Defining Megathrust Tsunami Sources at Northernmost Cascadia Using Thermal and Structural Information

By

Dawei Gao
B.Eng., Central South University, 2012

A Thesis Submitted in Partial Fulfillment
of the Requirements for the Degree of

MASTER OF SCIENCE

in the School of Earth and Ocean Sciences

University of Victoria

Supervisory Committee

Defining Megathrust Tsunami Sources at Northernmost Cascadia Using Thermal and Structural Information

By

Dawei Gao
B.Eng., Central South University, 2012

Supervisory Committee

Dr. Kelin Wang (School of Earth and Ocean Sciences)
Co-Supervisor

Dr. Stan Dosso (School of Earth and Ocean Sciences)
Co-Supervisor

Dr. Thomas James (School of Earth and Ocean Sciences)
Departmental Member

Abstract

Supervisory Committee
Dr. Kelin Wang (School of Earth and Ocean Sciences)
Co-Supervisor
Dr. Stan Dosso (School of Earth and Ocean Sciences)
Co-Supervisor
Dr. Thomas James (School of Earth and Ocean Sciences)
Departmental Member

The west coast of North America is under the threat of future great megathrust earthquakes and associated tsunamis. This dissertation addresses three urgent but unresolved issues in tsunami hazard assessment and risk mitigation at northernmost Cascadia. (1) Plate subduction is actively taking place along the Explorer segment of the northern Cascadia subduction zone and probably also its Winona fragment, and therefore their seismogenic and tsunamigenic potential should be investigated. (2) It needs to be investigated whether the shallowest portion of the Cascadia megathrust can undergo highly tsunamigenic trench-breaching rupture in great earthquakes like in the 2011 Tohoku-Oki earthquake at the Japan Trench. (3) For tsunami hazard assessment and early warning in southwestern British Columbia, high-resolution megathrust rupture models need to be systematically developed. To address the first issue, I develop finite element models for the Explorer segment to estimate thermally allowed potential seismic rupture zone of the megathrust. The results suggest a potential rupture zone of ~60 km downdip width located offshore. For the Winona fragment, where there are large uncertainties in the tectonic history and the age of the oceanic lithosphere, a preliminary estimate by considering only the thermal effect of sedimentation on a cooling lithosphere suggests a potential rupture zone of a minimum downdip width of 35 km. I address the second issue by reanalyzing seismic survey images off Vancouver Island with a focus on secondary faults around the accretionary wedge deformation front. No strong evidence suggests trench-breaching megathrust rupture being a dominant mode of fault behaviour at northern Cascadia, although the possibility cannot be excluded from tsunami hazard assessment. Buried rupture and coseismic activation of secondary faults may be more important at Cascadia. To address the third issue and also to investigate how the different secondary faults can contribute to tsunami generation, I compile a new Cascadia megathrust geometry and develop 21 tsunami sources using a three-dimensional (3D) dislocation model, including hypothetical models of frontal thrust, back-thrust, and splay faults. The dislocation models indicate that the buried rupture, splay-faulting rupture, and trench-breaching rupture can result in large seafloor uplift and coastal subsidence, and hence will lead to tsunamis that seriously affect the local coastal area. Back-thrust rupture near the deformation front is unimportant for tsunami generation. The model results also show that properly configured land-based Global Navigational Satellite System (GNSS) monitoring can distinguish between ruptures along the Cascadia megathrust and along the strike-slip Nootka fault and between megathrust ruptures of difference strike lengths and therefore can effectively contribute to real-time tsunami early warning. However, the results also reveal that these land-based measurements are not sensitive to the slip behaviour of the shallow portion of the megathrust farther offshore, demonstrating urgent need for near-trench, seafloor observations.

Table of Contents

List of Tables

List of Figures

Acknowledgments

I owe much gratitude to all those people whose help made this dissertation research possible. First of all, I would like to express my sincere gratitude to my supervisor, **Kelin Wang**, for his guidance, support, and encouragement, and also for providing the 1D thermal modelling code Sedtem and 3D dislocation modelling code Disl3d used in this research. His wealth of knowledge and passion for science always inspire me to work hard on my research. I also thank him for reviewing and editing drafts and offering comments during the writing of the thesis.

Special thanks go to my committee members **Stan Dosso** and **Thomas James**, and my external examiner, **Yan Jiang**, for their kind encouragement, helpful comments, and devoting their time to guiding my research.

I would like to thank all those who have contributed to this dissertation research. **Tania Lado Insua** obtained funding from Ocean Networks Canada and a collaboration with IBM Canada through Natural Sciences and Engineering Research Council of Canada Collaborative Research and Development grants (NSERC-CRD) for this research, carried out tsunami wave modelling on the cluster computer supported by Compute Canada and WestGrid, and provided the waveheight results and helpful comments and edits in Chapter 4. **Jiangheng He** developed the 2D finite element thermal modelling code PGCtherm2D and helped me resolve numerical and IT issues throughout my research. **Earl E. Davis** taught me the tectonics of the Explorer and Winona regions and helped me write that part of the thesis. **Michael Riedel** offered great guidance in gathering and interpreting the seismic records used in Chapter 3. **Tianhaozhe Sun** offered much help in my learning to use the dislocation modelling and many thoughtful discussions about developing tsunami sources. I also thank **George R. Priest**, **Chris Goldfinger**, and **Robert C. Witter** for thoughtful discussions about tsunami hazard assessment, **Xiang Gao** for assistance in setting up the thermal models, **Michael Bostock** and **Lindsay Chuang** for providing low frequency earthquake (LFE) information beneath northern Vancouver Island, **Honn Kao**, **Roy Hyndman**, **Kristin M.M. Rohr**, and **John F. Cassidy** for many helpful discussions and suggestions about the northern Cascadia subduction zone, **Subbarao Yelisetti** for helping me check the deformation structures at Cascadia's deformation front, **Peiling Wang** for sharing her dislocation models of the A.D. 1700 Cascadia earthquake, **Yuan Lu**, **Garry Rogers**, and **Lisa Nykolaishen** for discussions and feedbacks about using real-time Global Navigational Satellite System (GNSS) displacement data for tsunami early warning in northern Cascadia.

I would also like to thank **Lucinda Leonard** for the wonderful course on plate tectonics, and thank my friends and colleagues, **Yu Cui**, **Kun Liu**, **Ayodeji Kuponiyi, Lonn Brown**, **Jesse Hutchinson**, **Stefanie Wenker**, **Jeremy Gosselin**, **Zhuoli Xiao**, **Brian Green**, **Lingmin Cao**, and **Jianling Cao** for their help and encouragement.

This thesis is dedicated to my family, **Zhian Yu**, **Danghuai Gao**, **Dapeng Gao**, **Shiqiang Feng**, **Yinbin Feng**, **Shangqian Gao**, and **Yunqiu Li**, for their love, encouragement, and support.

Chapter 1. Introduction

1.1. Motivation and Objectives

Tsunamis are of great concern to many populated coastal areas around the world. Some recent great subduction zone earthquakes, such as the 2004 M_w 9.2 Sumatra and 2011 M_w 9.0 Tohoku-Oki earthquakes, generated devastating tsunamis and caused huge loss of life and damage to property. Although there has not been a great megathrust earthquake along the Cascadia margin over its approximately two-century recorded history, paleoseismic investigations [*Atwater et al.*, 1995; *Goldfinger et al.*, 2012] indicate that these events have repeatedly occurred in the past. The latest great Cascadia earthquake (M_w ~9) occurred on 26 January, A.D. 1700. This earthquake and the associated powerful tsunami led to serious damage along the Cascadia coast [*Ludwin et al.*, 2005]. The induced tsunami also caused damage across the Pacific Ocean in Japan [*Satake et al.*, 2003]. The west coast of North America is under the threat of future great megathrust earthquakes and associated tsunamis [*Leonard et al.*, 2012].

The research reported in this M.Sc. dissertation is designed to contribute to tsunami hazard assessment and risk mitigation at northernmost Cascadia, with the following three main objectives. (1) I will examine the thermal state of the Explorer segment of the Cascadia subduction zone and its Winona fragment further north to define the thermally allowed potential megathrust rupture zone. (2) I will re-examine the marine multichannel seismic images from surveys conducted in 1985 and 1989 by the Geological Survey of

Canada to identify potential tsunamigenic secondary faults in the area of the subduction zone deformation front and to investigate the possibility of trench-breaching rupture at Cascadia. (3) Based on the physics of rupture mechanics and currently available geological and geophysical observations, I will develop a suite of rupture scenarios using a three-dimensional (3D) dislocation model to be used as tsunami source models for long-term assessment of tsunami hazard in southwestern British Columbia and the development of real-time tsunami early warning strategy and systems.

The first objective addresses a major knowledge gap in our understanding of megathrust earthquake and tsunami potential along Canada's west coast. Previous megathrust earthquake studies at Cascadia excluded the tectonically complex Explorer region. The Explorer plate is a fragment of the Juan de Fuca plate off southwestern Canada. It is separated from the Pacific plate by the Explorer Ridge and Sovanco transform fault, and from the Juan de Fuca plate by the Nootka fault (Figure 1.1). A plate fragment beneath the Winona Basin may be separated from the bulk of the Explorer plate. The tectonically complex region of the Explorer plate is seismically very active (Figure 1.1), but it is not known whether megathrust earthquakes can occur along its boundary with the North America plate, either independently or in conjunction with events on the main part of the Cascadia subduction zone. A main question is whether the warm thermal state of the megathrust because of the very young age of the Explorer plate (~5 Ma at the deformation front) and the slow subduction rate (half of the rate south of the Nootka fault zone) can allow seismogenic faulting. I address this question by developing two-dimensional (2D) finite-element models constrained by earthquake and heat flow data (Chapter 2).

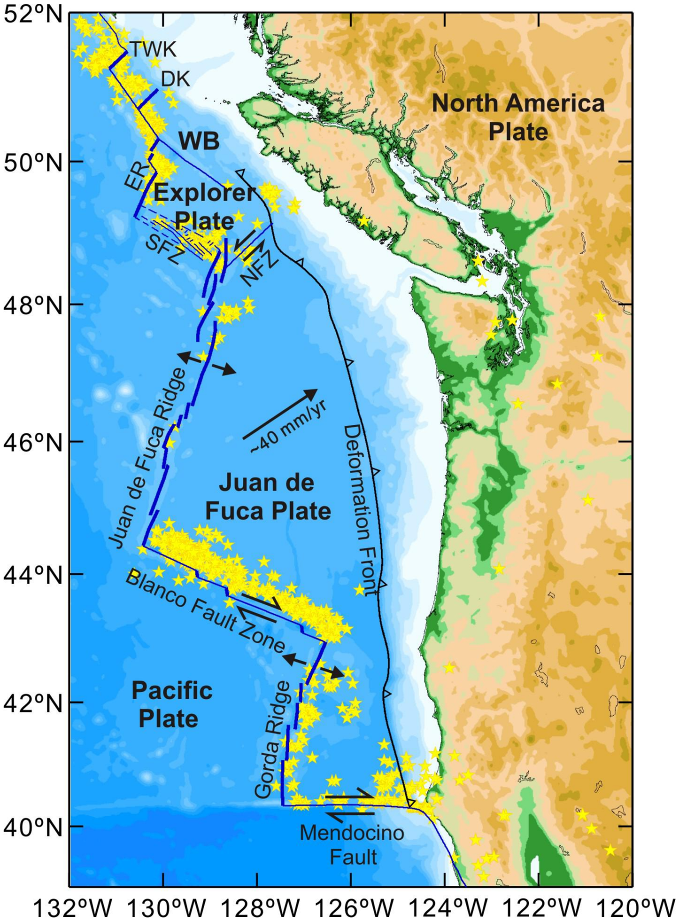

Figure 1.1. Tectonic setting of the Cascadia subduction zone. TWK, Tuzo Wilson Knolls; DK, Dellwood Knolls; WB, Winona basin; ER, Explorer Ridge; SFZ, Sovanco fault zone; NFZ, Nootka fault zone. Yellow stars represent earthquakes of $M_w > 4.0$ during 2006–2016. North of 48°N, the earthquake information comes from the catalogue of Earthquakes Canada (http://earthquakescanada.nrcan.gc.ca/index-eng.php); south of 48°N, the earthquake information comes from the United States Geological Survey (USGS, http://earthquake.usgs.gov/earthquakes/). Black barbed line indicates the deformation front.

The second objective addresses an issue raised by new observations made during the 2011 Tohoku-Oki earthquake. Megathrust rupture models previously developed for tsunami hazard assessment at Cascadia only consider two scenarios: buried rupture and splay faulting (Figure 1.2). The buried-rupture scenario is based on the assumption that the shallowest part of the fault exhibits a velocity-strengthening behaviour that tends to retard coseismic slip but allows aseismic slip after the earthquake [*Wang and He*, 2008]. Early rupture models developed for Cascadia [e.g., *Satake et al.*, 2003; *Cherniawsky et al.,* 2007] feature an updip zone of uniform rupture plus a downdip zone of linear transition with slip tapering to zero. More recent rupture models employed mainly by the Oregon Department of Geology and Mineral Industries (DOGAMI) for tsunami hazard assessment along the Oregon coast [e.g., *Priest et al.*, 2009, 2010; *Witter et al.,* 2011, 2013] feature rupture scenarios with slip peaking in the middle of the rupture zone and tapering to zero at both the updip and downdip ends (dark blue line in Figure 1.2c). The splay-faulting scenario [e.g., *Priest et al.*, 2009, 2010; *Witter et al.,* 2011, 2013] is based on indirect structural evidence for a possible splay fault along parts of the Cascadia margin [*Priest et al.*, 2009] (red dashed line in Figure 1.2c). However, a new question is posed for Cascadia by the 2011 M_w 9.0 Tohoku-Oki earthquake which exhibited huge fault slip extending to the trench, responsible for the devastating tsunami. Can the shallowest segment of the Cascadia megathrust also undergo trench-breaching rupture in great earthquakes or would it exhibit the velocity-strengthening behaviour to stop the coseismic rupture? I address this question by analyzing seismically imaged deformation structures near the accretionary wedge deformation front at Cascadia. If trench-breaching rupture is a dominant mode of coseismic slip at Cascadia, we expect it to leave some structural evidence.

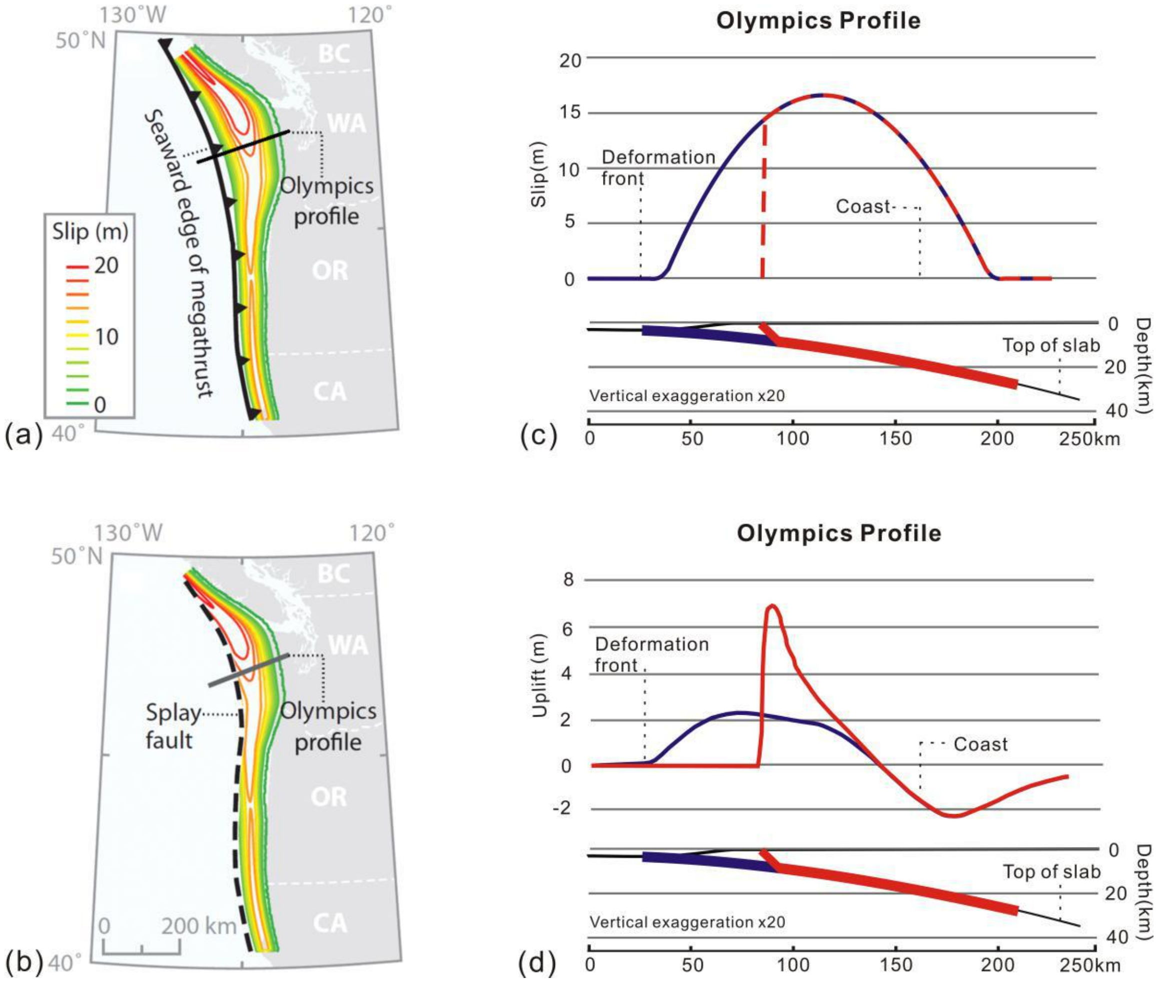

Figure 1.2. Examples of previous megathrust tsunami sources for tsunami hazard assessment at Cascadia [modified from *Witter el al.*, 2013]. (a) Map view of slip distribution for the buried rupture. (b) Map view of slip distribution for the splay faulting rupture. Dashed line is the surface trace of the assumed splay fault, which merges with the deformation front in southern Cascadia. (c) Fault slip along the profile shown in (a) and (b). Blue, buried rupture; red, splay faulting rupture. (d) Resultant seafloor uplift and coastal subsidence along the same profile. Blue, buried rupture; red, splay faulting rupture.

The third objective addresses an urgent need for long-term tsunami hazard assessment and real-time tsunami early warning at northernmost Cascadia. Existing megathrust tsunami sources that are of sufficient resolution for detailed tsunami hazard assessment along the local coast are focused on the Oregon part of the margin [e.g., *Priest et al.*, 2009, 2010; *Witter et al.,* 2011, 2013]. Low-resolution models such as those used by *Satake et al.* [2003] and *Cherniawsky et al.* [2007] are adequate for modelling the impact of a Cascadia tsunami across the Pacific or for illustrating the potential impact on the Cascadia local coast to the first order. Systematic high-resolution rupture scenarios have not been developed for tsunami hazard assessment in southwestern British Columbia. As part of this M.Sc. research project, I will develop a suite of rupture scenarios using a 3D dislocation model based on the latest structural information, knowledge of rupture mechanics, and what we have learned from recent large tsunamigenic earthquakes such as those at the Sumatra, Chile, and Japan subduction zones. This part of the study is in collaboration with Ocean Networks Canada. The rupture scenarios presented in this dissertation and their more refined versions can be used to develop tsunami inundation and evacuation maps to guide the design of mitigation strategy. The inundation models can also be used for the development of tsunami early warning strategy. Insights from this study can be applied to other subduction zones for tsunami hazard assessment and early warning.

1.2. Structure of This Thesis

Chapter 2 describes 2D finite-element modelling to investigate the thermal regime of the Explorer segment of the Cascadia subduction zone and define the spatial extent of the potential rupture zone (Objective 1). This part of the study also investigates whether megathrust earthquakes are thermally allowed if we assume the Winona fragment is actively subducting, but details are presented in the **Appendix**. **Chapter 3** describes the synthesis and analyses of seismically imaged deformation structures around the northern Cascadia deformation front and explores the possibility of slip-to-trench rupture at Cascadia (Objective 2). **Chapter 4** describes 3D dislocation modelling to develop tsunami source models, presents 21 tsunami source models developed in this study, and discusses applications of the source models to long-term tsunami hazard assessment and real-time tsunami early warning at northernmost Cascadia (Objective 3). **Chapter 5** summarizes the conclusions of the dissertation and recommendations for future research.

Chapter 2. Potential Megathrust Rupture Zone of the Explorer Segment

2.1. Thermal Constraints to the Potential Rupture Zone

Given the lack of instrumentally recorded great subduction zone earthquakes at Cascadia, our knowledge of the cosesimic slip behaviour of the Cascadia megathrust in past earthquakes is based mainly on paleoseismic studies [e.g., *Atwater et al.*, 1995; *Goldfinger et al.*, 2012; *Wang et al.*, 2013]. Although these studies offer important constraints on the recurrence pattern and along-strike variations of megathrust rupture, insufficient coverage of paleoseismic data in the margin-normal direction causes difficulties in defining the downdip limit of the megathrust rupture [*Wang et al.*, 2013].

Over the past two decades, models of the potential rupture zone of the Cascadia subduction megathrust have been proposed in a number of studies. These models are based mainly on thermal arguments, although deformational and structural evidence has also been used to offer supporting arguments [e.g., *Hyndman and Wang*, 1993, 1995; see reviews by *Hyndman*, 2013; *Wang and Tréhu*, 2016]. For typical megathrust fault zone material which is quartz rich [*Wang and Tréhu*, 2016], it is assumed that the fault may exhibit velocity-weakening behaviour and nucleate seismic rupture if the temperature is less than 350°C. At higher temperatures, the fault is assumed to exhibit velocity-strengthening behaviour which prohibits rupture initiation but allows limited rupture propagation. At even higher temperatures, such as > 450°C, the fault zone material exhibits a viscous behaviour and limits the maximum downdip extent of rupture. At temperatures lower than roughly 150°C, phyllosilicate minerals in the fault zone typically exhibit velocity-strengthening [*Ikari et al.*, 2011], although they may not fully stop rupture propagation [*Wang and Tréhu*, 2016].

In the 1990's, coseismic rupture and interseismic locking at Cascadia were thought to share the same downdip limit [e.g., *Hyndman and Wang*, 1995; *Flück et al.*, 1997]. The maximum downdip limit of interseismic locking (the eastern limit of the transition zone) proposed by *Hyndman and Wang* [1995] roughly corresponds to the 450°C isotherm (Figure 2.1a). The updip limit was assumed to be near the deformation front where the temperature at the top of the igneous crust is above 150°C [*Hyndman and Wang*, 1995]. In recognition of the importance of interseismic viscoelastic stress relaxation and to compensate for this effect in an elastic dislocation model, *Wang et al.* [2003] invoked a very wide "effective transition zone" (ETZ, Figure 2.1b). To model the A.D. 1700 great Cascadia earthquake, *Wang et al.* [2003] assumed the slip deficits in the interseismic locked zone would be fully recovered and the cosesimic rupture would stop halfway in the ETZ. The resultant coseismic model of a uniform rupture in the updip half with a linear transition in the downdip half was later used by *Satake et al.* [2003] and *Cherniawsky et al.* [2007] for tsunami modelling. Because the shallow portion of the megathrust is thought to exhibit a velocity-strengthening behaviour [*Wang and He*, 2008; *Hu and Wang*, 2008] that tends to retard rupture, and observations from large earthquakes and predictions by crack mechanics suggest that fault slip tapers in both updip and downdip directions [*Wang and He*, 2008], *Priest et al.* [2010, 2013, 2014] and *Witter et al.* [2011, 2012, 2013] used a bell-shaped slip distribution in the downdip direction proposed by *Wang and He* [2008] to develop tsunami sources for hazard assessment (e.g., blue curve in Figure 1.2c). A simplified version of the coseismic slip model of *Priest et al.* [2010] is shown in Figure 2.1c, in which the cosesimic rupture limits are exactly the same as those used by *Wang et al.* [2003] for modelling the A.D. 1700 Cascadia earthquake, and the slip peaks in the middle of the coseismic rupture zone in the location roughly corresponding to the downdip limit of the interseismic fully locked zone portrayed in Figure 2.1b.

There are also more recent interseismic locking models for Cascadia derived by directly inverting geodetic data using elastic dislocation models and without invoking thermal or other arguments [e.g., *McCaffrey et al.*, 2007, 2013; *Schmalzle et al.*, 2014]. Despite the severe lack of offshore resolution of the land-based geodetic observations, these models are helpful in indicating the general locking state of the Cascadia megathrust. However, the geodetically inferred interseismic locking models cannot be flipped to become the coseismic rupture models for a number of reasons [see review by *Wang and Tréhu*, 2016]. The downdip limit of locking is usually overestimated from inverting geodetic observations. For example, a weak patch of the fault may not be slipping simply because a neighbouring patch is truly locked [*Wang*, 2007]. Hence the “apparent locked zone”, that is, the zone of no slip, is usually larger than the zone that is truly locked. More importantly, the effect of interseismic viscoelastic stress relaxation

[*Wang et al.*, 2012] has usually been ignored when modelling interseismic deformation with elastic dislocation models, leading to artifacts.

All the existing coseismic rupture models for Cascadia stop at the Nootka fault zone (NFZ, Figure 2.2) and do not include the Explorer segment. Seismic and geodetic observations in the Explorer area are far from adequate for constraining megathrust rupture potential. The local seismic network has never recorded any interplate earthquake here. The sparsity of Global Navigation Satellite System (GNSS) sites does not permit a reliable determination of the present locking state of the megathrust [*Mazzotti et al.*, 2003], although the limited data are consistent with locking [*Y. Jiang*, personal communication, 2016]. To define the potential megathrust rupture limit in the Explorer region, I assume its downdip limit is controlled by a temperature of 450°C as suggested by *Hyndman and Wang* [1993; 1995]. To estimate the thermal limit, I develop 2D finite-element models constrained by earthquake and heat flow data. Most of the ensuing text in the rest of this chapter is from an unfinished manuscript titled “Thermal state of the Explorer segment of the Cascadia subduction zone: Implications for seismic and tsunami hazard”, by D. Gao, K. Wang, E.E. Davis, and J. He.

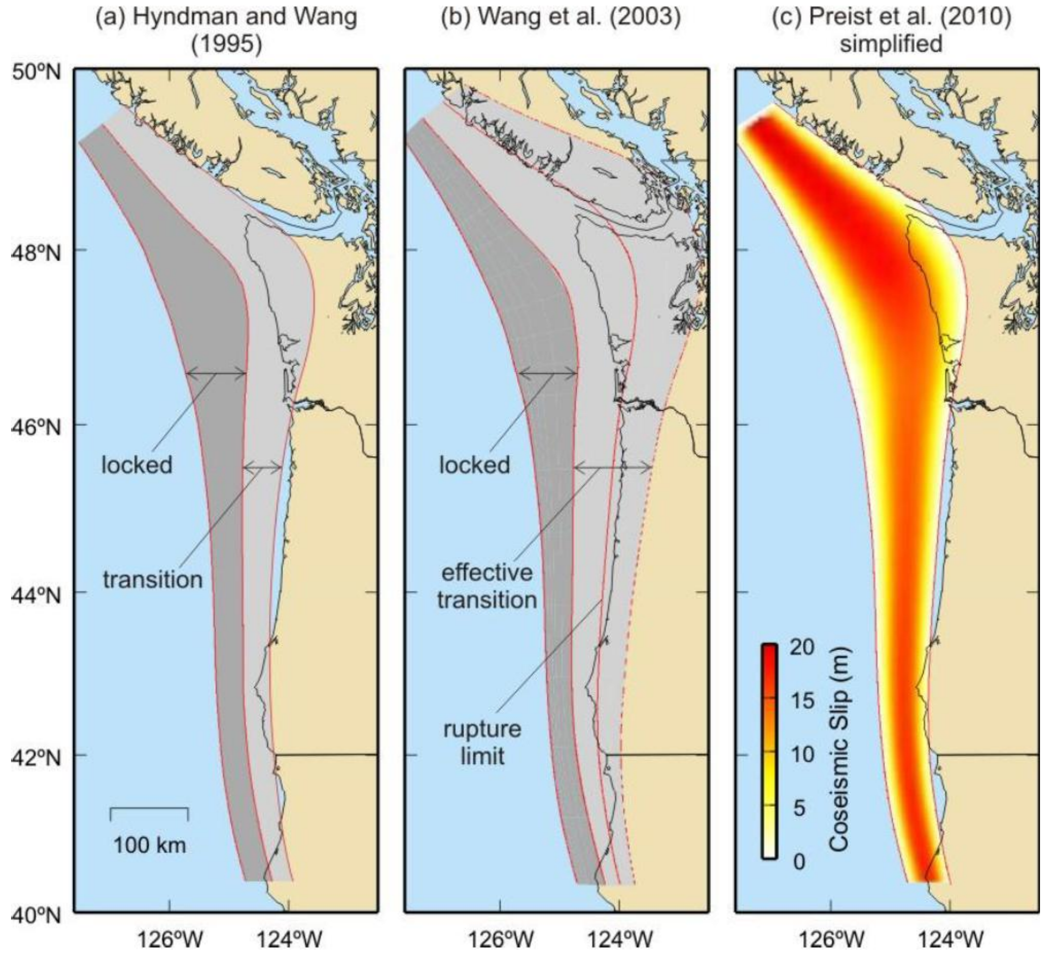

Figure 2.1. Typical interseismic locking or coseismic rupture models for Cascadia [summarised by *Wang and Tréhu*, 2016]. (a) Model by *Hyndman and Wang* [1995]: a uniform locked zone plus a linear downdip transition zone. (b) Model by *Wang et al.* [2003]: a uniform locked zone with a very wide effective transition zone (ETZ) to account for the missing viscoelastic effects. To model the A.D. 1700 great Cascadia megathrust earthquake, the coseismic rupture was assumed to stop halfway in the ETZ. (c) Coseismic slip model used by *Priest et al.* [2010]. The updip and downdip rupture limits are exactly the same as those in (b), but the downdip distribution of slip is assumed to have a bell shape (see Figure 1.2c) and 500 yr of slip deficit is assigned to the apex of the slip.

2.2. 2D Finite-element Thermal modelling

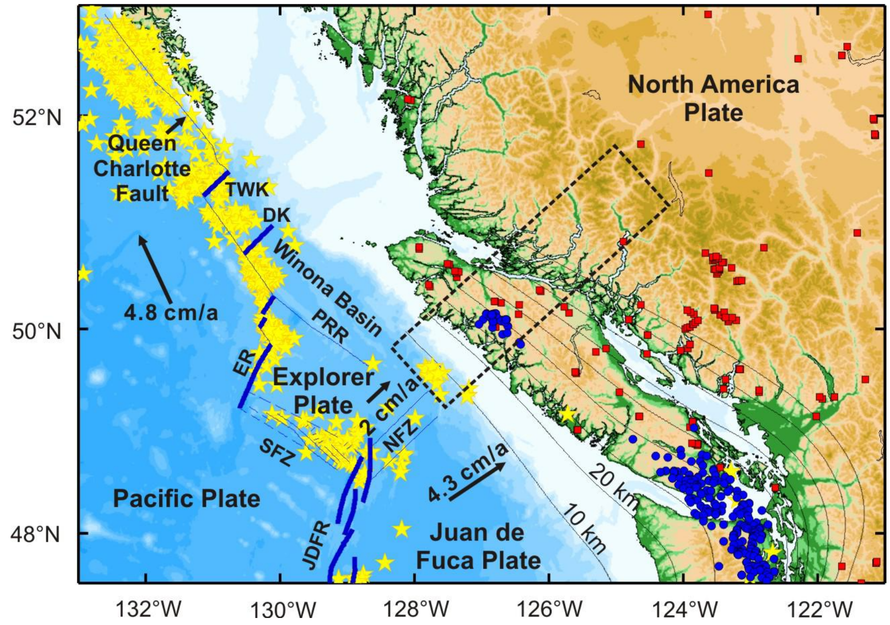

Figure 2.2. Tectonic setting of the northern Cascadia subduction zone, with the thermal model corridor shown as a dashed box. TWK, Tuzo Wilson Knolls; DK, Dellwood Knolls; ER, Explorer Ridge; PRR, Paul Revere Ridge; SFZ, Sovanco fault zone; NFZ, Nootka fault zone; JDFR, Juan de Fuca Ridge. Plate motion (labeled black arrows) is relative to NA [*Riddihough*, 1984; *DeMets et al.*, 1994; *Wilson*, 1993]. Yellow stars represent earthquakes of $M_w > 4.0$ during 2006–2016 from the catalogue of Earthquakes Canada (http://earthquakescanada.nrcan.gc.ca/index-eng.php). Red squares indicate locations of heat flow observations. Offshore heat flow sites are not shown here because they are far from the model corridor. Blue circles indicate low frequency earthquake epicentres determined by *Royer and Bostock* [2014], with more recent updates by *L. Chuang* [personal communication, 2015]. Subduction interface from *McCrory et al.* [2004] is contoured at 10 km intervals in black.

2.2.1. Tectonic Structure and Heat Flow Observations

The Explorer (EX) plate is a fragment of the Juan de Fuca (JDF) plate currently subducting beneath the North America (NA) plate (Figure 2.2). It was detached from the JDF along the Nootka fault zone (NFZ) about 4 Ma ago [*Riddihough*, 1984], and through its short history has fragmented further and deformed internally. This is evident in the broadly distributed present-day seismicity, the evolution of the Explorer Ridge (ER) spreading centre and NFZ, and the development of the Paul Revere Ridge (PRR) which may separate a plate fragment beneath the Winona Basin from the bulk of the EX plate. Observations of episodic occurrence of non-volcanic tremor, now recognized as a characteristic behaviour of the Cascadia subduction interface, beneath northern Vancouver Island put it beyond any doubt that EX is currently subducting beneath the NA plate [*Kao et al.*, 2009].

Assuming that the rate of internal deformation of the EX plate is small relative to the EX–NA interplate rate, it is reasonable to infer from EX–PA and PA–NA motions that the EX plate thrusts northeastward beneath NA at ~20 mm/yr [*Riddihough*, 1984]. This is approximately half the subduction rate of the JDF Plate south of the Nootka fault. The subducting EX plate is young (~5 Ma near the deformation front) [*Wilson*, 1993, 2002] and is blanketed by thick sediment along the continental margin [*Davis and Riddihough*, 1982; *Davis and Hyndman*, 1989].

Beneath northern Vancouver Island the subducted Explorer slab was first detected using receiver function analysis [*Cassidy et al.*,1998]. In more recent receiver function studies, *Audet et al.* [2008] and *Audet et al.* [2010] proposed a complex geometry of the shallow part (<50 km depth) of the subducting plate, but with very large uncertainties. Other available slab geometry models [e.g., *McCrory et al.*, 2004] for the Explorer region are defined by extrapolating the geometry of the Cascadia subduction interface defined to the south. The updated model by *McCrory et al.* [2012] depicts a smoothed version of *Audet et al.* [2010] in Explorer region.

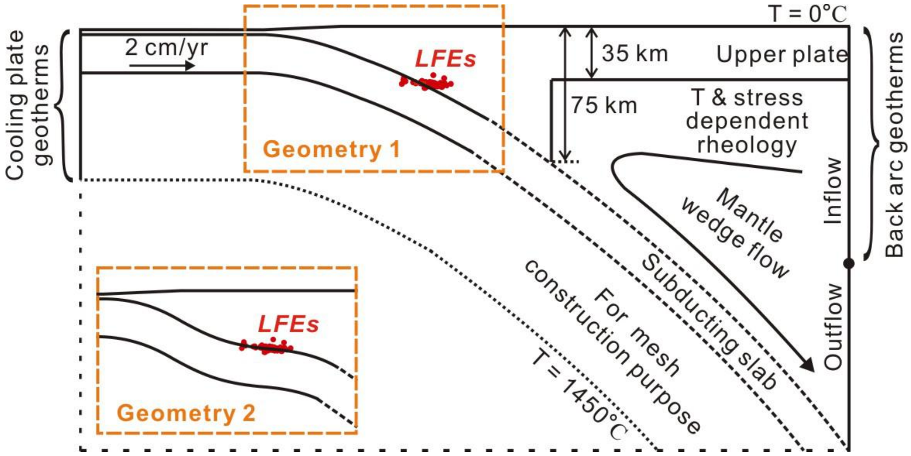

Figure 2.3. Schematic illustration of model structure and boundary conditions. Solid circles are LFE hypocentres. Two possible slab geometries are shown.

Newly published information on the hypocentral locations of low frequency earthquakes (LFEs) [*Royer and Bostock*, 2014] offers us an opportunity to improve the definition of the plate interface geometry. LFEs are a class of earthquakes of low magnitudes (M < 3) and frequencies (1-10 Hz) embedded in the sources of non-volcanic seismic tremor [*Shelly et al.*, 2006, 2007]. It is notoriously difficult to determine the depths of tremor sources, but the hypocentres of the LFEs can be rather accurately determined [*Royer and Bostock*, 2014]. The LFE hypocentres determined by *Royer and Bostock* [2014], with more recent updates [*L. Chuang*, personal communication, 2015], in Northern Vancouver Island are shown in Figure 2.2. Their cross-sectional view along the model corridor (Figure 2.2) is shown in Figure 2.3.

The LFE hypocentres are distributed locally along a sub-horizontal plane. We can use the average position of the LFE cluster to devise a simple slab geometry featuring monotonically increasing dip with depth (Geometry 1 in Figure 2.3), or we can obtain a more complex geometry by allowing the subduction interface to fit the locally flat shape of the LFE cluster (Geometry 2 in Figure 2.3). Geometry 2 may appear to be somewhat unusual but is similar to that of a segment of the Mexican subduction system [e.g., *Kim et al.*, 2012]. The shallow end is the same for both options. At the deformation front, the igneous crust of the subducting plate is around 5 km below sea level and is covered by 3 km of sediments (discussed in the next section). Between the deformation front and the LFE cluster, the slab geometry is not quantitatively constrained, and I simply introduce a smooth transition. Because intraslab earthquakes are few, there is great uncertainty in how far the Explorer plate penetrates into the mantle, although the length of the subducting slab is expected to be greater than ~240 km according to *Riddihough* [1984]. For the deeper part of the plate interface (>50 km depth), I extend the curve from shallow depths (Figure 2.3) for the convenience of constructing a finite element mesh. The deep plate geometry has little effect on the model results in our region of interest – the potential rupture zone of the shallow megathrust.

Lewis et al. [1997] presented heat flow measurements obtained from 15 shallow (100 m) boreholes and 6 mineral exploration wells in northern Vancouver Island. Three of the heat flow values (379-3, 379-4 and 379-5) were reported to have been affected by groundwater flow and hence are excluded from this study. The remaining heat flow measurements within a 90 km wide corridor are used as model constraints (Figure 2.2). Uncertainties in the heat flow measurements were not specified in the original reference. I assign an error bar of 10% to all the values which is typical for terrestrial heat flow measurements. These heat flow observations offer useful constraints for modelling the deep thermal structure of the Explorer segment. Unfortunately, no offshore heat flow measurements have been made in this southern-Explorer study corridor; models of the shallow thermal structure at the updip end of the model transect must be derived from plate age and estimates of sedimentation history as well as the slab geometry.

2.2.2. Modelling Method and Parametres

I use the finite element code PGCtherm2D, written by Dr. Jiangheng He at the Pacific Geoscience Centre, Geological Survey of Canada, to develop a 2D steady state model along the margin-normal corridor shown in Figure 2.2, similar to *Wada et al.* [2008] and *Gao and Wang* [2014] for southern Vancouver Island. The model consists of a non-deforming overriding plate, a non-deforming subducting plate with prescribed motion, and a viscous mantle wedge with a temperature- and stress-dependent wet olivine rheology (Figure 2.3; parametre values for wet olivine come from *Karato and Wu*, 1993). Details of the flow law for the mantle wedge are described by *Wada et al.* [2008]. The subducting slab is assigned a rate of ~20 mm/yr [*Riddihough*, 1984] and the overlying plate is assigned zero velocity from the surface to Moho depth. The continental Moho depth is assumed to be 35 km in this region but the actual bottom of the no-flow upper plate is deeper due to the thermally controlled mantle rheology. Material property values are similar to or the same as those used in previous thermal modelling work for Cascadia [e.g., *Hyndman and Wang*, 1993; *Wada et al.*, 2008; *Gao and Wang*, 2014]. For example, thermal conductivities of the continental crust, slab, and mantle wedge are assumed to be 2.5, 2.9, and 3.1 W $m^{-1}K^{-1}$, respectively, and radiogenic heat production value of the continental crust and the rest of the model domain are assumed to be 0.4 and 0.02 μW m^{-3}, respectively.

The temperatures for the upper and the lower boundaries of the model are kept at 0°C and 1450°C, respectively [e.g., *Peacock and Wang*, 1999; *Wada et al.*, 2008]. For the landward boundary (very far from our region of interest and thus unimportant for the purpose of this work) the geotherm is assigned in the same way as in *Currie et al.* [2004] and *Wada et al.* [2008], etc. which yields a surface heat flow 75 mW/m^{-2}. The seaward boundary, set to be 15 km west of the deformation front, is assigned the thermal profile of a 5-Ma old oceanic plate. It is advection of the age-controlled incoming-plate thermal structure by subduction that controls the thermal state of the shallow part of the subduction zone and the plate interface. Because of the efficiency of the advective transfer of heat by the slab, the depth of the lower boundary of the model is unimportant for a young slab like the Explorer plate [*Peacock and Wang*, 1999].

In determining the thermal structure of the incoming plate, the effects of sediment deposition and compaction have to be considered. Published seismic profile 85-04 [*Davis and Hyndman*, 1989] shows that the incoming Explorer plate is covered with very thick sediments. The thickness at the deformation front is about 3 km [*M. Riedel*, personal communication, 2015], similar to that offshore of southern Vancouver Island [*Hyndman and Wang*, 1993]. The sedimentation history is poorly known. Due to lack of specific constraints on the sedimentation history, I assume the sediment accumulated from 4 Ma to the present thickness (3 km) at a constant rate. To address the possibility of accelerated sedimentation during the Pleistocene [*Su et al.*, 2000], I also consider a model in which sedimentation occurs only during the most recent 1 Ma. To calculate the geotherms in the plate, I use a 1D heat transfer model [*Wang and Davis*, 1992] for a cooling lithosphere (5 Ma), including the thermal effects of sediment deposition and compaction. In the model, the sediment surface defines the reference frame. Sediment is added with the specified deposition rate; the sediment-basement contact moves to greater depths in this reference frame. During the sedimentation process, the cold sediments absorb heat from the material below, and heat-bearing fluid is expelled from the compacting sediment to maintain an exponential dependence of porosity on depth. Details of the mass movement and heat transfer equations are described by *Wang and Davis* [1992]. The material properties and porosity-depth relationship are the same as those used by *Hyndman and Wang* [1993] for southern Vancouver Island. In detail, a widely used exponential porosity function is employed here: $\phi = \phi_0 e^{-z/L}$, where ϕ is porosity, ϕ_0 is porosity value at the seafloor, z is depth below seafloor, and L is a depth scale. In addition, the porosity is constrained not to be less than a minimum value $\phi_{\min} = 0.15$. All the parametre values are the same as in *Hyndman and Wang* [1993] and are listed in Table 2.1.

Table 2.1. Material Properties

Parametre	**Symbol**	**Value**	**unit**
Water conductivity	λ_w	0.6	$Wm^{-1}K^{-1}$
Grain sediment conductivity	λ_s	2.74	$Wm^{-1}K^{-1}$
Basement conductivity	λ_b	2.9	$Wm^{-1}K^{-1}$
Water thermal capacity	ρc_w	4.30	$MJ\ m^{-3}K^{-1}$
Sediment thermal capacity	ρc_s	2.65	$MJ\ m^{-3}K^{-1}$
Basement thermal capacity	ρc_b	3.3	$MJ\ m^{-3}K^{-1}$
Surface porosity	ϕ_0	0.6	
Porosity depth scale	L	1.5	km
Minimum porosity	$\phi_{\min}$	0.15	

The subduction interface is simulated using a line-element technique that allows more accurate calculation of stress and heat generation along the interface [*Gao and Wang*, 2014] than do the viscous-layer [*Wada et al.*, 2008] and differential-motion [*van Keken et al.*, 2002] methods. It is appropriate to assume that the maximum depth of decoupling between the subducting plate and the overlying mantle wedge is about 75 km [*Wada and Wang*, 2009]; uncertainties in this depth have negligible impact on the model results for our region of interest.

In modelling the shallow thermal structure of subduction zones, the effect of frictional heating along the megathrust can be important [*Gao and Wang*, 2014]. The rate of frictional heating is the product of fault slip rate v and shear stress $\tau = \mu(\sigma_n - P) \approx \mu(1-\lambda)\sigma_n = \mu' \sigma_n$, where μ is the coefficient of friction, σ_n is normal stress (approximately the value of the lithostatic pressure), P is pore fluid pressure, and λ is the ratio of pore fluid pressure to lithostatic pressure. Parametre $\mu' = \mu(1 - \lambda)$ is normally referred to as the effective friction coefficient but it is called the apparent friction coefficient by *Gao and Wang* [2014] because its value is expected to vary during seismic slip. The precise physical meaning of μ', and the details of calculating frictional heating, viscous heating further downdip, and heat dissipation in the zone of frictional-viscous transition zone along the plate interface are as described by *Gao and Wang* [2014].

2.3. Modelling Results

For each slab geometry shown in Figure 2.3, I test three values of the effective coefficient of friction μ'. Past modelling experience suggests that a μ' value of 0.03 is appropriate for Cascadia and many other subduction faults [e.g., *Wada and Wang*, 2009; *Gao and Wang*, 2014; *Wang et al.*, 2015] and hence is the preferred value for the Explorer segment. The other two μ' values, 0 and 0.1, represent no and very high frictional heating, respectively [*Gao and Wang*, 2014]. For either geometry, the predicted heat flow fits the measurements very well independent of the μ' values (Figures 2.4a and 2.5a).

Even for the offshore area, heat flows predicted with different μ' values are quite similar. The muted effect of frictional heating is because of the low subduction rate (~2 cm/yr) and the very shallow depth (and small σ_n) of the affected fault segment.

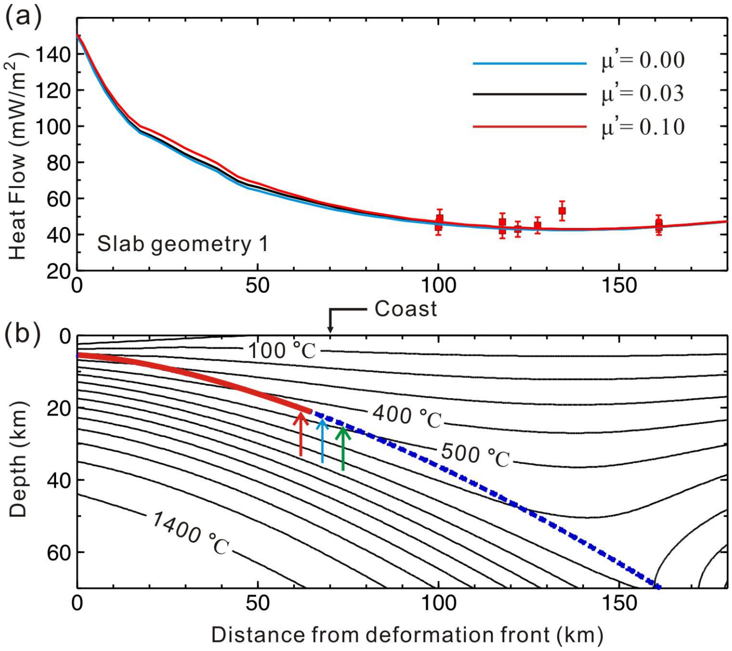

Figure 2.4. Thermal model results (simple slab geometry). (a) Model predicted surface heat flow with the simple slab geometry. An error bar of 10% is assigned to all the heat flow values. (b) Thermal structure for the simple slab geometry with $\mu' = 0.03$. Thick line marks the subduction interface, with the solid red portion marking the potential megathrust rupture zone terminated by a temperature of 450°C. The arrows in (b) mark the locations of 450°C on the plate interface for three other models, each differing from the shown model only in one parametre: red, $\mu' = 1.0$; blue, $\mu' = 0$; green, sedimentation is assumed to have occurred during the most recent 1 Ma instead of 4 Ma.

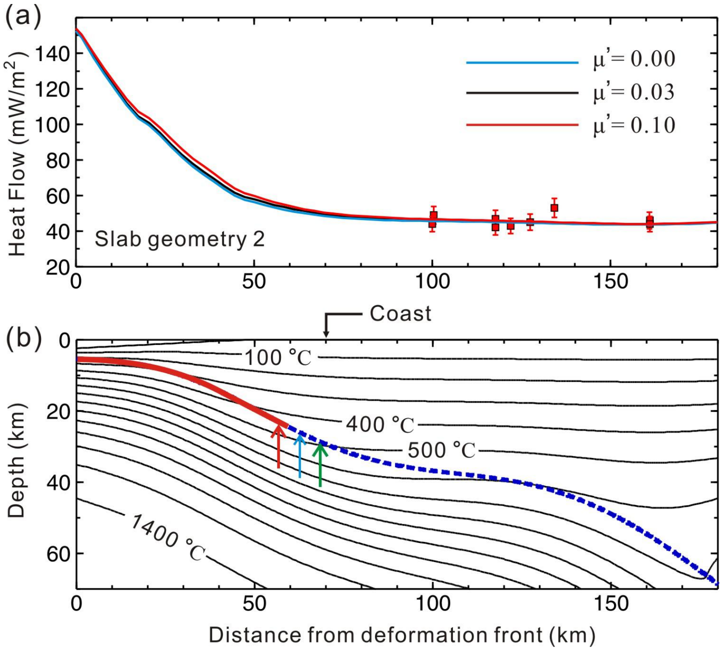

Figure 2.5. Thermal model results (flat-slab geometry). (a) Model predicted surface heat flow with the flat-slab geometry. An error bar of 10% is assigned to all the heat flow values. (b) Thermal structure for the flat-slab geometry with $\mu' = 0.03$. Thick line marks the subduction interface, with the solid red portion marking the potential megathrust rupture zone terminated by a temperature of 450°C. The arrows in (b) mark the locations of 450°C on the plate interface for three other models, each differing from the shown model only in one parametre: red, $\mu' = 1.0$; blue, $\mu' = 0$; green, sedimentation is assumed to have occurred during the most recent 1 Ma instead of 4 Ma.

The modeled thermal structure of the subduction zone with $\mu' = 0.03$ is shown in Figures 2.4b and 2.5b for the two slab geometries. If we assume that the portion of the megathrust where rupture can initiate is limited to a temperature of 350°C as discussed in Section 2.1, the results indicate that, for either slab geometry, the Explorer segment is cold enough to allow megathrust earthquakes to initiate over a zone of about 35–40 km downdip width. If we further assume that the rupture can propagate as far downdip as limited by a temperature of 450°C [*Hyndman and Wang*, 1993], the potential rupture zone may be ~60 km wide extending to near the coast of Vancouver Island.

As is obvious from Figures 2.4 and 2.5, the results are not very sensitive to the assumed slab geometry and frictional heating. Assuming no ($\mu' = 0$) or large ($\mu' = 0.1$) frictional heating moves the downdip limit by less than 10 km (Figures 2.4b and 2.5b). If we assume that sedimentation on the EX plate took place only during the most recent 1 Ma, the incoming plate would be slightly colder, and thus the thermally defined downdip rupture limit extends about 15 km further landward than in the model of 4-Ma sedimentation (Figures 2.4b and 2.5b, green arrow).

Here I assume the potential coseismic rupture in the Explorer segment is confined by a temperature of 450°C defined by the model with slab geometry 1, $\mu' = 0.03$, and sedimentation occurring during the most recent 4 Ma (Figure 2.4b, solid red line). For the downdip limit of the potential coseismic rupture, I hand-extrapolate the 2D potential rupture zone in the Explorer segment and merge it with the coseismic rupture model proposed by *Wang et al.* [2003] (Figure 2.1b) by allowing a smooth transition. Similar to earlier work [e.g., *Hyndman and Wang*, 1995; *Wang et al.*, 2003] at Cascadia, the updip limit of the potential rupture zone is assumed to be at the deformation front. Different from previous smooth versions of the deformation front, I employ a more detailed version in this work. The resultant potential rupture zone is shown in Figure 2.6b.

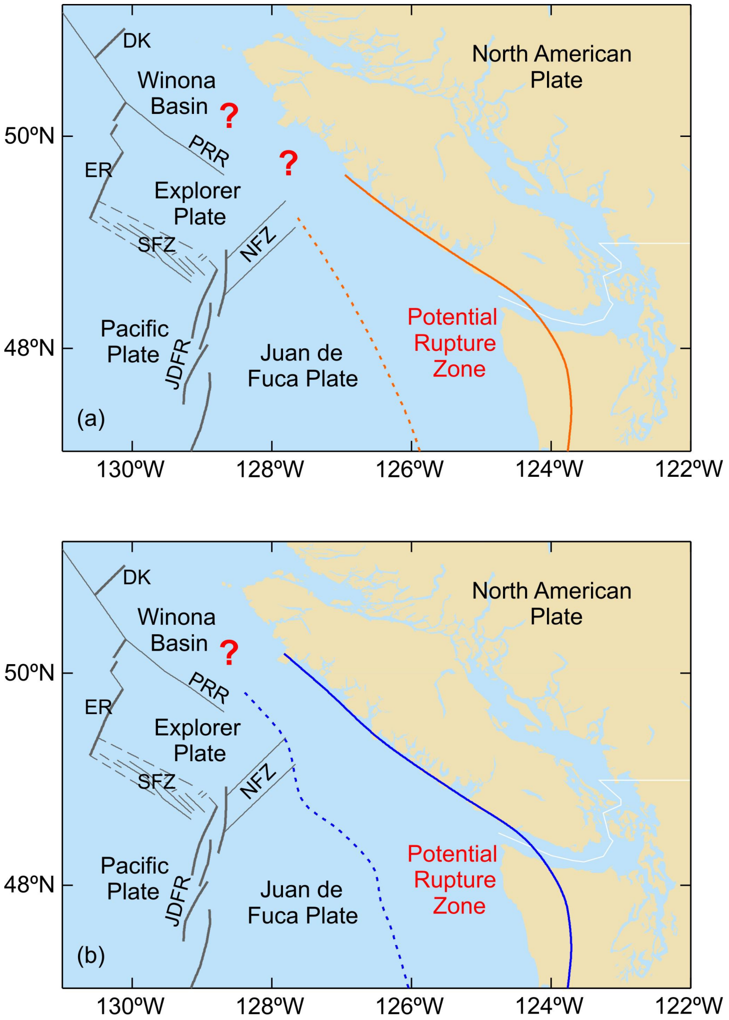

Figure 2.6. Potential megathrust rupture zone of northern Cascadia. DK, Dellwood Knolls; ER, Explorer Ridge; PRR, Paul Revere Ridge; SFZ, Sovanco fault zone; NFZ, Nootka fault zone; JDFR, Juan de Fuca Ridge. (a) The downdip limit of the potential rupture zone (solid orange line) proposed by *Wang et al.* [2003]. The updip limit (dashed orange line) is assumed to be at the deformation front. (b) New downdip limit of the potential rupture zone (solid blue line) for Cascadia including the Explorer segment. The updip limit (dashed blue line) here is a more detailed version compared with that of *Wang et al.* [2003].

It is highly probable that the Winona fragment is also subducting beneath the NA plate and is capable of generating megathrust earthquakes and associated tsunamis. Because of the complex tectonic history of the Winona region [e.g., *Davis and Riddihough*, 1982; *Rohr and Tryon*, 2010], a fully quantitative assessment of the megathrust potential will require future observations to be made to resolve a number of contentious questions, and it is beyond what can be realistically accomplished in this M.Sc. project. A very preliminary effort has been made to investigate the thermal state of the Winona fragment and is explained in Appendix.

Chapter 3. Potential Tsunamigenic Structure around Cascadia Deformation Front

3.1. Insights from Japan and Sumatra

At Cascadia, there have been no instrumentally recorded great subduction zone earthquakes in its two-century written history. But paleoseismic investigations indicate that ~20 earthquakes have occurred on the Cascadia megathrust over the last 10,000 years [*Atwater et al.*, 1995; *Goldfinger et al.*, 2012]. The most recent great Cascadia earthquake occurred on 26 January A.D. 1700 with a moment magnitude (M_w) ~9, resulting in a powerful tsunami that propagated across the Pacific Ocean to cause damage in Japan [*Satake et al.*, 2003]. Although this event and earlier great earthquakes provided valuable information on the seismogenic and tsunamigenic potential of the Cascadia megathrust, the information is far from adequate for understanding the slip behaviour of the shallow part of the megathrust during earthquakes, which is of first-order importance for tsunami generation.

For the purpose of tsunami hazard assessment, two models of tsunami generation have been assumed at Cascadia [e.g., *Priest et al.*, 2009, 2010; *Witter et al.*, 2012, 2013]: (1) seafloor deformation induced by a buried rupture (Figure 3.1a), and (2) enhanced seafloor uplift due to splay faulting (Figure 3.1b). The first scenario is based on the assumption that the shallowest portion of the megathrust exhibits a velocity-strengthening behaviour which normally resists coseismic rupture but allows aseismic slip after the earthquake [e.g., *Wang and Hu*, 2006]. An example is the 28 March 2005 M_w 8.7 Nias, Sumatra, earthquake. Continuous GPS observations on forearc islands (~60 km from the trench) revealed that little slip occurred on the shallow portion of the fault during the earthquake but significant aseismic afterslip occurred updip of the cosesimic rupture area [*Hsu et al.*, 2006]. If the effects of viscoelastic relaxation are incorporated, the actual amount of afterslip is even greater [*Sun and Wang*, 2015] than that estimated from an elastic model [*Hsu et al.*, 2006].

The second scenario is based on indirect structural evidence that a splay fault may be present along the central Cascadia margin, separating older and younger accretionary complexes [*Priest et al.*, 2009]. If the shallowest portion of the megathrust exhibits coseismic strengthening, a splay fault may be activated by a sudden compression of the outer accretionary wedge during a great earthquake [*Wang and Hu*, 2006]. Because of the steeper dip of the splay fault than the megathrust, seafloor uplift will be enhanced (Figure 3.1b), contributing to tsunami generation. Splay faulting is suspected to have facilitated tsunami generation in the 1946 Nankai earthquake (Figure 3.1b) [e.g., *Cummins and Kaneda*, 2000] and some other great megathrust earthquakes, such as the 1960 Chilean and 1964 Alaskan earthquakes [*Plafker*, 1972]. Although there is no conclusive evidence that the inferred splay fault at Cascadia is actually present and/or contributed to past tsunami generation, the possibility of splay faulting cannot be excluded from tsunami hazard assessment [see review by *Wang and Trehu*, 2016].

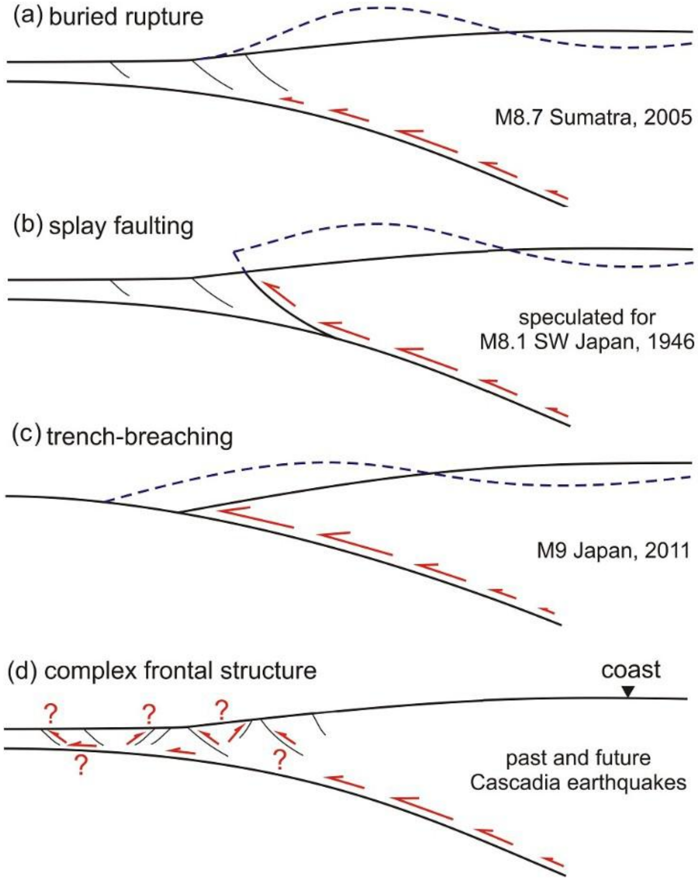

Figure 3.1. Four rupture scenarios of subduction zone earthquakes for generating tsunamis [*Wang and Trehu*, 2015]. Red arrows represent coseismic slip. Dashed lines represent seafloor deformation. (a) Buried rupture. (b) Splay faulting rupture. (c) Trench-breaching rupture. (d) Activation of multiple thrusts and back-thrusts.

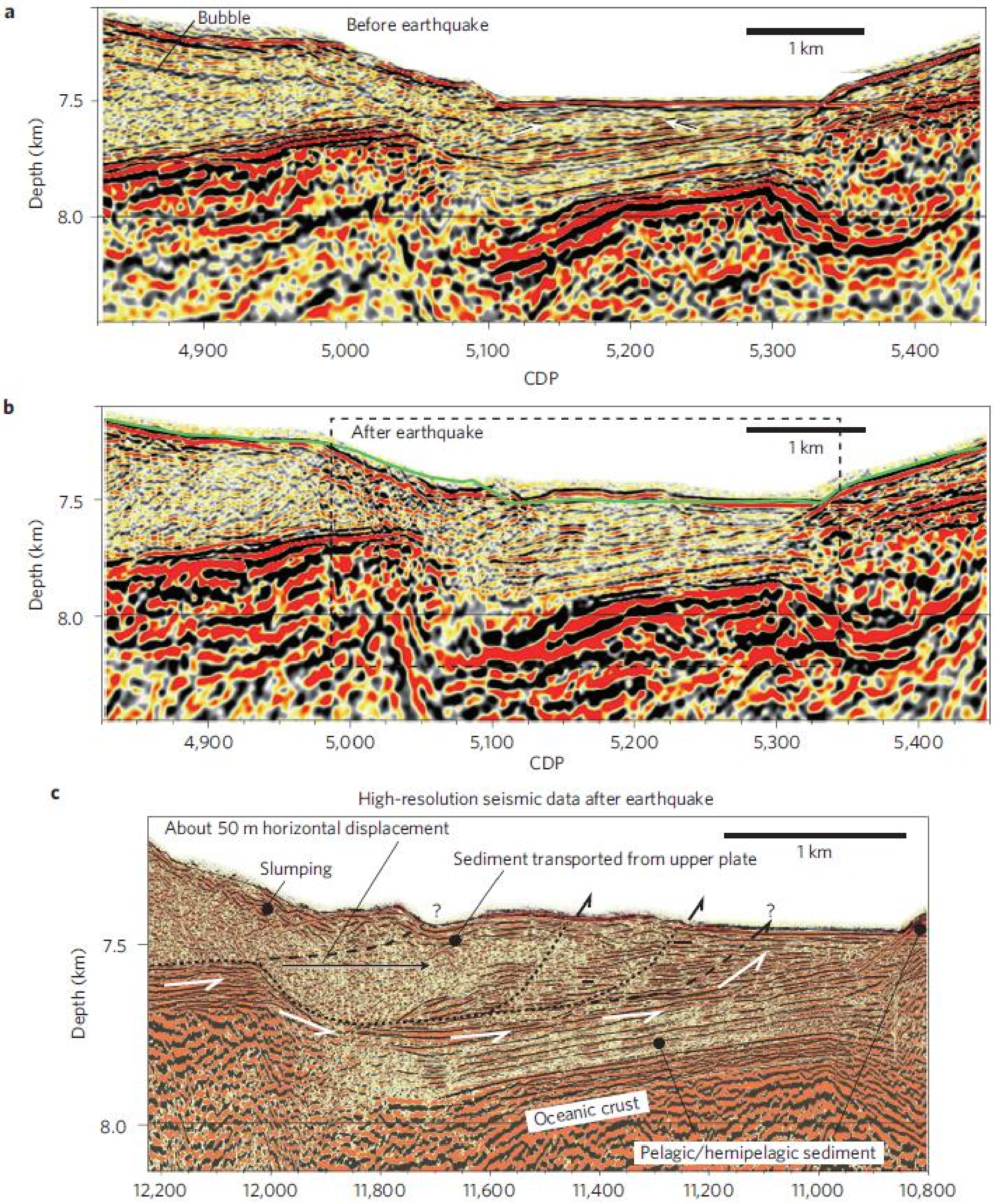

Figure 3.2. Seismic imaging of the Japan trench area obtained before and after the 2011 Tohoku-Oki earthquake [*Kodaira et al.*, 2012]. CDP, common depth point. (a) Seismic image obtained before the earthquake with vertical exaggeration 2:1. (b) Seismic image obtained after the earthquake with vertical exaggeration 2:1. Seafloor before the earthquake is marked by a green line. (c) Interpretation of the seismic image obtained after the earthquake within the dashed rectangle shown in (b).

The 2011 M_w 9.0 Tohoku-Oki earthquake raised a new question for Cascadia hazard analyses. Numerous studies based on seismic [e.g., *Ide et al.*, 2011], geodetic [e.g., *Iinuma et al.*, 2012; *Ozawa et al.*, 2012], and tsunami [e.g., *Satake et al.*, 2013] data indicate that large coseismic slip extended to or near the trench axis (Figure 3.1c). The trench-breaching rupture of the 2011 Tohoku-Oki earthquake was more directly revealed by repeated multibeam bathymetry measurements [*Fujiwara et al.*, 2011] and high-resolution seismic imaging of the trench area [*Kodaira et al.*, 2012] before and after the earthquake. The large differences between pre- and post-earthquake bathymetry at the trench [*Fujiwara et al.*, 2011] and newly developed upheaval structure in the trench sediment as a result of the earthquake (Figure 3.2b) [*Kodaira et al.*, 2012] both suggest a trench-breaching rupture. During the coseismic slip, the rupture may have propagated along the master fault (Figure 3.2c, whites arrows) causing horizontal shortening of the trench sediment [*Kodaira et al.*, 2012].

Unlike the sediment-starved Japan trench where one continuous décollement extends all the way to the trench, a structure style that facilitates slip-to-trench rupture, the trench at Cascadia is buried by large amounts of sediment (~3 km) (Figure 3.1d). Can the shallowest portion of the Cascadia megathrust also slip to the trench in great earthquakes as in the Tohoku-Oki earthquake, or would it normally resist coseimic rupture but creep aseismically after the earthquake as in the 2005 M_w 8.7 Nias earthquake? Similar to Cascadia, the Sumatra trench is also covered by very thick (over 4 km) sediment [*Gulick et al.*, 2011]. Multiple thrusts and back-thrusts are present in the sediment near the

Sumatra trench [*Henstock et al.*, 2006; *Singh et al.*, 2008; *Gulick et al.*, 2011]. Seismic [*Singh et al.*, 2008; *Gulick et al.*, 2011] and high-resolution bathymetry [*Henstock et al.*, 2006] studies suggest that the cosesimic fault slip during the 2004 M_w 9.2 Sumatra megathrust earthquake may have propagated updip close to the trench or even breached the seafloor. However, available seismic and geodetic data do not provide convincing evidence to confirm this. About 20 earthquakes occurred on the Cascadia megathrust over the recent 10,000 years [*Atwater et al.*, 1995; *Goldfinger et al.*, 2012]. If the previous megathrust ruptures breached the seafloor at Cascadia, there should be strong evidence in the deformed sediment formation in the deformation front area. Therefore, to investigate the possibility of slip-to-trench rupture during megathrust earthquakes at Cascadia, I reanalyzed the seismic images from marine multichannel seismic surveys conducted in 1985 and 1989 with a new focus on the accretionary wedge deformation front.

3.2. Seismic Images of the Deformation Front Area

Two marine multichannel seismic (MCS) surveys were conducted off the west coast of Vancouver Island in 1985 and 1989 by the Geological Survey of Canada. The survey profile locations are shown in Figure 3.3. Data acquisition and processing were carried out two to three decades ago by *Yorath et al.* [1987], *Clowes et al.* [1987] and *Davis and Hyndman* [1989] for the 1985 survey and *Spence et al.* [1991a, 1991b], *Hyndman et al.* [1994] and *Yuan et al.* [1994] for the 1989 survey, which represent the best effort of the time. I re-examine reflection images from ten of these profiles (Lines 89-03, 85-01, 89-04, 89-05, 89-06, 89-07, 85-02, 89-08, 89-09, and 85-04) with a new focus on the accretionary wedge deformation front.

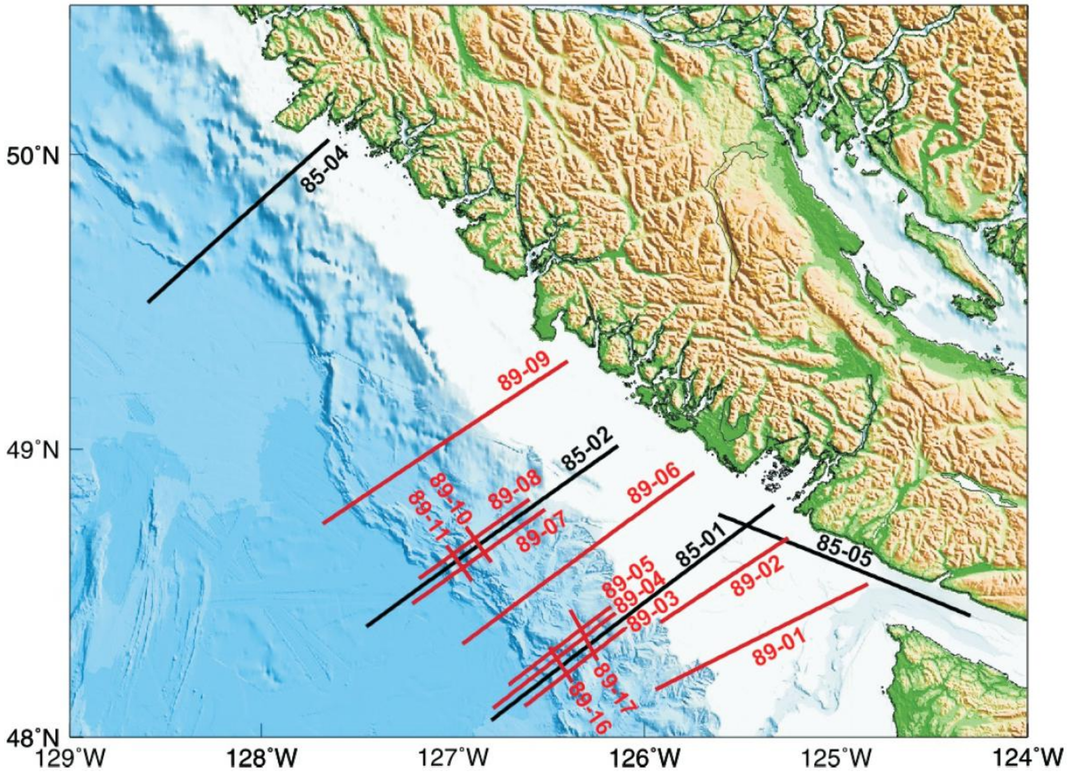

Figure 3.3. The 1985 (black lines) and 1989 (red lines) marine multichannel reflection profiles.

All the 1985 seismic survey images were presented in terms of both "depth" and "two-way travel time" in the original references [*Clowes et al.*, 1987; *Davis and Hyndman*, 1989], but those from 1989 survey were presented only in "two-way travel time" (Figure 3.4) [*Spence et al.*, 1991a; *Hyndman et al.*, 1994] except for Lines 89-04 and 89-07 from *Yuan et al.* [1994]. To obtain deformation structures near the deformation front, it would be ideal to convert the two-way travel time to depth for Lines 89-03, 89-05, 89-06, 89-08, and 89-09.

Unfortunately we have no digital velocity information for these old profiles to do a time-depth conversion on the segy-stacks in a timely fashion. One strategy would be to take the velocity information from the printed records, hand-edit them into the NMO-format, and then read them into processing package Globe Claritas for the conversion [*M. Riedel*, personal communication, 2015]. Another way is to hand-measure the "depth" and "two-way travel time" sections of Lines 89-04 and 89-07 from *Yuan et al.* [1994] to get a "two-way travel time vs depth" relation to do a quick time-depth conversion for the other lines of the 1989 survey. Given the many assumptions and simplifications in the tsunami source modelling (will be discussed in Chapter 4), the second approach is expected to be more than adequate.

From manually converted depth sections for Lines 89-03, 89-05, 89-06, 89-08, and 89-09 and the original depth sections for the other 5 lines, I picked all the landward dipping thrusts and seaward dipping back-thrusts. Figure 3.4 shows an example for how I pick these thrusts and back-thrusts. The time section of Line 89-04 is shown in Figure 3.4a. Three landward dipping thrusts (F1, F2, and F3) are present near the deformation front. F2 breaks the seafloor while the other two do not seem to. It is difficult to tell whether these three thrusts penetrate to the top of the igneous oceanic crust because of the limited data resolution. Neither is it known whether these faults were generated seismically by previous megathrust earthquakes or aseismically due to slow plate convergence. The deformation structures of Line 89-04 is sketched in Figure 3.4b. Figures 3.4c (original time section of Line 89-09) and 3.4d (the depth section form of Line 89-09 after the simple time-to-depth conversion) show more complicated deformation in which both a thrust (F4) and a back-thrust (F5) are present in the sediment. A summary of deformation structures from the 10 seismic profiles are sketched in Figure 3.5.

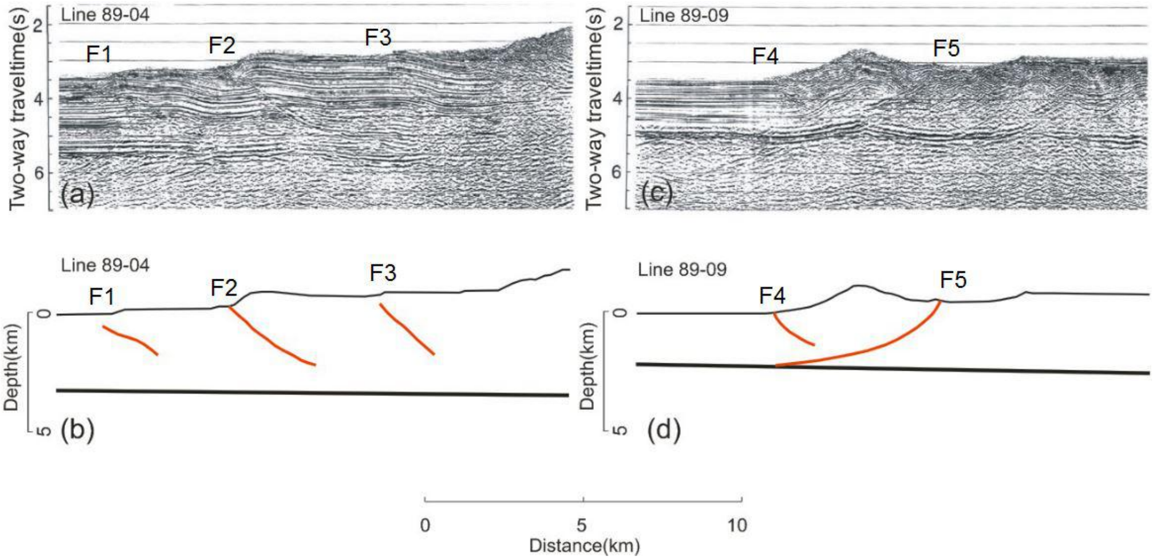

Figure 3.4. Examples of identifying potential tsunamigenic secondary faults near the deformation front. (a) Original seismic image of Line 89-04 [*Hyndman et al.*, 1994]. (b) Deformation structures of line 89-04 shown as a sketch. (c) Original seismic image of Line 89-09 [*Hyndman et al.*, 1994]. (d) Deformation structures of line 89-09 shown as a sketch.

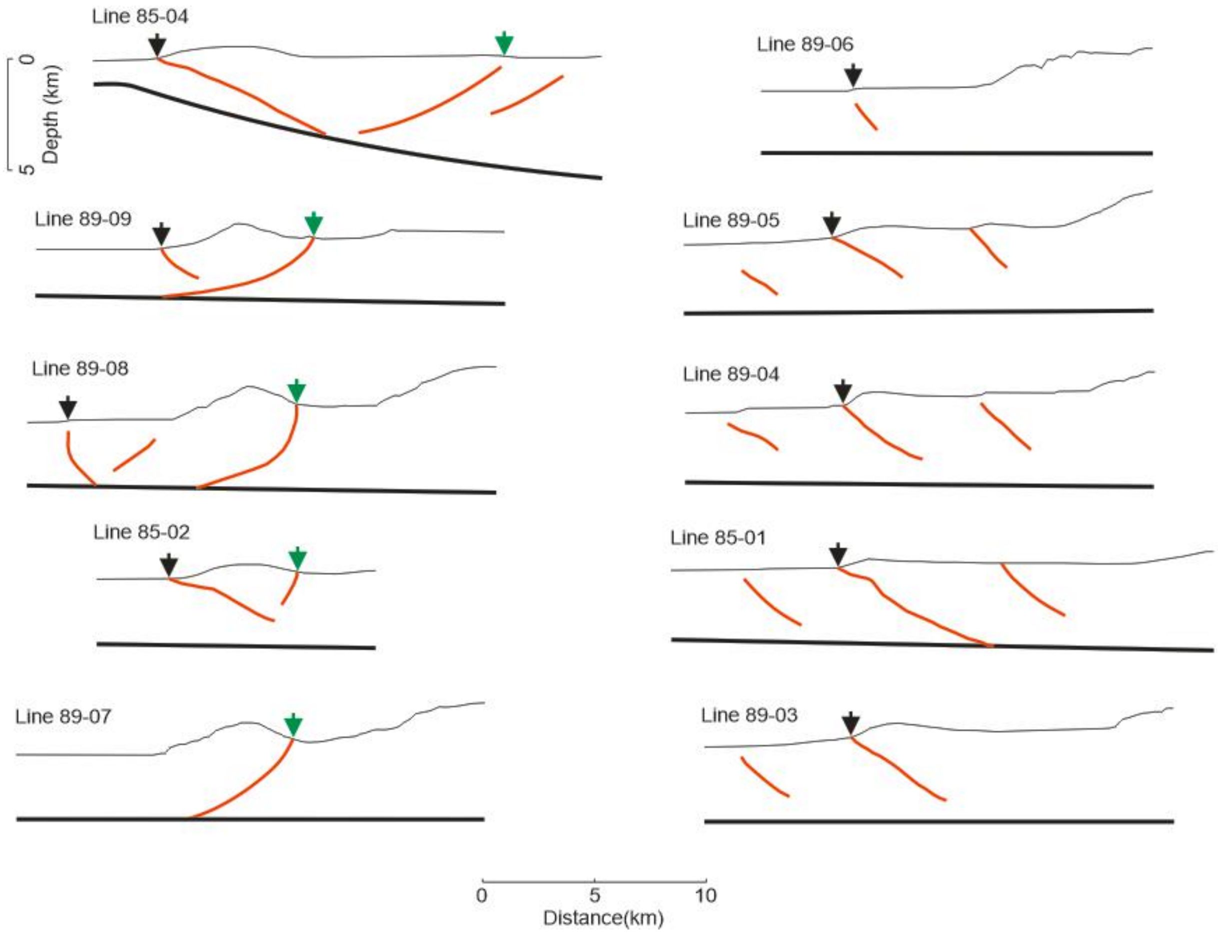

Figure 3.5. Deformation styles along the northern Cascadia margin (profile locations are shown in Figure 3.3). Black and green arrows denote the dominant frontal thrusts and back-thrusts, respectively.

3.3. Implications for Tsunami Hazard Evaluation

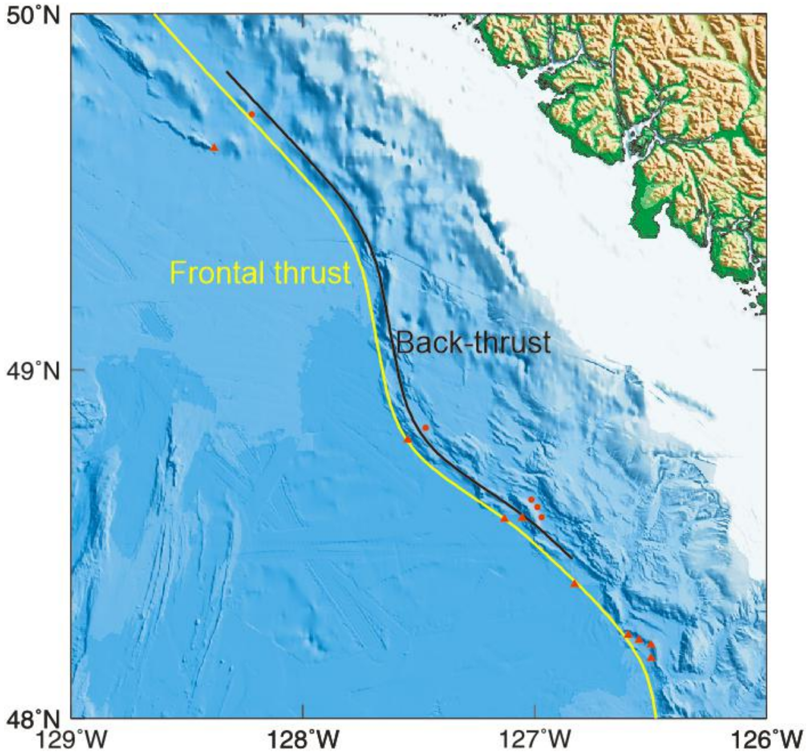

Figure 3.6. Locations of dominant frontal thrust (red triangles) and back-thrust (red dots) from seismic survey profiles (Figure 3.5). Yellow and black lines show the surface traces of our hypothetical frontal thrust and back-thrust, respectively, for tsunami source modelling.

The incoming plate at Cascadia is blanketed by ~3 km sediment near the deformation front. Off Vancouver Island, deformation style of the sediment varies along the margin (Figure 3.5). In a southern portion there are multiple thrusts dipping landward. Half-way north the vergence changes to dominantly back-thrusting. Farther north, in the Explorer segment, both seaward and landward vergent thrusts are present. If I map the locations of the dominant frontal thrusts and back-thrusts obtained from the seismic images onto the bathymetry map, it is clear that the locations of dominant frontal thrusts and back-thrusts correspond to tiny linear frontal anticlinal folds very well (Figure 3.6). Individual frontal thrusts and back-thrusts offshore of Vancouver Island are localized with very small strike lengths. Given the complex structure at Cascadia's deformation front and lack of a continuous frontal thrust and/or back-thrust which could facilitate large slip at trench (Figure 3.5), slip-to-trench rupture appears to be much less likely. Elastic seafloor deformation of the upper plate induced by a buried rupture and activation of multiple thrusts and back-thrusts due to sudden shortening of the frontal accretionary prism (Figures 3.1a, d) may be the more likely tsunami source scenarios for Cascadia. If multiple thrusts and back-thrusts are activated in megathtust earthquakes (Figures 3.1d), coseimic slip will be diverted from the décollement to these thrusts and back-thrusts. It is very uncertain how much coseismic slip should be assigned to individual thrusts and back-thrusts.

To investigate how the frontal thrusts and back-thrusts contribute to tsunami generation, I devise a hypothetical frontal thrust model and a hypothetical back-thrust model that are continuous along strike (Figure 3.6). To devise the hypothetical frontal thrust, I picked one dominant landward dipping thrust from each seismic profile (except Line 89-07 where no frontal thrust can be identified) assuming that the dominant thrust breaks the seafloor and connects to the décollement. The décollement is near the base of the sediment section as suggested by *Davis and Hyndman* [1989]. Taking Line 89-04 for example (Figure 3.7a), F2 is the dominant thrust and breaches the seafloor. I assume F2 connects to the décollement along the dashed line shown in Figure 3.7a and thus allow coseismic rupture to be diverted to the seafloor. Then I use the landward dipping thrusts obtained from the 9 seismic profiles with an average dip of ~32° to generalize a 3D frontal thrust. The frontal thrust smoothly merges with the megathrust at a depth less than ~10 km. For the hypothetical back-thrust, I also picked one dominant seaward dipping thrust from each profile (except those profiles without a back-thrust, Figure 3.5) assuming that the dominant back-thrust breaks the seafloor and connects to the décollement (Figure 3.7b). The hypothetical back-thrust dipping ~33° merges with the décollement at depth around 3 km below the seafloor. Due to the sudden compression of the frontal accretionary prism during a great megathrust earthquake, the back-thrust might be activated as shown in Figure 3.7b.

Although these two hypothetical continuous along-strike fault geometry models are unrealistic, they are adequate to help us understand how the frontal thrust and back-thrust can contribute to tsunami generation at Cascadia. I will use them to develop tsunami sources in Chapter 4. Considering other uncertainties and assumptions in the tsunami source modelling, these two representative models of rupture geometry around the deformation front are practical for tsunami hazard assessment.

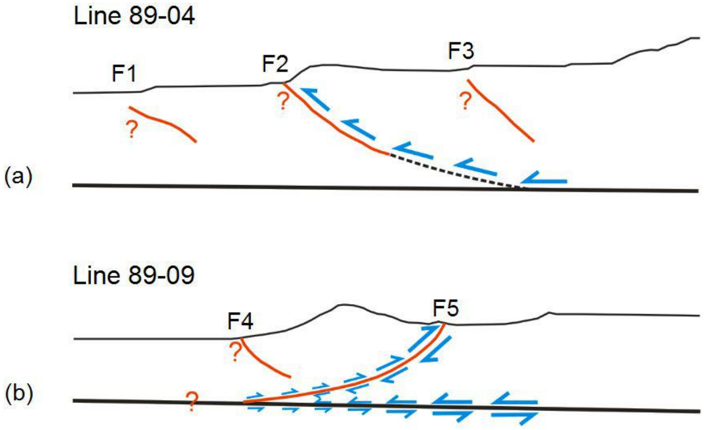

Figure 3.7. Examples showing how to devise hypothetical frontal thrust and back-thrust models. (a) Frontal thrust example. Red lines: landward dipping thrust faults. Blue arrows: assumed coseismic slip in megathrust earthquakes. I assume the dominant thrust F2 connects to the décollement along the dashed black line. (b) Back-thrust example. Red lines: landward dipping thrust and seaward dipping back-thrust. Blue arrows: assumed coseismic slip in megathrust earthquakes.

Chapter 4. Megathrust Tsunami Source Modelling

4.1. 3D Dislocation Model

In this work, tsunami sources are simulated with a 3D numerical dislocation model in a uniform elastic half-space. The computer program disl3d.f, developed by Dr. Kelin Wang, numerically integrates the point-source dislocation solution (Green's function) of *Okada* [1985] over a 3D megathrust and yields displacement at observation points on the upper surface of the model (Figure 4.1a). The modelling contains three steps: constructing a 3D fault mesh, assigning slip vectors, and calculating seafloor deformation. Details are described below.

4.1.1. Constructing 3D Fault Mesh

For numerical integration, a real fault needs to be divided into integration elements with each element representing a point source. Thus deformation at a surface observation point is the sum of the contributions from all the elements (Green's functions). In map view, the real megathrust can be defined by two curved boundaries along-strike: the updip and downdip boundaries (Figure 4.1). It is convenient to construct a 2D rectangular mesh first and then map the mesh on to the real 3D fault with the curved strike boundaries. Another main convenience for using a 2D rectangular mesh is that it is easy to carry out mathematical operations on fault slip distribution along both dip and strike direction easily before mapping them to the real fault (I will discuss this in section 4.1.2).

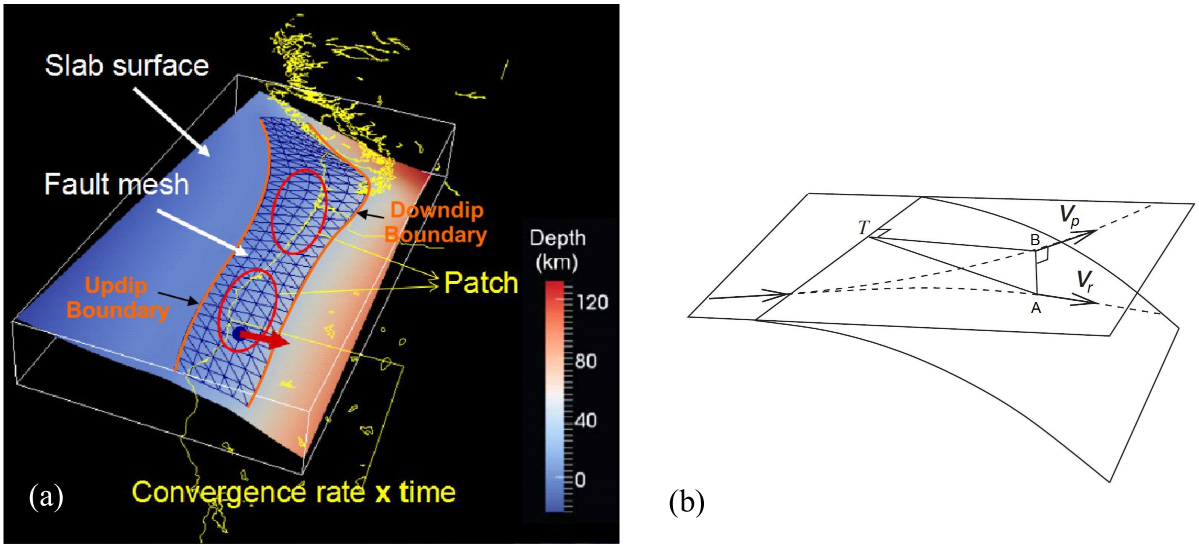

Figure 4.1. Dislocation model. (a) Fault mesh for Cascadia [modified from *Wang*, 2012]. Very large triangular elements are shown here to illustrate the concept. The triangles actually used for numerical integration are much smaller. In particular, meshes for the splay fault, frontal thrust, and back-thrust are very dense near the updip edge with element dimensions of a few hundred metres. (b) Illustration of the concept of the pseudo-slip vector [modified from *Wang et al.*, 2003]. For any real slip vector V_r on the fault (point A), the corresponding pseudo-slip vector V_p is simply the V_r rotated into the horizontal plane around the local fault strike axis, with position at the surface point B directly above A. When calculating deformation, the pseudo-slip vector will be rotated back into the local fault surface by disl3d.f.

The length and width of the 2D rectangular mesh can be arbitrary. However, using a length and width comparable to the real dimensions of the strike and width, respectively, of the fault will minimize element distortion during 2D-3D mapping. A mesh with interconnected triangular planar elements is highly preferred because triangles can accommodate any arbitrarily curved fault geometry better than planar elements of other shape do. Computing time is proportional to the mesh density. An uneven element size distribution can offer an optimal trade-off between solution accuracy and computing efficiency if we need very high mesh density in only limited areas of the fault.

In this study, I first construct a 2D rectangular mesh with coordinates (*i*, *j*), where the *i*-axis is in the strike direction and *j*-axis is in the dip direction. The mesh consists of uneven triangular elements typically with higher density for the shallow part of the fault. Then I map the 2D rectangular mesh to the fault with curved along-strike boundaries in geographic coordinates (latitude, longitude). Depth values are then assigned to the fault mesh nodal points to get a 3D fault mesh. The depth information comes from a gridded plate interface geometry (to be discussed in section 4.2).

4.1.2. Assigning Slip Vectors

Fault slip vectors are assigned at the mesh nodal points within a slip patch, a portion of the fault mesh (Figure 4.1a). The nodal slip vectors are supplied in the form of pseudo-slip vectors. The pseudo-slip vector is simply the real slip vector rotated into the horizontal plane around local fault strike axis (Figure 4.1b). The azimuth (angle clockwise from north) of the strike axis minus the rake (the hanging wall movement relative to the strike direction during a rupture) of the real slip vector defines the azimuth α of the pseudo-slip vector. If the magnitude of the slip vector is s, the pseudo-slip vector can be divided into two components: $s\cos\alpha$ (north) and $s\sin\alpha$ (east). For calculating deformation with disl3d.f, the pseudo-slip vector will be rotated back into the local fault surface.

Slip vectors can be assigned in different ways. They can be assigned directly, imported from a known slip model, or calculated based on relative plate motion. If the fault slip direction is to be based on relative plate motion, it is convenient to calculate the magnitude and azimuth of pseudo-slip vectors separately. If we want to scale the fault slip along dip and/or strike direction, we only need to consider how to scale the magnitude.

The magnitude is calculated on the rectangular 2D fault mesh by scaling a uniform value in both the dip (*j*) and strike (*i*) directions. A 1D function proposed by *Wang and He* [2008], with typos corrected in *Wang et al.* [2013], for shaping the magnitude in the downdip direction is reproduced as follows

$$s(j') = s_0\delta(j')\{1+\sin[\pi\delta(j')]^b\}\,, \tag{4-1}$$

$$\delta(j') = \begin{cases} \dfrac{6}{q}j'^2\left(\dfrac{q}{2}-\dfrac{j'}{3}\right) & 0 \le j' \le q \\ \dfrac{6}{(1-q)^3}(1-j')^2\left(\dfrac{1-q}{2}-\dfrac{1-j'}{3}\right) & q \le j' \le 1 \end{cases} \tag{4-2}$$

where $j' = j/w$ is the ratio of downdip distance j from the upper limit of the rupture zone to the downdip width *w*, s_0 is maximum slip, *b* is a broadness parametre ranging from 0 to 0.3, and *q* is a skewness parametre ranging from 0 to 1. The symmetric bell shape slip distribution with $b = 0.2$ and $q = 0.5$ has been applied in a number of studies (e.g., *Priest et al.* [2009, 2010, 2013, 2014], *Wang et al.* [2013], *Witter et al.* [2011, 2012, 2013]) for megathrust rupture modelling at Cascadia and is used for all the buried-rupture models in this work. Its variations can be used to model splay faulting and trench-breaching ruptures (Figures 4.2). If needed, slip magnitude variation along the strike direction is controlled by scaling the magnitude with the local relative patch width $(w/w_{max})^n$, where w is the local width of the slip patch, w_{max} is the maximum width of the patch, and $n \geq 0$ [e.g., *Wang et al.*, 2013]. Hence the widest part of the patch has the largest peak slip.

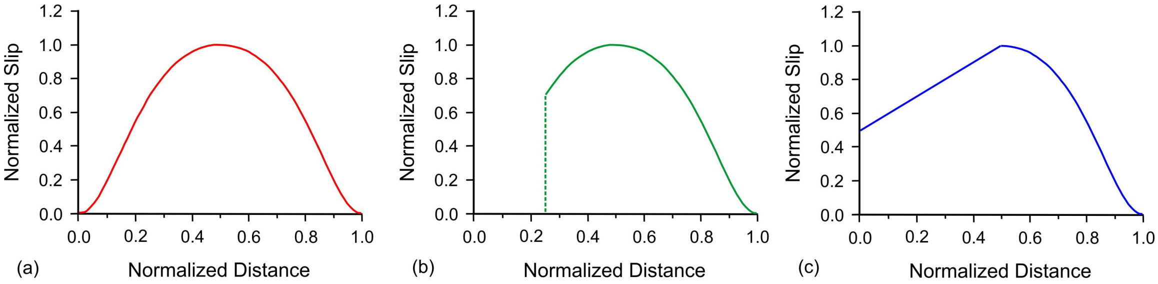

Figure 4.2. Normalized slip along the downdip direction [Modified from *Wang et al.*, 2013]. (a) A symmetric bell shape slip distribution with $b = 0.2$ and $q = 0.5$ which is used for all the buried rupture models in this work. (b) The symmetric bell shape slip distribution truncated by the surface trace of a splay fault which is used for the splay faulting rupture scenarios in this work. (c) Half-bell shape slip distribution plus a linear decrease from the peak slip towards the updip limit (straight line segment) which is used for the trench-breaching rupture models in this work.

The azimuth of the pseudo-slip is obtained on the real fault mesh but with depth ignored, as if all fault mesh nodal points have the same depth. It can be either directly assigned to all nodal points in the patch or calculated for each node from Euler vectors of relative plate motion. If the azimuth is obtained from Euler vectors, the slip magnitude is determined as an equivalent time of slip deficit accumulation which is a product of equivalent time (in years) and the local plate convergence rate. In this work at Cascadia, I determine the slip vector for each node using Euler vectors in exactly the same way as in *Wang et al.* [2003]. The direction of the slip is assumed to be exactly opposite of plate convergence between the Juan de Fuca plate and the Cascadia forearc [*Wang et al.*, 2003].

4.1.3. Calculating Seafloor Deformation

For numerical integration, the point-source dislocation at the centre of gravity of each triangular element is defined by the average fault slip of the three nodal points of the element. The product of the average slip and the area of the element is the "strength" of the point dislocation. Deformation at an observation point on the upper surface of the elastic half space with a Poisson's ratio of 0.25 is calculated by integrating the contributions from all the point sources over the entire fault mesh. Only one elastic modulus is independent in this solution. Since the deformation calculation is performed in a Cartesian system (x, y, depth), the fault mesh generated in geographic coordinates (latitude, longitude, depth) (section 4.1.1) should be converted to the Cartesian system first with appropriate projection method with orientation x-north, y-east, and z-down at the centre of map projection. For Cascadia, I use the Lambert Conformal projection for minimum distortion. After the dislocation calculation in the Cartesian system is done, the results (also in the Cartesian system) can be converted back into geographic coordinates (latitude, longitude) using the same projection method.

With point-sources represented by finite-size fault elements, it is not possible to calculate deformation right on the fault surface. In the case of a fault that breaches the top surface (e.g., frontal thrust, back-thrust, splay fault), the observation points for calculating surface deformation cannot be right on the fault trace. But the surface deformation near the fault can be approximately obtained by choosing observation points very close to the fault trace. If the offset of the observation point from the fault trace is too large, we cannot accurately describe near-fault surface deformation that may be important for tsunami generation. If the offset is too small relative to the size of the fault elements, large numerical errors will occur. Comparison with the analytical solution of *Okada* [1985] for a surface-breaching rectangular fault shows that the offset of the observation points from the fault mesh should be at least four times the dimension of the fault triangle. In order to obtain accurate surface deformation near the fault trace, the mesh near the fault trace should be very fine. I typically use the mesh with element dimensions of three to four hundred metres near the fault trace in this thesis. Deeper fault elements can be much larger because the surface observation points are farther away from those elements.

To obtain a distribution of surface deformation, a surface grid of observation points with appropriate grid spacing needs to be designed. The total computing time is proportional to the number of observation points. In a buried rupture scenario in which the surface observation points are far from the fault, usually a regular observation grid can be designed. However, in the scenarios where a rupture breaches the surface, the strain variation induced by the rupture near the fault trace is very large and requires very small grid spacing. If there is no need for very small observation grid spacing away from the fault trace, an irregular observation grid can be designed allowing much denser grid spacing only near the fault trace.

4.2. New Cascadia Megathrust Geometry

In this work, I compiled a new fault geometry for the entire Cascadia megathrust. The new megathrust geometry model is based on a combination of three parts (Figure 4.3c). For southern Cascadia, the fault geometry comes from *McCrory et al.* [2012] based primarily on Wadati-Benioff zone (WBZ) hypocentres (blue box in Figure 4.3c). Compared with earlier geometry models [e.g., *Flück et al.*, 1997; *McCrory et al.*, 2004], *McCrory et al.* [2012] reveals a more complex fault geometry in the southernmost Cascadia by precise relocation of the NCSS earthquakes using *hypoDD* method. For the northern part, their model depicts a complexly curved interface that would require the subducting slab to buckle at rather short wave lengths. Such short wave-length deformation is not very likely for the subducting lithosphere and is not convincingly supported by the data used. I prefer the older, simpler and smoother geometry proposed by *McCrory et al.* [2004] which is based on wide-angle seismic reflection and refraction data for the shallow part of the fault geometry and teleseismic travel-time data and intraslab earthquake hypocentres for the deeper part (red box in Figure 4.3c). A smooth transition between the two models is assumed (Figure 4.3c).

At northernmost Cascadia (Explorer region), the LFE hypocentres determined by *Royer and Bostock* [2014] are distributed locally along a sub-horizontal plane around 35 km depth (Figure 2.3). I have devised two 2D fault geometries for the Explorer segment in Chapter 2. One is by fitting a curve passing through the average position of the LFE cluster, a simple geometry with monotonically increasing dip (Geometry 1, Fig. 2.3). The other one is a more complex geometry by fitting the locally flat shape of the LFE cluster (Geometry 2, Fig. 2.3). For tsunami generation, it is the shallowest portion of the fault where rupture can initiate and propagate that is the most critical (Chapter 2). For the shallowest offshore part, the difference between these two geometry models is very small. Here I construct a simple 3D Explorer fault geometry featuring monotonically increasing dip with depth by extrapolating mainly from the 2D Geometry 1 (yellow box in Figure 4.3c). A smooth fault geometry transition is allowed from the Explorer segment to southern Vancouver Island (Figure 4.3c).

After obtaining the megathrust geometry, slight modification of seafloor topography is applied to fault depth because the dislocation model is developed in an elastic half-space with a flat upper surface and without including actual bathymetric and topographic reliefs [*Flück et al.*, 1997; *Wang et al.*, 2003]. I modified the shallow part of the fault geometry so that the fault depth below the free surface in the model approximately corresponds to the fault depth below the seafloor [e.g., *Wang et al.*, 2013].

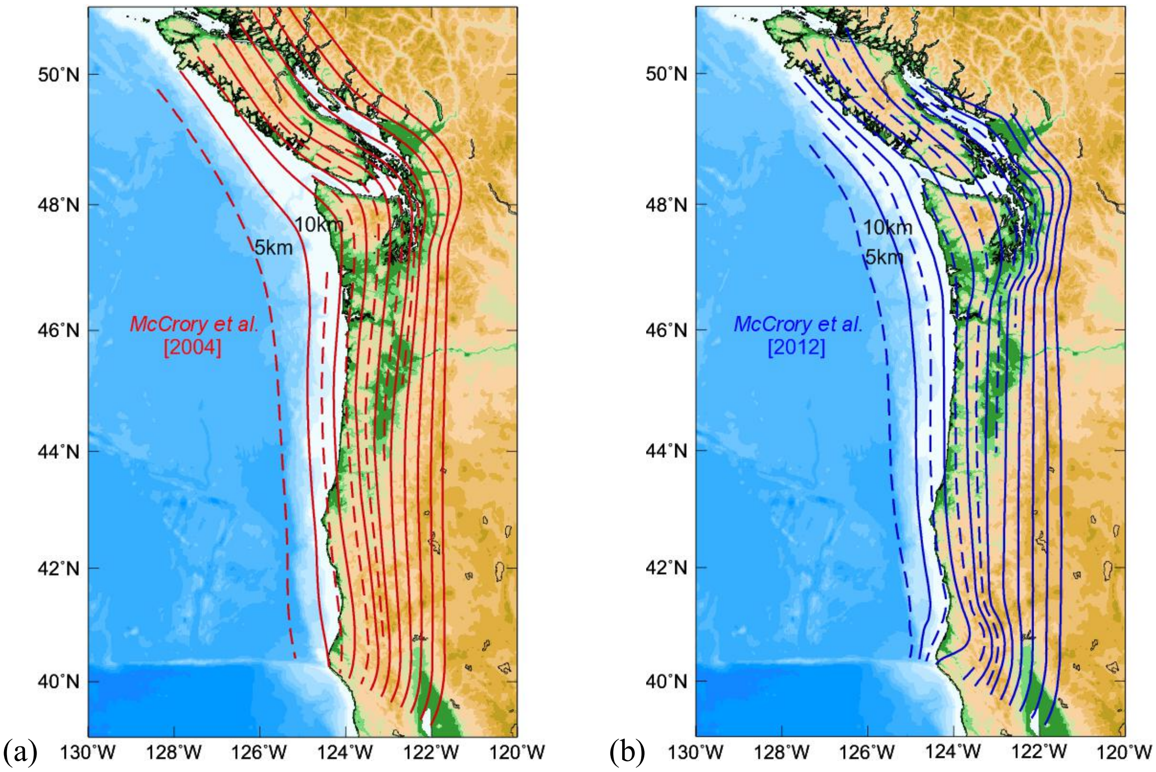

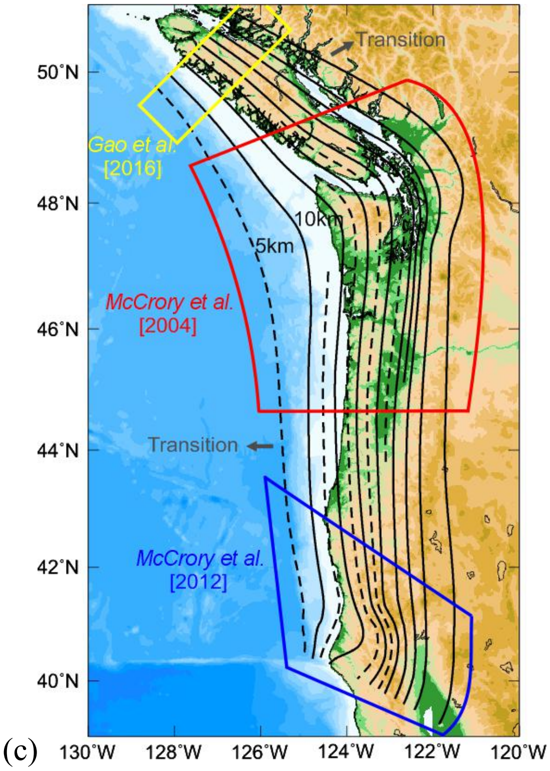

Figure 4.3. Slab depth contours. (a) Fault geometry model by *McCrory et al.* [2004]. Dashed and solid red lines indicate depth contours in 5 km and 10 km increments, respectively.
(b) Fault geometry model by *McCrory et al.* [2012]. Dashed and solid blue lines indicate depth contours in 5 km and 10 km increments, respectively.
(c) New fault geometry model for whole Cascadia compiled from *McCrory et al.* [2004], *McCrory et al.* [2012] and *Gao et al.* [2016]. *Gao et al.* [2016] is based mainly on Chapter 2 in this thesis.

4.3. Simulated Rupture Scenarios for Tsunami Hazard Assessment

For tsunami hazard assessment, I develop 21 tsunami sources (Table 4.1) in the following subsections with the 3D dislocation model (discussed in section 4.1) employing the new Cascadia fault geometry (discussed in section 4.2). The size of earthquakes representing energy released is defined using the moment magnitude [*Hanks and Kanamori*, 1979]

$$M_w = \log_{10}(M_0 - 9.1)/1.5 \tag{4-3}$$

where M_0 is the scalar seismic moment, which is the product of shear modulus, rupture area, and average fault slip.

To simulate tsunami sources, I have considered three rupture scenarios: buried rupture, splay faulting rupture, and trench-breaching rupture scenarios. The first two rupture scenarios have been considered for tsunami hazard assessment at Cascadia by a number of researches (e.g., *Priest et al.* [2009, 2010, 2013], *Witter et al.* [2011, 2012, 2013]). After reanalyzing the deformation structures near the accretionary wedge deformation front (discussed in Chapter 3), trench-breaching rupture at Cascadia seems not to be very likely compared with the first two rupture scenarios. However, for hazard assessment, we need to consider trench-breaching rupture scenarios, even though the likelihood of their actual occurrence may be low. Hence here I include the trench-breaching rupture scenarios as new potential tsunami sources at Cascadia. Additionally, I also consider both local and whole-margin ruptures (Figure 4.4), including the tectonically complex Explorer segment which has not been included for tsunami hazard assessment. A summary of tsunami sources developed in this study is given in Table 4.1, with details to be explained in subsequent subsections.

With the main focus on northernmost Cascadia, the coseismic rupture limits compiled in section 2.3 can be employed for the local ruptures at northern Cascadia. The downdip rupture limit consists of two parts (Figure 2.5): downdip rupture limit for the Explorer segment defined by this study (section 2.3) and downdip limit proposed by *Wang et al.* [2003] for the rest of Cascadia. However, by considering the whole-margin rupture, the updip and downdip limits of *Wang et al.*'s [2003] model in southern Cascadia need to be updated because their model was based on the old megathrust geometry compiled by *Flück et al.* [1997]. As explained in section 4.2, a more recent study by *McCrory el al.* [2012] reveals a complex subducting slab shape in southernmost Cascadia (Figure 4.3, section 4.2). Here I merge the downdip rupture limit north of 43 °N defined in this study and *Wang et al.* [2003] (Figure 2.5, section 2.3) with the 15 km depth contour of the plate interface south of 43 °N proposed by *McCrory el al.* [2012] as the downdip rupture limit. The exact downdip limit of the potential rupture zone in the southernmost Cascadia is less important given the northern-Cascadia focus of this dissertation. Similar to earlier work [e.g., *Hyndman and Wang*, 1995; *Wang et al.*, 2003], the updip limit is assumed to be at the deformation front, but I use a more detailed version of the deformation front (Figure 4.4a) than previously used (Figure 2.1b). The resultant updip and downdip limits of the whole-margin coseismic rupture zone are shown in Figure 4.4a with barbed and dotted black lines marking the updip and downdip limits, respectively.

Table 4.1. Summary of rupture scenarios for tsunami hazard assessment

	EX	**JDF1**	**EX+JDF1**	**Whole Margin**
Buried Rupture	B-01 (Figure 4.5a)	B-02 (Figure 4.5b)	B-03 (Figure 4.5c)	B-04 (Figure 4.5d)
Splay Faulting Rupture A	S-A1 (Figure 4.7a)	S-A2 (Figure 4.7b)	S-A3 (Figure 4.7c)	S-A4 (Figure 4.7d)
Splay Faulting Rupture B	S-B1 (Figure 4.8a)	S-B2 (Figure 4.8b)	S-B3 (Figure 4.8c)	S-B4 (Figure 4.8d)
Trench-breaching Rupture A	T-A1 (Figure 4.9a)	T-A2 (Figure 4.9b)	T-A3 (Figure 4.9c)	N/A
Trench-breaching Rupture B	T-B1 (Figure 4.10a)	T-B2 (Figure 4.10b)	T-B3 (Figure 4.10c)	N/A
Trench-breaching Rupture C	T-C1 (Figure 4.11a)	T-C2 (Figure 4.11b)	T-C3 (Figure 4.11c)	N/A

EX, Explorer segment; JDF1, northern part of the Cascadia megathrust (see Figure 4.4). The boundaries for different ruptures are shown in Figure 4.4.

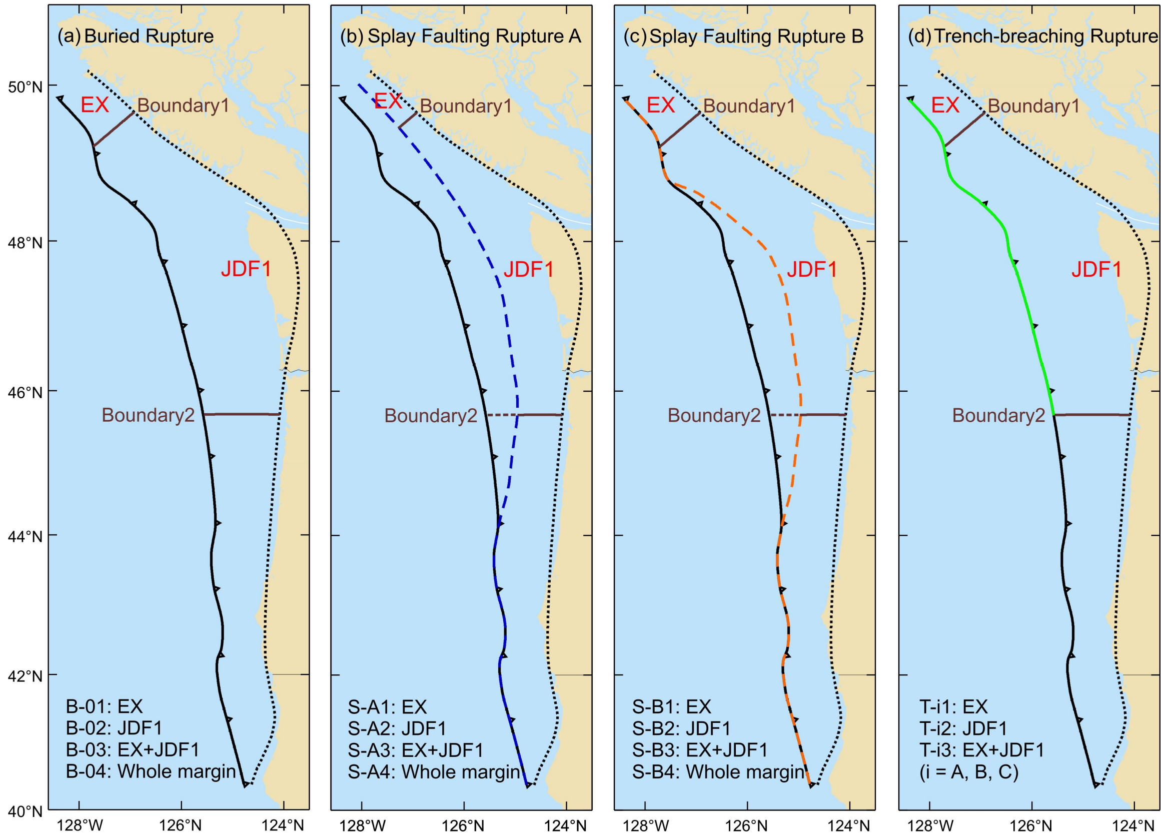

Figure 4.4. Boundary maps for (a) buried rupture, (b) splay faulting rupture A, (c) splay faulting rupture B, and (d) trench-breaching rupture scenarios. EX, Explorer segment; JDF1, northern part of the Cascadia megathrust. Boundary 1 corresponds to the Nootka Fault; boundary 2 roughly corresponds to a low-slip area during the A.D. 1700 Earthquake [*Wang et al.*, 2013]. Barbed black line in each panel shows the deformation front. Dotted black line indicates the downdip limit of the potential rupture zone. For (b), (c), and (d), the dashed blue, dashed orange, and solid green lines indicate surface traces of splay fault A, splay fault B, and frontal thrust, respectively. Frontal thrust south of the boundary 2 is not modelled in this work.

4.3.1. Buried Rupture Scenarios

Similar to earlier works at Cascadia (e.g., *Priest et al.* [2009, 2010], *Witter et al.* [2011, 2013]), I assume the fault slip peaks in the middle of the buried rupture zone and tapers to zero both updip and downdip as described by the bell-shaped function of equation (4-1, 4-2) (Figure 4.2a). As explained in section 3.1, this is based on the classical assumption that the shallowest part of the fault tends to resist coseismic rupture but allows aseismic slip after the earthquake. As explained in section 4.1.2, the slip direction in this work is determined from Euler vectors of relative plate motion, and the slip magnitude is defined by the product of an equivalent time and local plate convergence rate. I assign 500 yr of slip deficit to the apex of the bell-shape distribution in all the models (Figure 4.5) since the great megathrust earthquakes occurs at Cascadia about every 500 years on average. Because the seafloor deformation has a linear relationship with the amount of fault slip, the results can be easily scaled to obtain deformation due to other slip values.The peak fault slip varies along strike because of variations of subduction rate. A margin-normal fault slip profile (Figure 4.5c) is shown in Figure 4.6a.

I devised four buried rupture models for tsunami hazard assessment (Table 4.1), including three local ruptures and one whole-margin rupture (Figures 4.4 and 4.5). In model B-01 (Figure 4.5a), the Explorer segment north of the Nootka fault ruptures independently. In model B-02, the rupture is between the Nootka fault and a southern boundary roughly corresponding to an inferred low-slip area during the A.D. 1700 earthquake [*Wang et al.*, 2013]. Model B-03 is a combination of B-01 and B-02. Model B-04 features a whole-margin rupture. Seafloor deformation in all the four models is also shown in Figure 4.5. All the rupture models result in seafloor uplift and coastal subsidence. An example of tsunami wave propagation induced by model B-03 will be given in section 4.4.

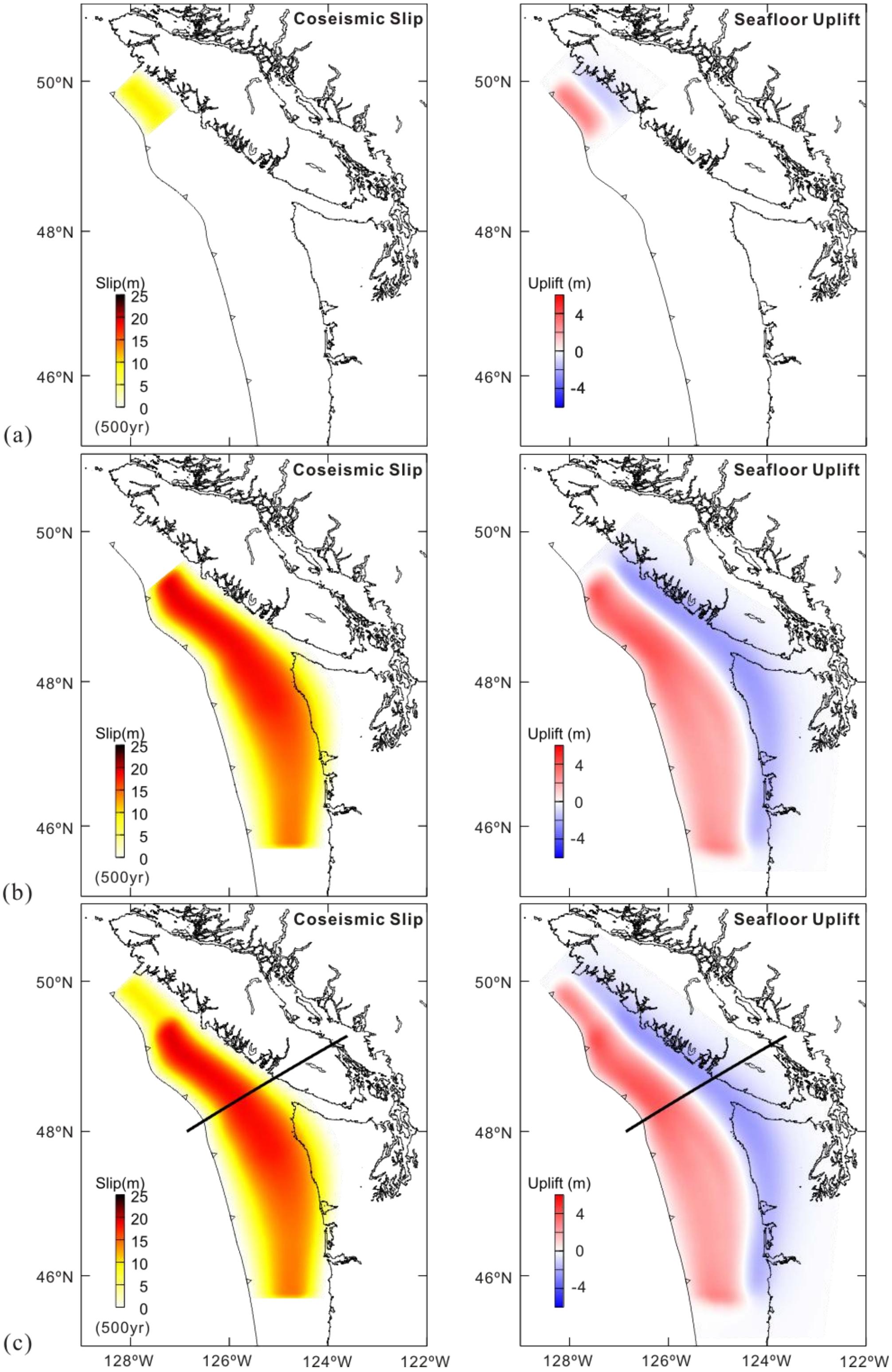
Coseismic Slip
Seafloor Uplift
50°N
48°N
46°N
Slip(m)
25
20
15
10
5
0
(500yr)
Uplift (m)
4
0
-4
(a)
(b)
(c)
128°W
126°W
124°W
122°W

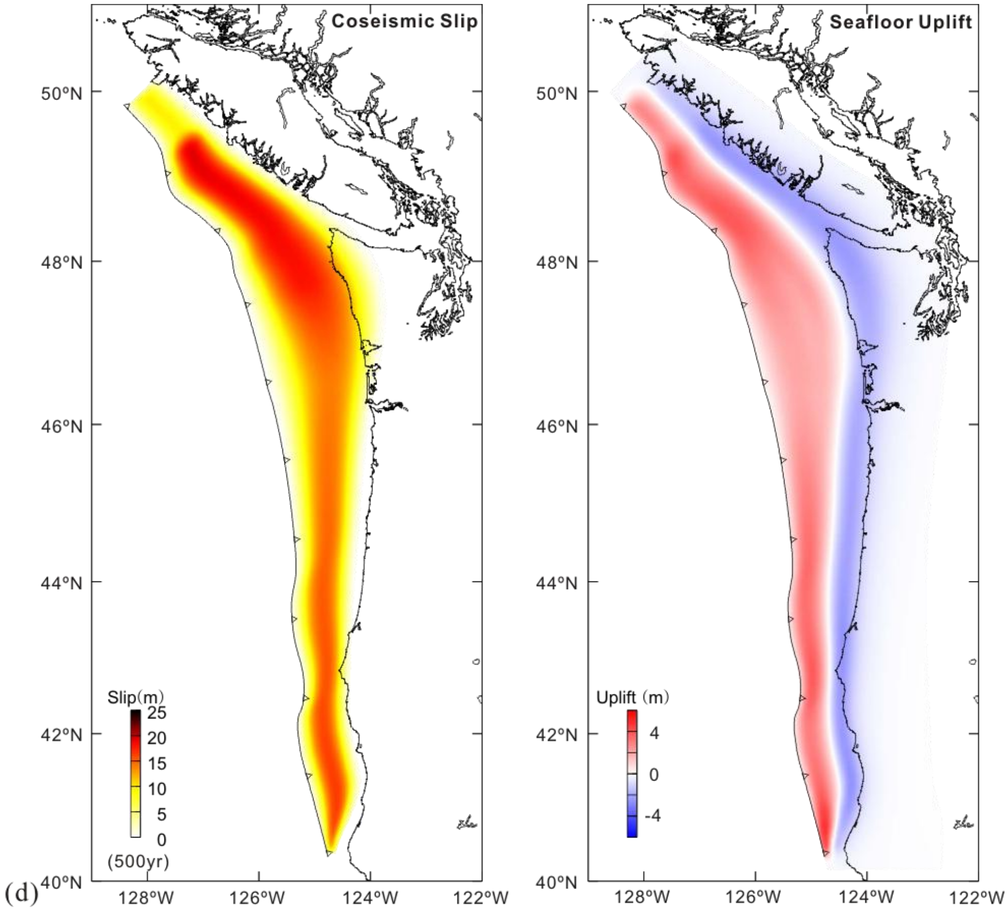

Figure 4.5. Four buried rupture scenarios. The black barbed line marks the deformation front. (a) Rupture B-01 with $M_w = 8.01$. (b) Rupture B-02 with $M_w = 8.90$. (c) Rupture B-03 with $M_w = 8.92$. (d) Rupture B-04 with $M_w = 9.05$.

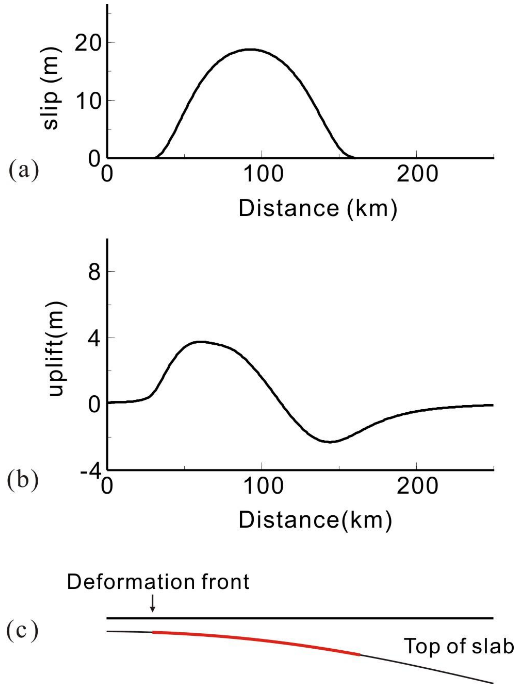

Figure 4.6. Fault slip and surface deformation along the profile shown in Figure 4.5c. (a) Fault slip along the profile. Black line: fault slip of the buried rupture (B-03) along the profile with the function (4-1,2) with a broadness of 0.2 and a skewness of 0.5. (b) Seafloor uplift along the profile. (c) Fault geometry in a cross-section view. Red line: fault slip extent along the profile.

4.3.2. Splay Faulting Rupture Scenarios

A splay fault may be present along the continental slope at central Cascadia between 45°N and 47°N offshore of Washington and Oregon [*Priest et al.*, 2009]. Whether and how far the splay fault extends northward offshore of Vancouver Island are poorly known. For tsunami hazard assessment at northernmost Cascadia, I devised two hypothetical splay fault geometries which both dip ~30° landward and merge with the megathrust at depths less than 20 km. In the first geometry (splay fault A), I extended the splay fault proposed for central Cascadia [*Priest et al.*, 2009] northward along the continental shelf edge (Figure 4.4b). In the second geometry (splay fault B), I merged *Priest et al.*'s [2009] fault with deformation front off Vancouver Island (Figure 4.4c) similar to the merging of the splay fault with deformation front at southern Cascadia [*Priest et al.*, 2009]. For southern Cascadia, both the two splay fault models merge with the deformation front as in *Priest et al.* [2009]. Without further information, the two splay fault geometry models are useful for exploring how the splay fault might contribute to tsunami generation at northernmost Cascadia.

Here I devise two groups of splay faulting rupture models based on the two splay fault geometries (Table 4.1). Each group contains four rupture models including three local ruptures and one whole-margin rupture (Figures 4.7 and 4.8). For simplicity, the fault slip is simply the buried rupture slip truncated by the surface trace of the splay fault (Figure 4.9). The fault slip and surface deformation of the splay fault models S-A3 (Figure 4.7c) and S-B3 (Figure 4.8c) are shown in Figure 4.9. Naturally, the splay faulting rupture models result in higher seafloor uplift than the previous buried rupture models do (Figure 4.6) and hence considerably amplify the tsunami. An example of how the splay fault contribute to tsunami generation will be given in section 4.4.

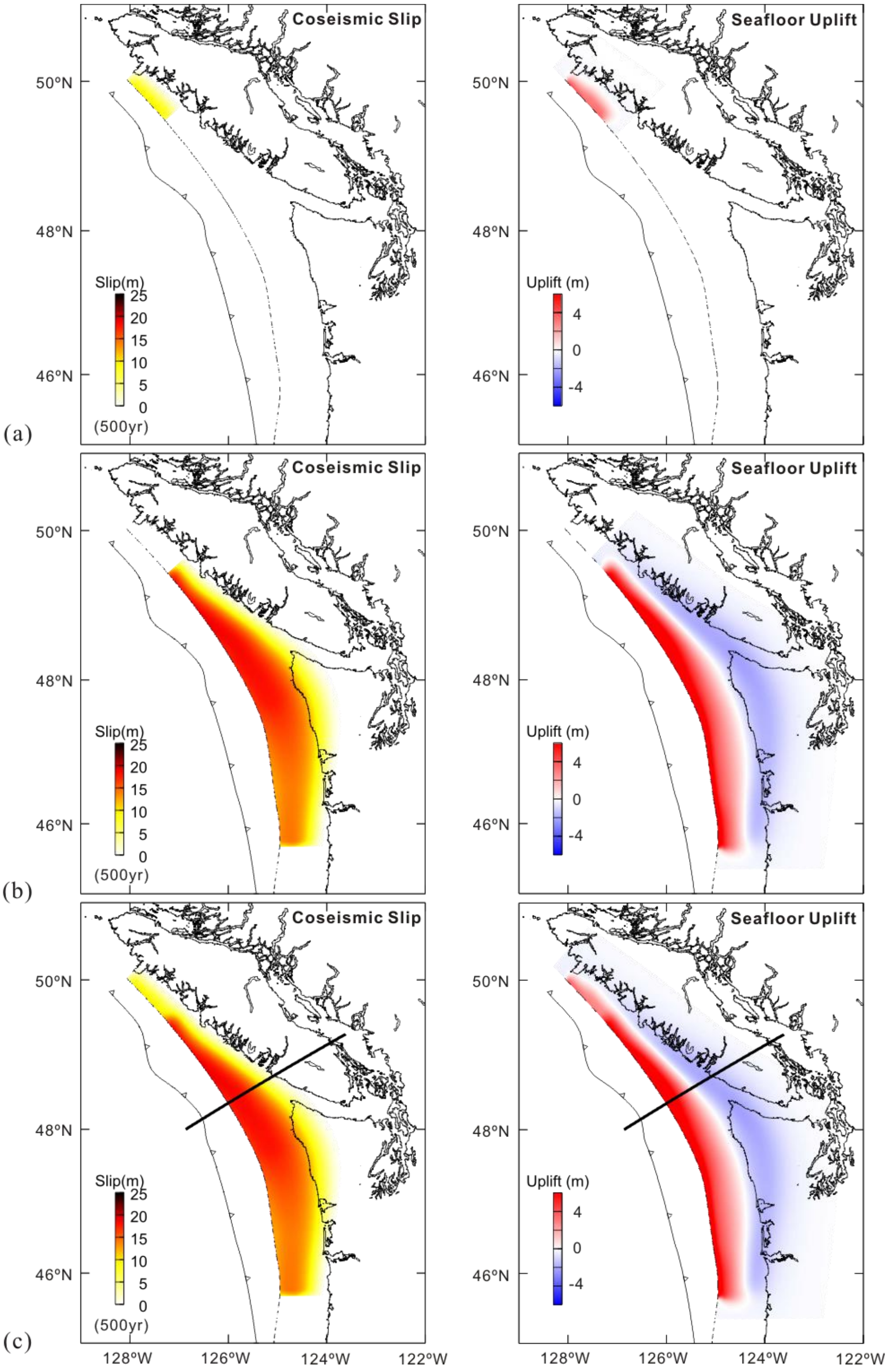
Coseismic Slip
Seafloor Uplift
Slip(m)
25
20
15
10
5
0
(500yr)
Uplift (m)
4
0
-4
50°N
48°N
46°N
128°W
126°W
124°W
122°W
(a)
(b)
(c)

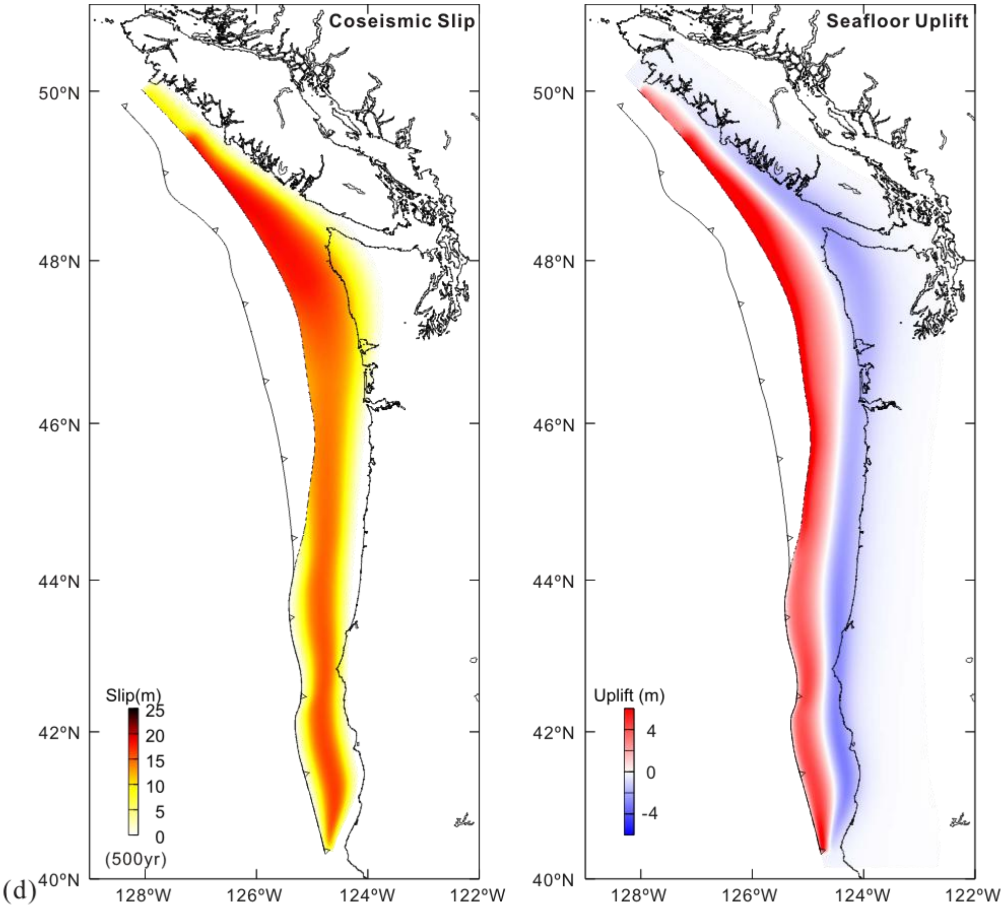

Figure 4.7. Splay faulting rupture scenarios with splay fault A. The black barbed line marks the deformation front. Dash line marks the surface trace of the splay fault. (a) Rupture S-A1 with $M_w = 7.82$. (b) Rupture S-A2 with $M_w = 8.81$. (c) Rupture S-A3 with $M_w = 8.82$. (d) Rupture S-A4 with $M_w = 8.99$.

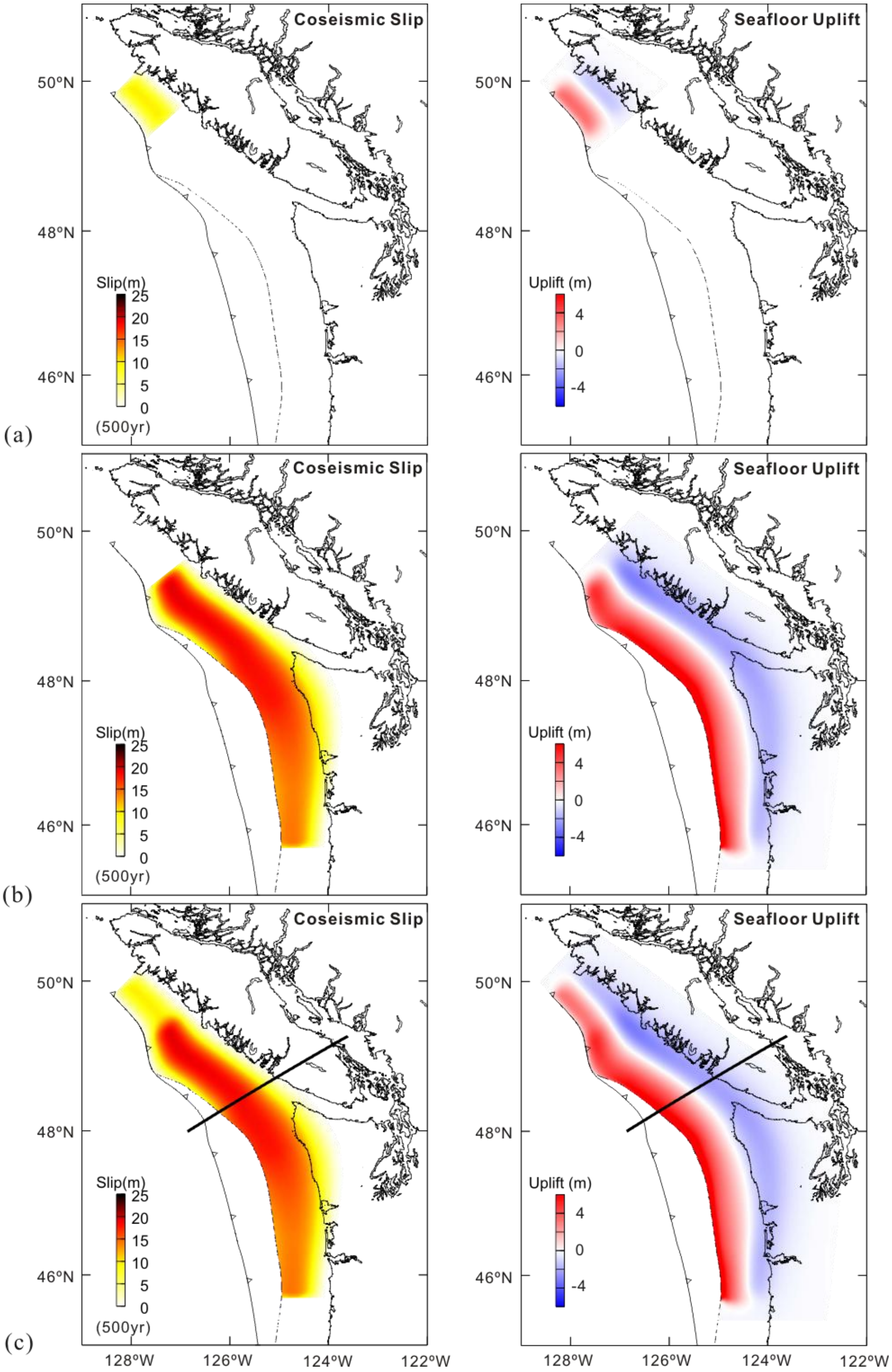
Coseismic Slip
Seafloor Uplift
50°N
48°N
46°N
Slip(m)
25
20
15
10
5
0
(500yr)
Uplift (m)
4
0
-4
(a)
(b)
(c)
128°W
126°W
124°W
122°W

(d)

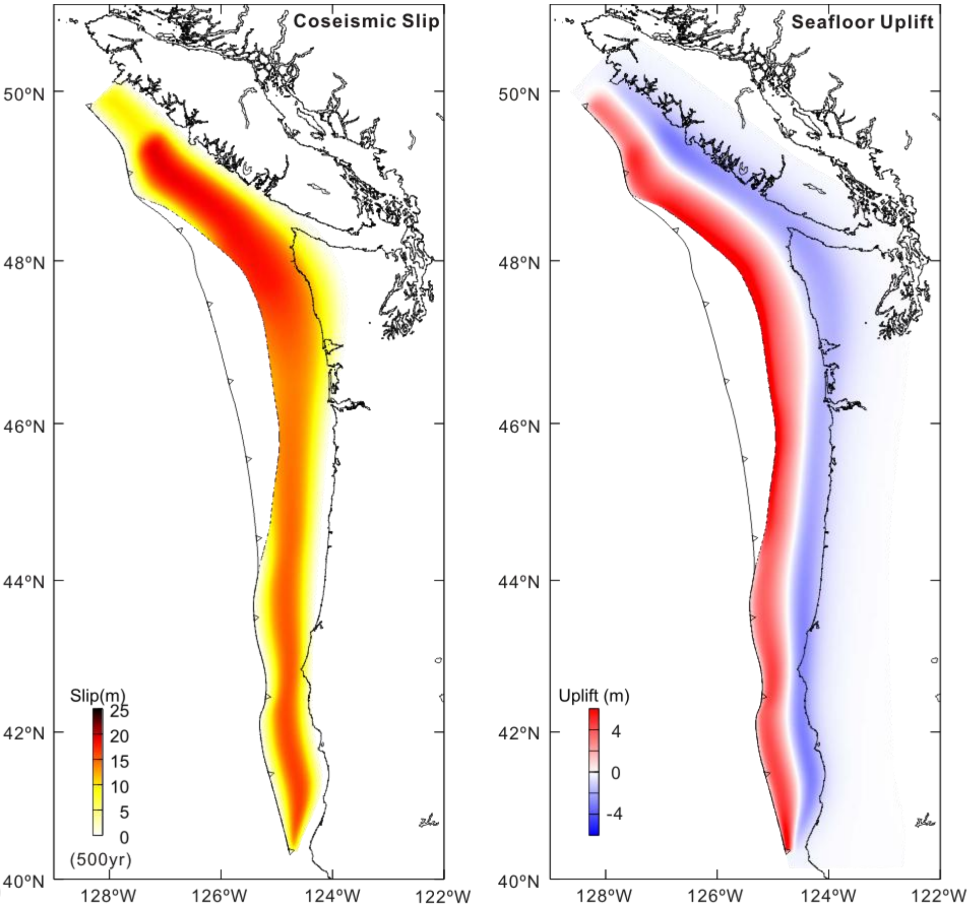

Figure 4.8. Splay faulting rupture scenarios with splay fault B. The black barbed line marks the deformation front. Dash line marks the surface trace of the splay fault. (a) Rupture S-B1 with $M_w = 8.01$. (b) Rupture S-B2 with $M_w = 8.85$. (c) Rupture S-B3 with $M_w = 8.87$. (d) Rupture S-B4 with $M_w = 9.02$.

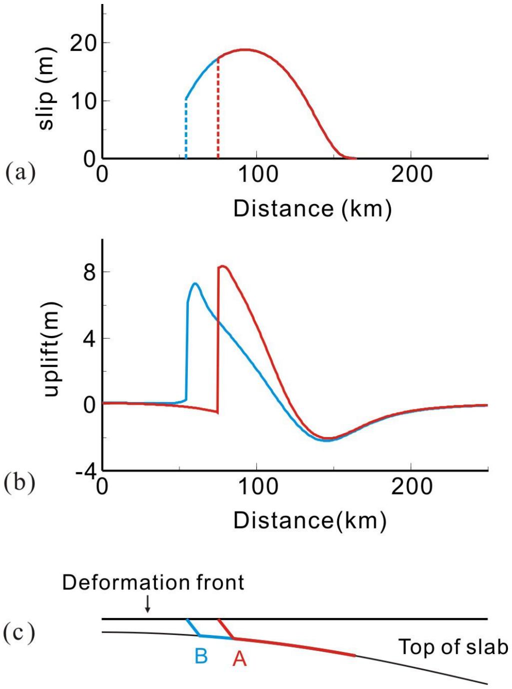

Figure 4.9. Fault slip and surface deformation along the profile shown in Figures 4.7c and 4.8c. (a) Fault slip along the profile. Red line: model S-A3; Blue line: model S-B3. (b) Seafloor uplift along the profile. Red line: model S-A3; Blue line: model S-B3. (c) Fault geometry in a cross-section view. Red line: fault slip extent along the profile with splay fault geometry A. Blue line: fault slip extent along the profile with splay fault geometry B.

4.3.3. Trench-breaching Rupture Scenarios

I devise three groups of trench-breaching models based on the hypothetical frontal thrust I proposed in section 3.3 (Figures 3.6 and 4.4). I do not consider whole-margin trench-breaching rupture here because of lack of information and because the probability for that is even much lower than the low-probability local trench-breaching rupture. Besides, for tsunami impact on the local coastal area at northernmost Cascadia, the whole-margin rupture is far less important than the local rupture. Therefore, each group of trench-breaching models here consists of only three local ruptures. The boundaries for them are shown in Figure 4.4.

In any one of the three groups, the downdip half of fault slip is exactly the same as that of a buried rupture, i.e., half bell-shaped slip (Figures 4.2 and 4.13). Slip in the updip half is assumed to change linearly from the peak in the middle of the rupture towards the surface trace of the frontal thrust. Slip at trench is 10% of peak slip in group A (T-A1, T-A2, and T-A3); 50% in group B (T-B1, T-B2, and T-B3); and 100% in group C (T-C1, T-C2, and T-C3) (see Table 4.1 and Figure 4.13). These different updip fault slip decrease rates represent different degrees of coseismic strengthening [*Hu and Wang*, 2008; *Wang and He*, 2008] or dynamic weakening [*Di Toro et al.*, 2011; *Noda and Lapusta*, 2013] of the shallow portion of the megathrust. Higher fault slip at the trench means a lower degree of coseismic strengthening to stop the rupture or a higher degree of dynamic weakening to facilitate rupture, and vice versa. The trench-breaching rupture scenarios and associated deformation are shown in Figures 4.10, 4.11 and 4.12. Obviously, the trench-breaching rupture models can amplify the seafloor uplift dramatically (Figure 4.13). In section 4.4, I will show an example of tsunami generation using the trench-breaching rupture model T-B3.

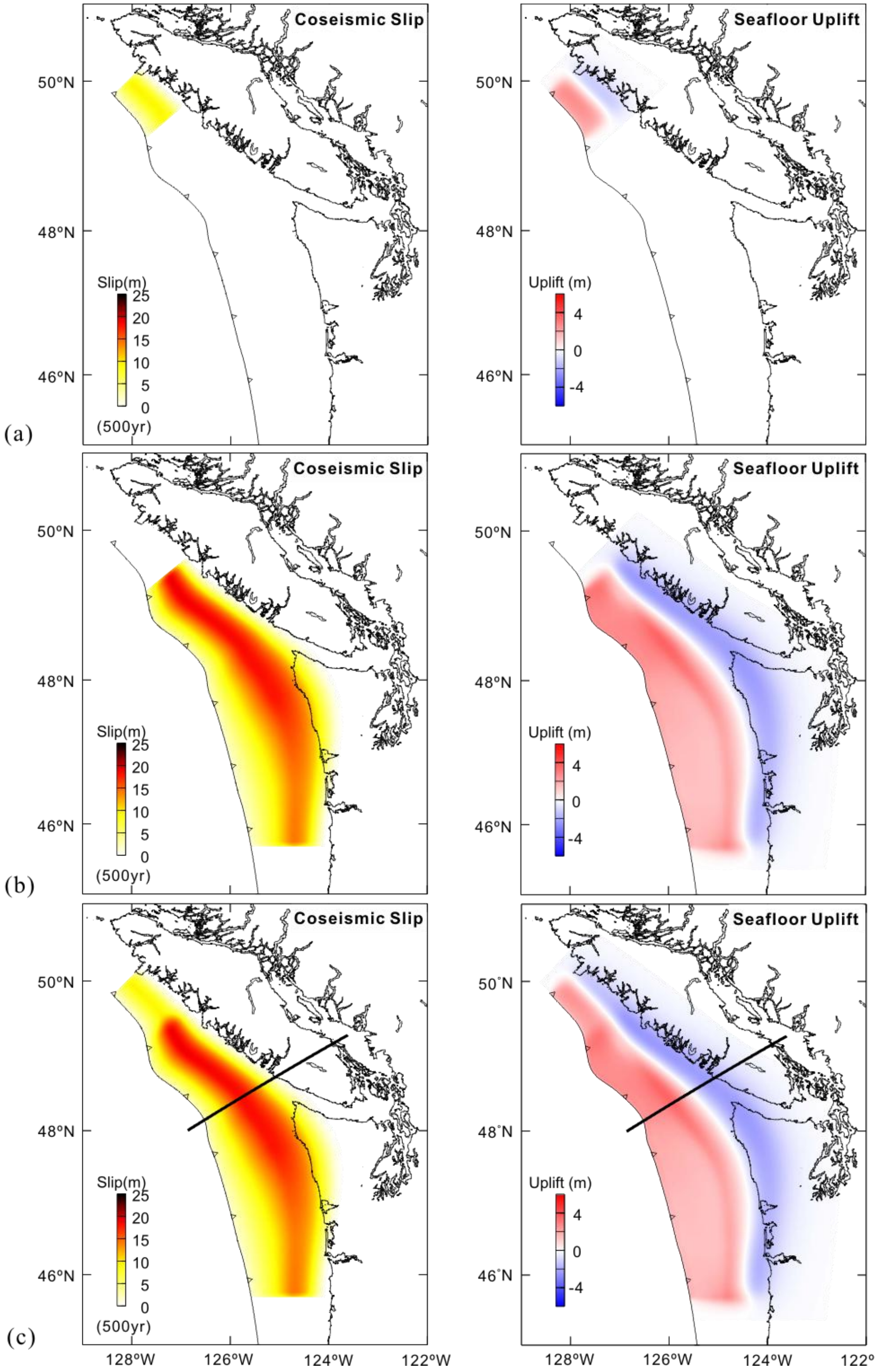

Figure 4.10. Trench-breaching rupture scenarios: group A with slip at trench = 10% of peak slip. The black barbed line marks the deformation front (also the surface trace of the hypothetical frontal thrust). (a) Rupture T-A1 with $M_w = 8.01$. (b) Rupture T-A2 with $M_w = 8.89$. (c) Rupture T-A3 with $M_w = 8.90$.

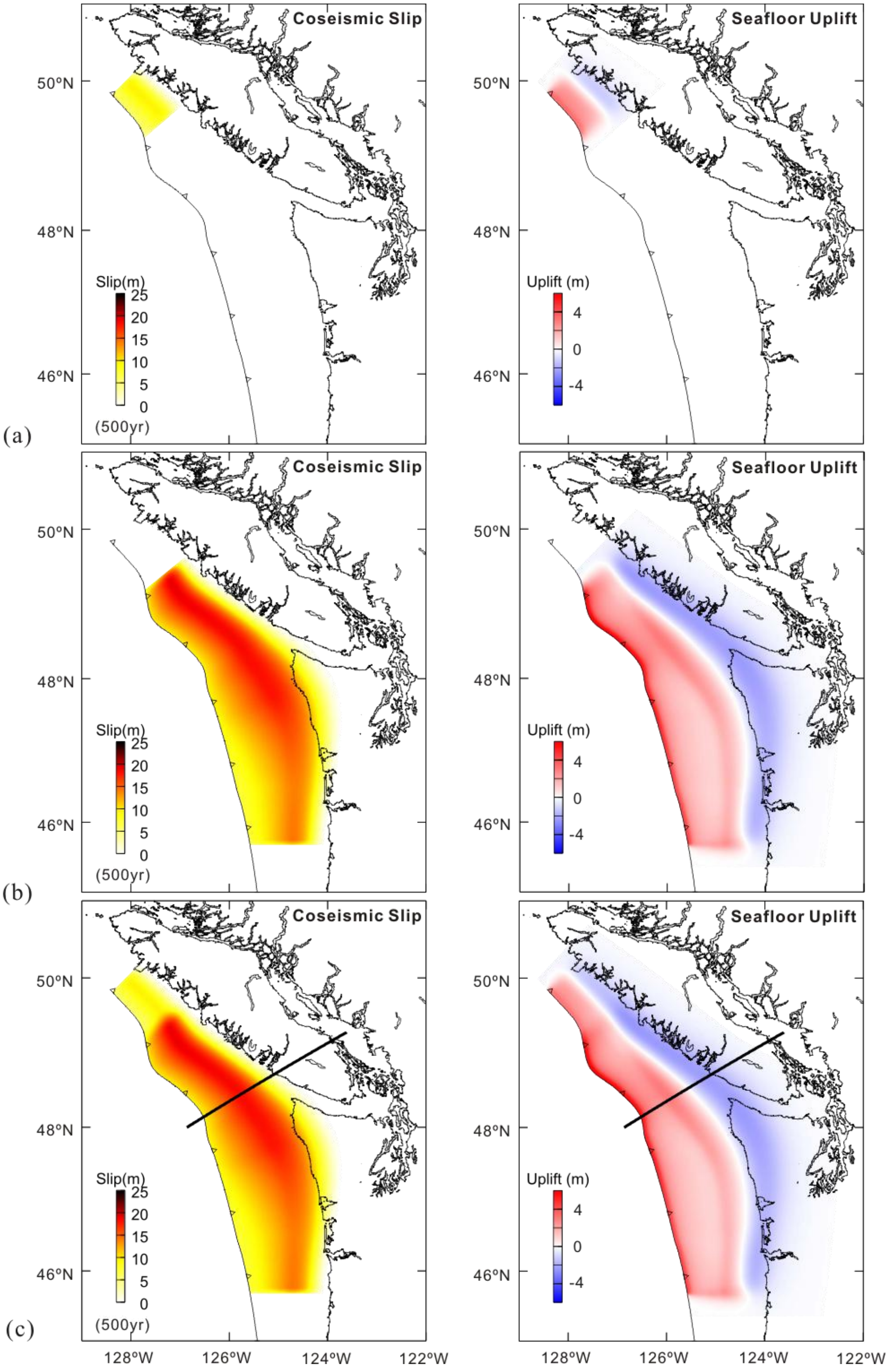

Figure 4.11. Trench-breaching rupture scenarios: group B with slip at trench = 50% of peak slip. The black barbed line marks the deformation front (also the surface trace of the hypothetical frontal thrust). (a) Rupture T-B1 with M_w = 8.06. (b) Rupture T-B2 with M_w = 8.94. (c) Rupture T-B3 with M_w = 8.95.

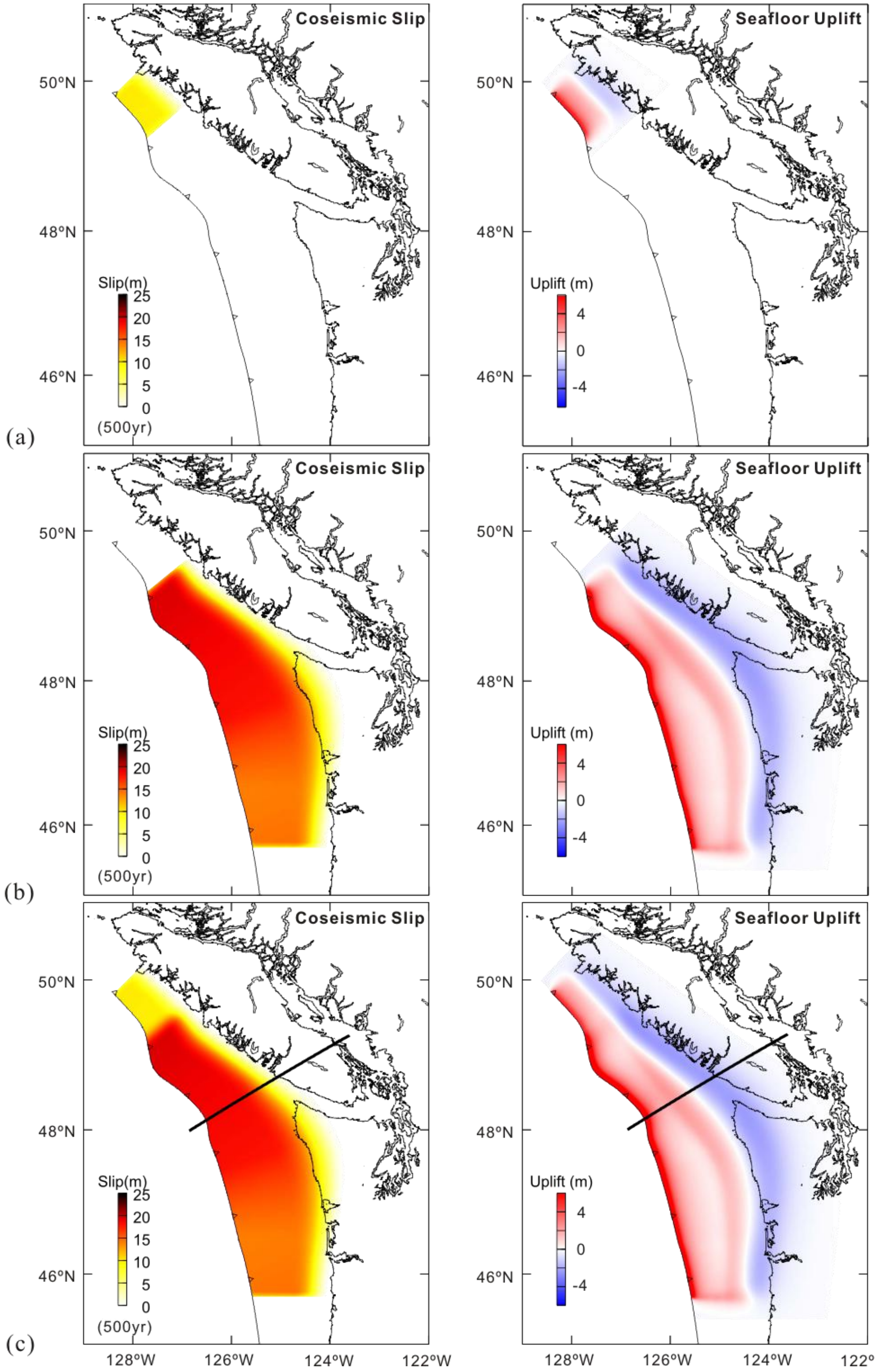

Figure 4.12. Trench-breaching rupture scenarios: group C with slip at trench = 100% of peak slip. The black barbed line marks the deformation front (also the surface trace of the hypothetical frontal thrust). (a) Rupture T-C1 with M_w = 8.11. (b) Rupture T-C2 with M_w = 8.98. (c) Rupture T-C3 with M_w = 9.00.

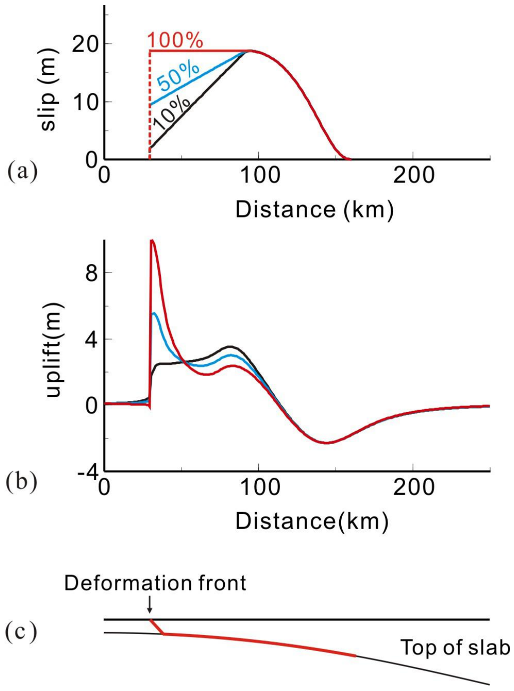

Figure 4.13. Fault slip and surface deformation along the profile shown in Figures 4.10c, 4.11c, and 4.12c. (a) Fault slip and (b) seafloor uplift along the profile. Black line: slip at trench = 10% of peak slip; blue line: slip at trench = 50% of peak slip; red line: slip at trench = 100% of peak slip. (c) Fault geometry in a cross-section view. Red line: fault slip extent along the profile.

4.3.4. Back-thrust Rupture Component Scenarios

To investigate how the back-thrusts contribute to tsunami generation, I conducted two tests for the back-thrust rupture component using the hypothetical back-thrust I devised in the section 3.3 (Figure 3.6). A symmetric bell-shaped fault slip with $b = 0.2$ and $q = 0.5$ in the dip direction (see functions 4-1,2) is assumed for the two tests (Figure 4.14). The back-thrust is very short in the dip direction and a bit longer in the strike direction. It is not very likely that such a tiny back-thrust can release a large slip deficit. Thus 50 yr and 100 yr of slip deficits are tested in the models respectively. The results are shown in Figures 4.14 and 4.15. Because of the very tiny and short wavelength seafloor deformation resulted from the long and narrow fault slip distribution, I conclude that back-thrust rupture near deformation front is unimportant for tsunami generation.

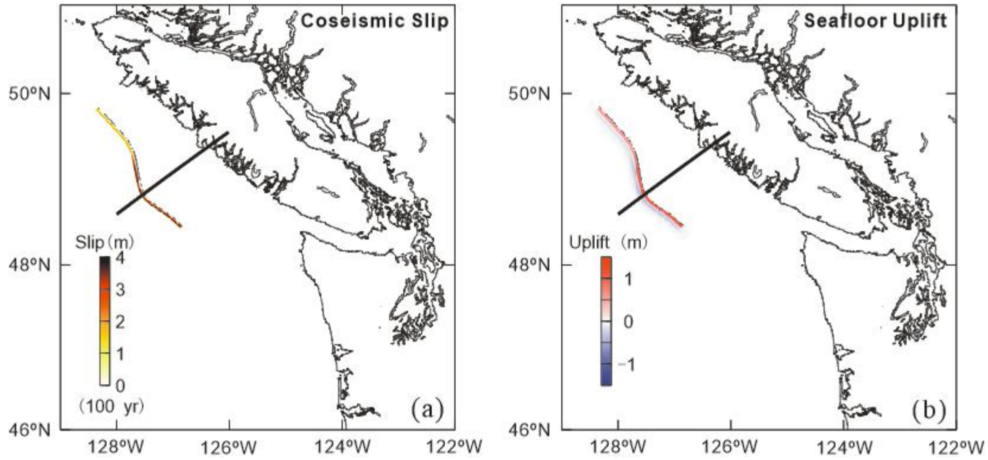

Figure 4.14. Test for the back-thrust rupture component. (a) Fault slip with 100 yr of slip deficit and (b) associated seafloor deformation.

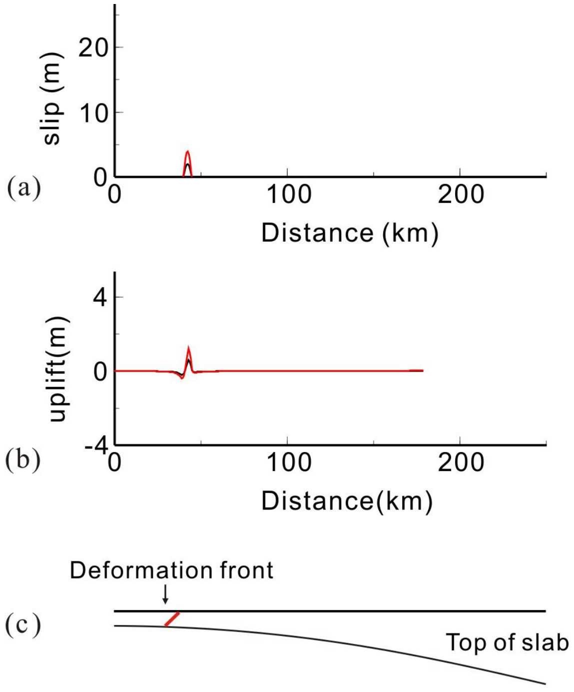

Figure 4.15. Fault slip and surface deformation along the profile shown in Figure 4.14. (a) Fault slip and (b) seafloor uplift along the profile. Black line: slip deficit = 50 yr; red line: slip deficit = 100 yr. (c) Fault geometry in a cross-section view. Red line: fault slip extent along the profile.

4.3.5. Modeled Subsidence Compared with the Observations of the A.D. 1700 Cascadia Earthquake

The source models I developed in the preceding subsections are based on the best available knowledge of the fault structure of the subduction zone and physics of rupture mechanics. The rather uniform rupture in the strike direction in these models is useful for tsunami hazard assessment and early warning. However, observations from large subduction zone earthquakes, such as the 2004 M_w 9.2 Sumatra [*Chlieh et al.*, 2007], 2010 M_w 8.8 Chile [*Lorito et al.*, 2011] and 2011 M_w 9.0 Tohoku-Oki [e.g., *Ide et al.*, 2011] earthquakes, indicate that coseismic fault slip during large earthquakes is heterogeneous (along strike).

Wang et al. [2013], mainly on the basis of foraminiferal transfer function studies, concluded the great A.D. 1700 Cascadia earthquake also exhibited heterogeneous fault slip. Employing the fault geometry proposed by *McCrory et al.* [2004], they developed a 3D dislocation model allowing the slip to vary both along strike and in the downdip directions. They proposed a rupture model with four high-slip patches separated by low-slip areas (Figure 4.16a) to explain the paleoseismic estimates of coastal subsidence (Figure 4.16e). To account for the possibility of a trench-breaching rupture, they also conducted a test in which the fault slip extends to the seafloor near the deformation front (Figure 4.16b). The coastal subsidence due to a buried rupture (Figure 4.16e, blue line) is almost identical to that due to a trench-breaching rupture (Figure 4.16e, dashed orange line). That is because the coastal deformation is not sensitive to the rupture of the most seaward part of the megathrust.

I map the fault slip of *Wang et al.*'s [2013] two rupture models to the updated Cascadia fault geometry (section 4.2). The results are shown in Figure 4.16c for the buried rupture and 4.16d for the trench-breaching rupture. The surface deformation is modelled exactly the same way as in *Wang et al.* [2013] with the 3D dislocation model (section 4.1). The model-predicted coastal deformation by this study (Figure 4.16e, purple line and dashed black line) is very similar to the results of *Wang et al.* [2013] (Figure 4.16e) because of the small difference between the old and new megathrust geometry models in the shallow part where the rupture is confined (Figure 4.3).

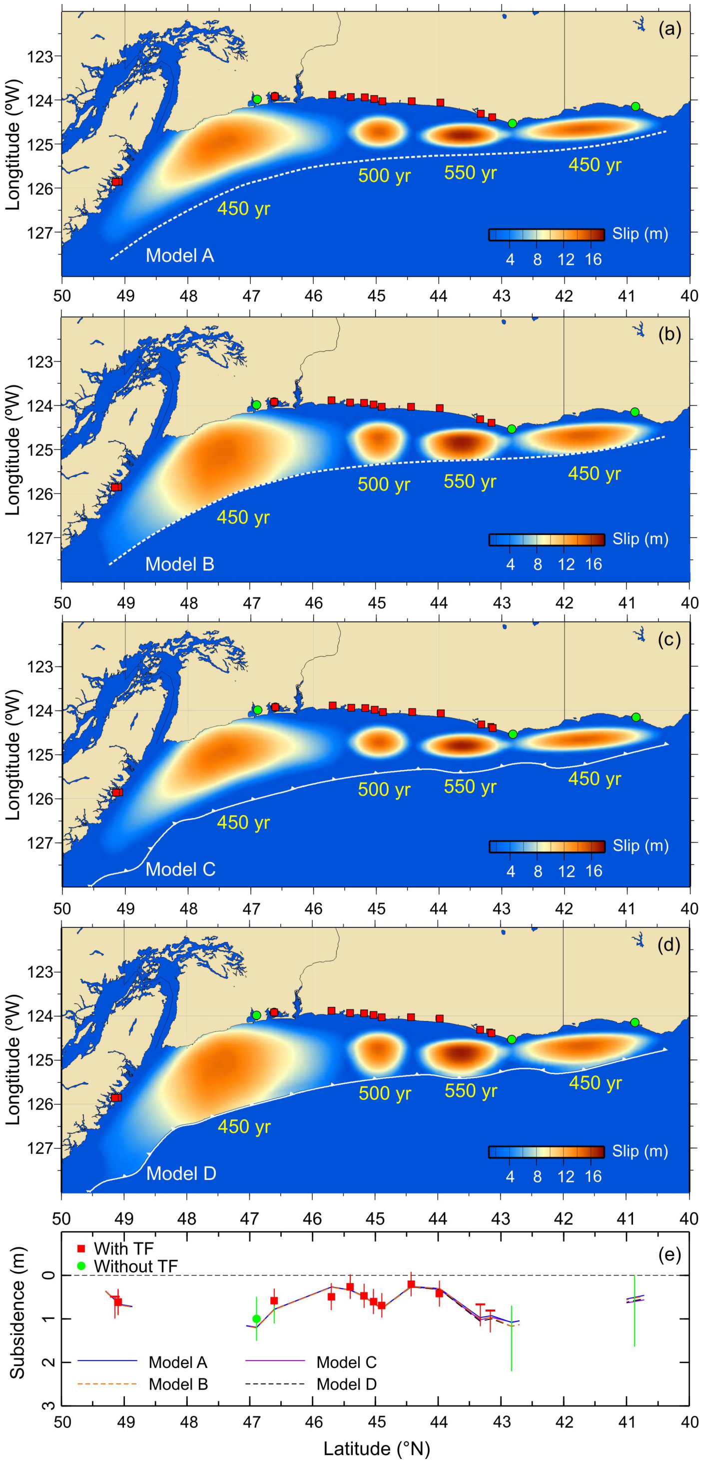

Figure 4.16. Heterogeneous slip during the 1700 giant earthquake. (a) The preferred rupture model and (b) a trench-breaching rupture model by *Wang et al.* [2013]. Dashed white line marks the updip limit of the rupture. (c) and (d) are the updated versions of (a) and (b) in this study, respectively. White barbed line is a more detailed version of the deformation front (updip limit). (e) Model-predicted coseismic subsidence and paleoseismic estimates [modified from *Wang et al.*, 2013].

4.4. Applications to Tsunami Hazard Assessment and Early Warning

All the coseismic deformation scenarios developed in the preceding section can be used as the initial conditions for simulation of tsunami propagation and inundation for tsunami hazard assessment and early warning. The information is useful to scientists, engineers, and city planners who wish to develop tsunami inundation and evacuation maps as well as preparedness and mitigation strategies.

4.4.1. Applications to Tsunami Hazard Assessment

For tsunami hazard assessment, all the rupture scenarios can be systematically evaluated using a logic tree with branches from most to least important in controlling tsunami generation [e.g., *Priest et al.*, 2009; *Witter et al.*, 2011]. An example of a very simple logic tree with branches defined by two parametres, i.e., slip distribution along trench-normal direction (Figures 4.6a, 4.9a, and 4.13a) and the size of the rupture, is shown in Figure 4.17. Each branch of the logic tree should be assigned a reasonable weighting factor by an expert committee based on geological and geophysical data at Cascadia and other analogous subduction systems. Total model weight at the end of each branch is the product of the weighting factors of the two parametres (Figure 4.17). The weight for each rupture scenario represents the relative confidence of the committee based on the current available geological and geophysical observations and by no means reflects the probability of the next tsunami.

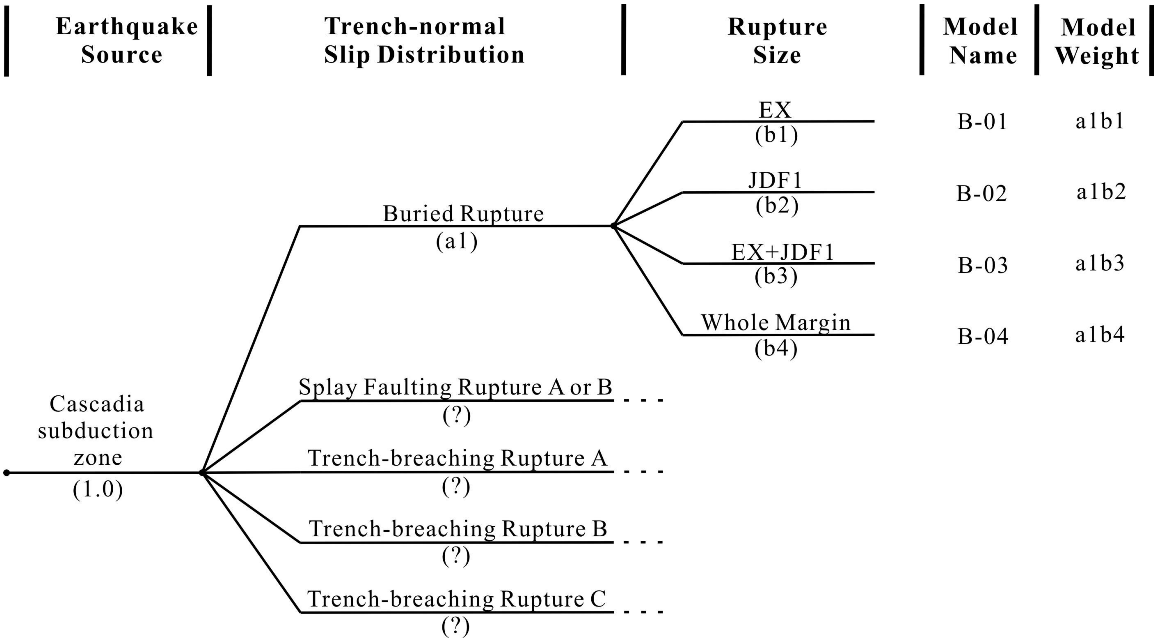

Figure 4.17. An example of a simple logic tree to rank the 21 rupture models. See Table 4.1 and Figure 4.4 for the different ruptures. Question mark in the parentheses represents the weighting factor that should be assigned by an expert committee. If a weighting factor a1 is assigned to the buried rupture and factor b1 is assigned to the rupture size (EX), the total model weight of model B-01 is the product of a1 and b1.

To briefly show how to use the tsunami sources developed in section 4.3.3 for tsunami simulation, three (B-03, S-B3, and T-B3, see Table 4.1) of them are tested for wave propagation with the FUNWAVE-TVD model [*Shi et al.*, 2012] by Dr. Tania L. Insua at Ocean Networks Canada [*Insua et al.*, 2015]. This numerical model is a long wave propagation model. FUNWAVE-TVD solves fully non-linear and dispersive Boussinesq equations [*Wei et al.*, 1995] for the wave propagation in coastal areas and has been benchmarked against other tsunami numerical simulation models as part of the U.S. National Tsunami Hazard Mitigation Program. This model combines a tsunami source model (coseismic seafloor deformation) with a digital elevation models (DEM) of the area to provide information about the estimated time of arrival of the wave and wave height for different sites. The digital elevation grids used for this study were based on the ETOPO 1 global topography and bathymetry [*Amante and Eakins*, 2009] as well as the British Columbia NOAA DEM [*Carignan et al.*, 2013] and two new DEM for Barkley Sound [*Love et al.*, 2015a] and Port Alberni [*Love et al.*, 2015b]. These new DEM have been produced by NOAA-NCEI in collaboration with Ocean Networks Canada and Emergency Management BC based on data from the Canadian Hydrographic Service, GeoBC and the Alberni-Clayoquot Regional District (ACRD). If topographic information, the phase speeds and particle kinematics are available, inundation maps can also be generated by the FUNWAVE-TVD model (preliminary results are available on the Ocean Networks Canada website).

Figures 4.18, 4.19, and 4.20 show the preliminary tsunami wave propagation simulations resulted from the buried rupture B-03 (Figure 4.5c), splay faulting rupture S-B3 (Figure 4.8c), and trench-breaching rupture T-B3 (Figure 4.11c), respectively. As the coseismic seafloor deformation is projected to the free sea water surface to act as initial conditions for tsunami wave propagation, we see two peak waves with the positive one westward and negative one eastward (see Figures 4.18a, 4.19a, and 4.20a) right after the earthquake (time = 0 h, 1 min). Within a few minutes, the positive one splits into two waves heading to seaward and landward directions respectively (Figures 4.18b, 4.19b, and 4.20b). In less than half an hour after the earthquake, the landward positive wave front reaches some coastal areas, e.g., the northern west coast of Vancouver Island

(Figures 4.18c, 4.19c, and 4.20c). The wave front will become irregular when approaching the coast because of wave refraction and convergence due to the geometry variation along the shelf and coast [e.g., *Cherniawsky et al.*, 2007]. In the meantime, the seaward positive wave front rapidly approaches the western boundary of the model. The maximum sea water surface elevations during the first 6 hours after the three different earthquakes are shown in Figures 4.18d, 4.19d, and 4.20d, respectively. Among the three rupture scenarios, the splay fault rupture S-B3 leads to the most devastating tsunami along the coast (Figure 4.19d).

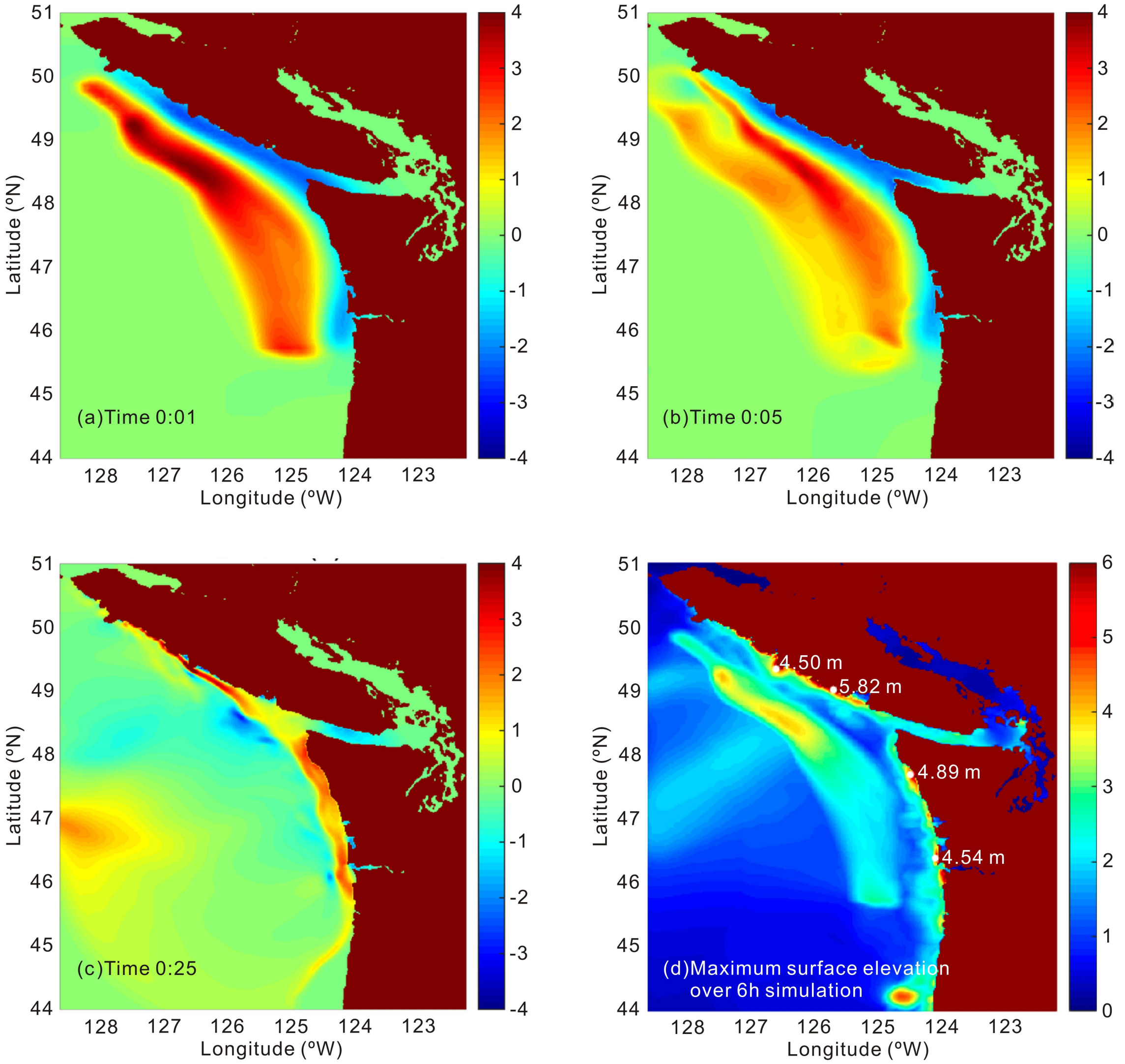

Figure 4.18. Tsunami wave propagation due to the buried rupture B-03 (see Table 4.1 and Figure 4.5c). (a), (b), and (c) are three snapshots showing the modelled tsunami wave propagation at 0:01, 0:05, and 0:25 (hour: minute) after the earthquake, respectively. (d) Maximum surface elevation during the first 6 hours after the event (B-03). Reference: Canadian Geodetic Vertical Datum of 2013 (CGVD2013).

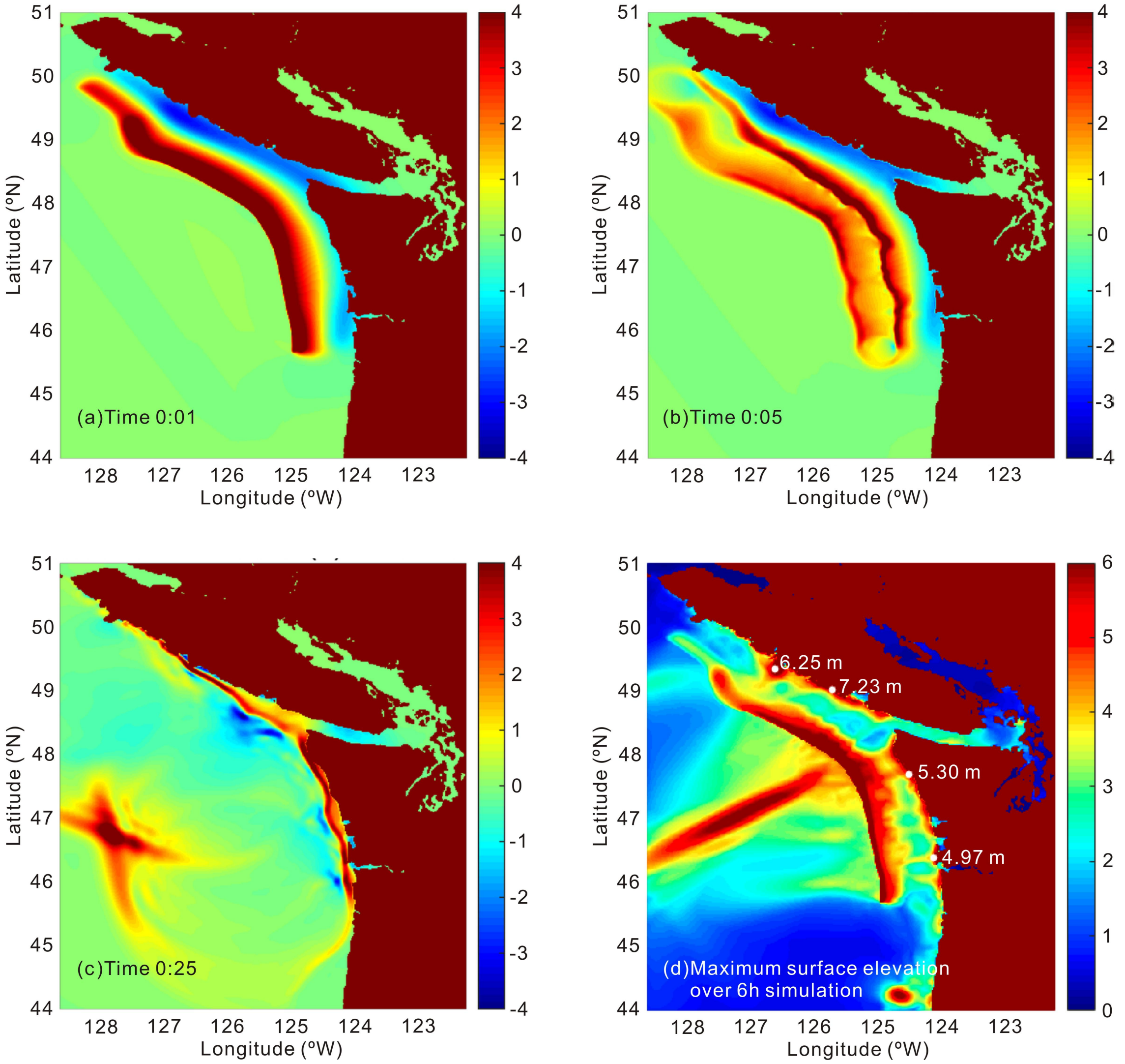

Figure 4.19. Tsunami wave propagation due to the splay faulting rupture S-B3 (see Table 4.1 and Figure 4.8c). (a), (b), and (c) are three snapshots showing the modelled tsunami wave propagation at 0:01, 0:05, and 0:25 (hour: minute) after the earthquake, respectively. (d) Maximum surface elevation during the first 6 hours after the event (S-B3). Reference: Canadian Geodetic Vertical Datum of 2013 (CGVD2013).

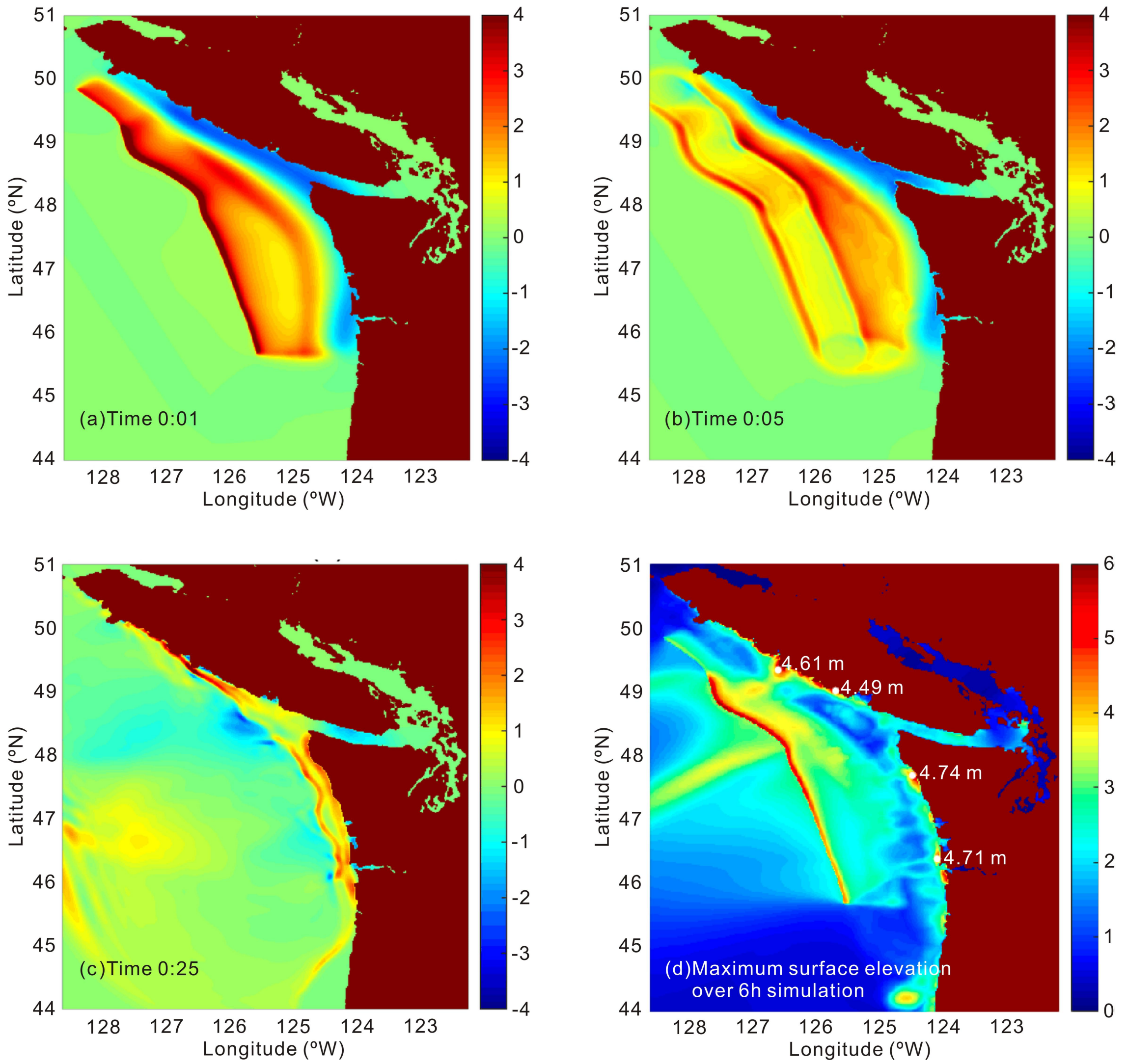

Figure 4.20. Tsunami wave propagation due to the trench-breaching rupture T-B3 (see Table 4.1 and Figure 4.11c). (a), (b), and (c) are three snapshots showing the modelled tsunami wave propagation at 0:01, 0:05, and 0:25 (hour: minute) after the earthquake, respectively. (d) Maximum surface elevation during the first 6 hours after the event Canadian Geodetic Vertical Datum of 2013 (CGVD2013).

4.4.2. Applications to Tsunami Early Warning

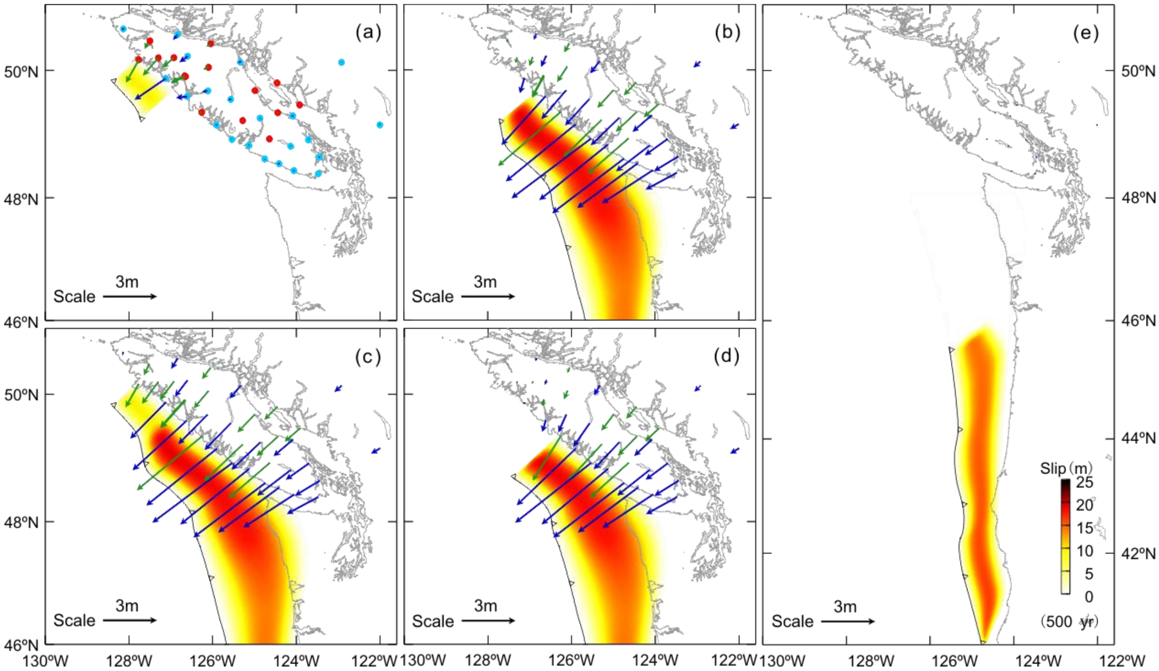

Figure 4.21. Cascadia megathrust rupture scenarios with predicted displacements of existing (dark blue arrows) and proposed (green arrows) GNSS sites. Blue and red dots in (a) indicate the locations of existing and proposed GNSS stations, respectively. The distribution of slip is of a bell shape in the dip direction (section 4.1.2), with the peak value representing 500 year of slip deficit. (a), (b), and (c) are buried rupture models B-01, B-02, and B-03 (Figure 4.5), respectively. (d) and (e) are two new buried rupture models. Rupture in (d) has the same southern boundary (Boundary 2, Figure 4.4) as models B-02 and B-03 but different northern boundary. (e) shows a rupture in southern Cascadia. The northern boundaries in (d) and (e) are for testing purpose only.

The use of real-time Global Navigational Satellite System (GNSS) displacement data for tsunami early warning in northern Cascadia was first proposed by *Dragert et al.* [2005]. The locations of existing GNSS stations on Vancouver Island and mainland Canada are shown in Figure 4.21a (blue dots). Geological Survey of Canada has proposed several new GNSS stations which are also shown in Figure 4.21a (red dots) [*Y.*

Lu and L. Nykolaishen, personal communication, 2016]. With adequate real-time GNSS observations, the displacements of GNSS stations can be inverted to determine the earthquake source to provide the initial conditions for tsunami modelling. The other way is to compare the observed GNSS displacements with the pre-computed displacement predictions of earthquake rupture models to quickly select the most appropriate pre-computed tsunami source model and corresponding inundation predictions. To confirm the feasibility of using real-time GNSS displacement data for tsunami early warning in northern Cascadia, I conduct a series of tests in this subsection (Figures 4.21, 4.22, 4.23, and 4.24).

Figure 4.21 shows the predicted horizontal coseismic displacements of existing (dark blue arrows) and proposed (green arrows) GNSS sites in northern Cascadia resulted from different buried rupture scenarios with slip distribution following a bell shape in the dip direction (section 4.1.2). For every margin-normal profile, the peak of the bell-shaped slip distribution is equivalent to 500 years of slip deficit. Three of the buried rupture models (Figures 4.21a, 4.21b, and 4.21c) are exactly the same models developed in section 4.3.1 (Figure 4.5). Two new buried rupture models (Figures 4.21d and 4.21e) are developed here. The first one (Figure 4.21d) uses the same southern boundary (boundary 2, Figure 4.4) as models B-02 (Figures 4.5b and 4.21b) and B-03 (Figures 4.5c and 4.21c) do, but the new model employs a different northern boundary for testing purpose only. The second one is shown in Figure 4.21e featuring a rupture in southern Cascadia. It is obvious that the predicted displacements of land-based GNSS stations are very sensitive to the along-strike rupture boundary close to the Vancouver Island (Figures 4.21a, 4.21b, 4.21c, and 4.21d) and insensitive to rupture farther south (Figure 4.21e).

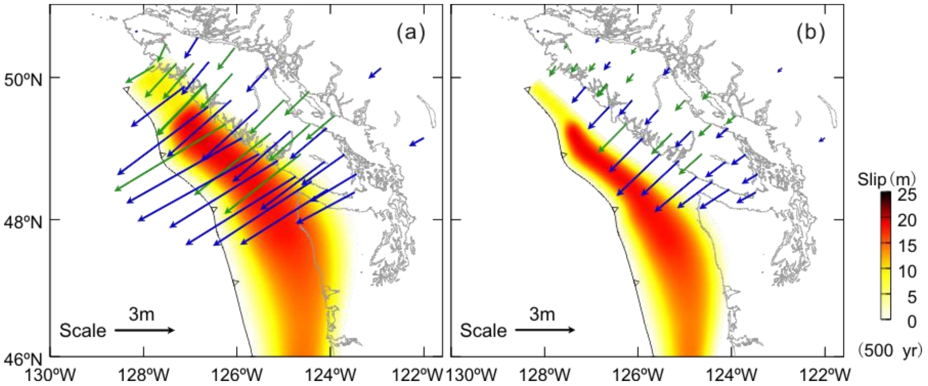

Figure 4.22. Cascadia megathrust rupture scenarios with predicted displacements of existing (dark blue arrows) and proposed (green arrows) GNSS sites. Compared with the buried rupture model B-03 (Figure 4.21c), model in (a) has a wider, and model in (b) has a narrower rupture zone in the downdip direction, respectively.

To further test whether the GNSS stations are sensitive to the downdip rupture limit, I devise two more buried rupture scenarios with a wider (Figure 4.22a) and a narrower (Figure 4.22b) rupture zone than that of model B-03 (Figure 4.21c) in the downdip direction, respectively. Other parametres are the same as used for model B-03. Clearly the predicted displacements of GNSS sites are very sensitive to the downdip limit of the coseismic rupture.

However, the land-based GNSS stations do not have very good resolution in distinguishing between different cosesimic fault behaviours in the shallow part of the megathrust which is quite far from the coast at northern Cascadia. Figures 4.21c, 4.23a, 4.23b, and 4.23c show a similar deformation pattern caused by the buried rupture B-03 (Figure 4.5c), two splay faulting ruptures S-A3 and S-B3 (Figures 4.7c and 4.8c), and a newly developed trench-breaching rupture (Figure 4.23c). In the new trench-breaching rupture model, I assume the fault slip at trench is 30% of the peak slip. Other parametres are the same as for models T-A3, T-B3, and T-C3 (section 4.3.3). These four models (Figures 4.21c, 4.23a, 4.23b, and 4.23c) have the same fault slip in the deeper part of the fault. Although they have different slip in the shallow part (Figure 4.2), they have similar GNSS displacement patterns. Especially, the difference between the new trench-breaching rupture (Figure 4.23c) and the buried rupture B-03 (Figure 4.21c) is very small, as illustrated by their differential displacements (displacements resulted from the new trench-breaching rupture minus those resulted from the buried rupture) in Figure 4.23d. Most of the GNSS stations feature differential displacements of less than 5 cm except a few sites on northern Vancouver Island. With the current real-time GNSS resolution (5cm) [*Y. Jiang*, personal communication, 2016], it would be very difficult to distinguish between these two rupture scenarios. The examples here indicate that it is very difficult for the land-based GNSS stations to timely differentiate between different behaviours of the shallow portion of the megathrust for tsunami early warning.

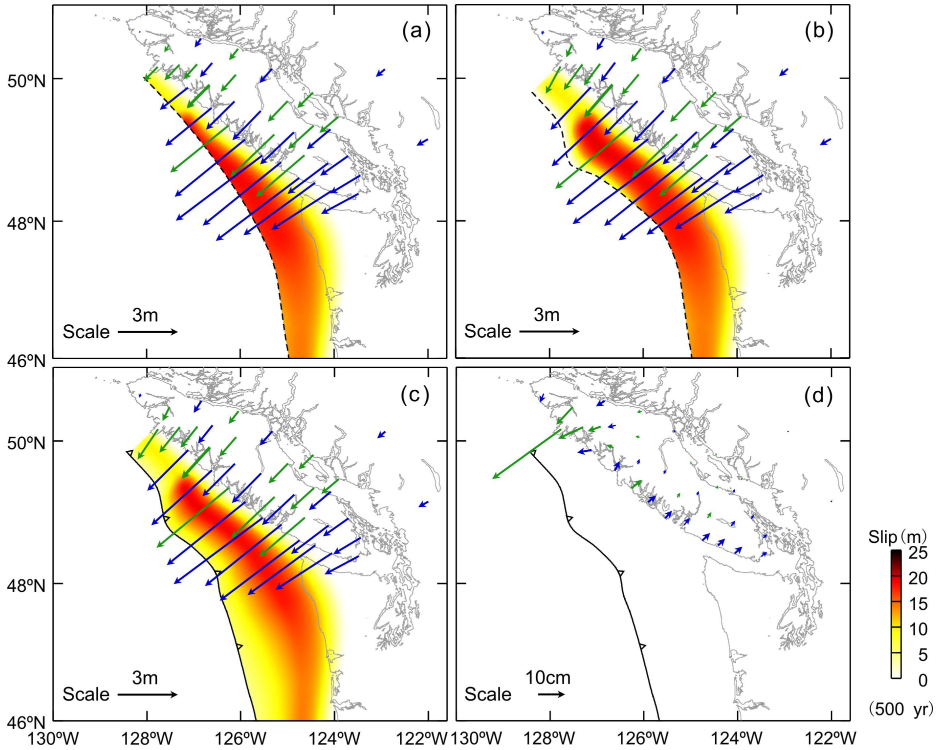

Figure 4.23. Cascadia megathrust rupture scenarios with predicted displacements of existing (dark blue arrows) and proposed (green arrows) GNSS sites. (a), (b), and (c) are splay faulting rupture model S-A3 (Figure 4.7c), splay faulting rupture model S-B3 (Figure 4.8c), and a new trench-breaching model (see the text), respectively. (d) Differential GNSS displacements between the trench-breaching model (Figure 4.23c) and the buried rupture model B-03 (Figure 4.21c).

One important objective of the GNSS Tsunami Early Warning System is to prevent false alarm in the situation of a large but non-tsunamigenic earthquake. To illustrate whether the GNSS stations can differentiate between tsunamigenic megathrust earthquake and non-tsunamigenic strike-slip earthquake, I show a simple strike-slip rupture in the Nootka fault zone in Figure 4.24. Typically, earthquakes occur along the Nootka fault zone over a depth range of 10–15 km and with M_w less than 7.0 [*Obana et* *al.*, 2015]. In this simple test, I construct a vertical rectangular fault with length 40 km and width 15 km. The shallowest part of the fault is assumed zero depth. For simplicity, I assign an uniform slip to the rectangular fault. The direction of fault slip is the relative plate motion between the Explorer plate and Juan de Fuca plate. The relative motion between these two plates is about 2 cm/year (section 2.2). If the slip magnitude is assumed equivalent to 100 yr of slip deficit, the slip magnitude would be 2 metres. The modelled earthquake M_w is about 7.0. The resultant horizontal coseismic displacements of land-based GNSS stations are extremely small as shown in Figure 4.24, with directions distinctly different from those due to a megathrust event.

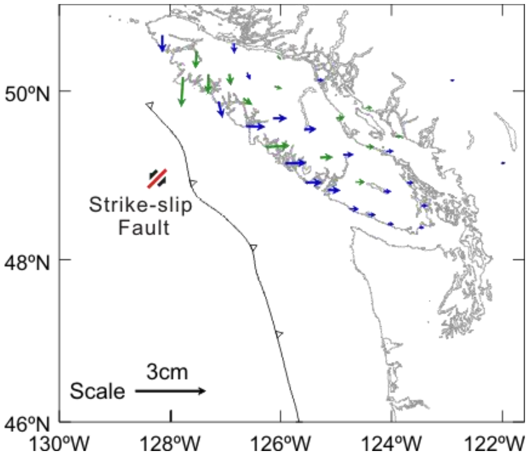

Figure 4.24. An example of a strike-slip rupture in Nootka fault zone with predicted displacements of existing (dark blue arrows) and proposed (green arrows) GNSS sites.

As is obvious from the tests, there are two main issues for using real-time GNSS displacement data to determine the coseismic rupture. (1) The existing GNSS stations (blue dots in Figure 4.21a) at northern Cascadia are inadequate to constrain the along-strike rupture boundary which is important in controlling tsunami impact on the coastal area of Vancouver Island. With the proposed GNSS stations (red dots in Figure 4.21a), especially the sites proposed in northern Vancouver Island, real-time GNSS displacement data can well determine the the along-strike rupture boundary offshore of Vancouver Island. (2) Because the land-based GNSS stations are far from the most seaward part of the megathrust, they cannot well constrain the rupture characteristics farther offshore. For tsunami generation, the coseismic fault behaviour of the shallow part of the megathrust is of first-order importance. Although the coastal deformation induced by a buried rupture (Figure 4.21c) might be similar to that induced by a splay faulting rupture (Figures 4.23a and 4.23b) or a trench-breaching rupture (Figure 4.23c), the resultant tsunamis may differ significantly. Thus near-trench (seafloor) real-time observations are needed to complement the land-based network. Ocean Networks Canada currently has real-time seismic and pressure data in all the nodes of the NEPTUNE cabled ocean observatory off the west coast (Figure 4.25). An extension of the infrastructure available for seismic detection in the Ocean Networks Canada observatories will take place in the upcoming years and is expected to be operational by 2019 [*T. L. Insua*, personal communication, 2016]. It will be extremely valuable to expand this system with extension cables to accomplish a much wider coverage of the near-trench area. Given adequate GNSS sites and a proper network configuration, a combination of near-trench real-time observations and the GNSS displacements certainly can distinguish between the different rupture scenarios as tsunami sources. Insights form this section can be applied to other subduction zones for tsunami early warning.

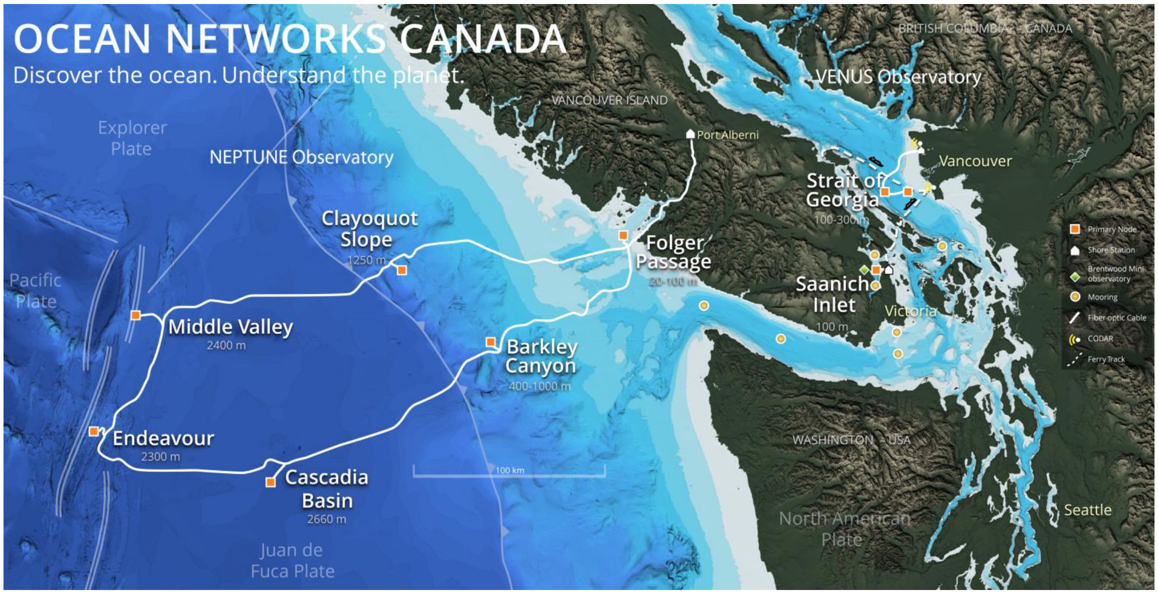

Figure 4.25. The NEPTUNE cabled ocean observatory [from *T. L. Insua*, personal communication, 2016]. Red squires represent primary nodes of the observatory. Real-time seismic and pressure data in all the nodes of the observatory are currently available. White barbed line indicates the deformation front.

Chapter 5. Conclusions and Recommendations for Future Research

In this M.Sc. dissertation, I fulfill the three main objectives discussed in Introduction (Chapter 1). For the Explorer segment, I developed 2D finite-element thermal models to investigate the thermal state of the megathrust (Chapter 2). With some ambiguity that does not affect the definition of the shallow potential rupture zone, I use low frequency earthquake (LFE) hypocentres around 35 km depth determined by *Royer and Bostock* [2014] to help constrain the interface geometry for the Explorer segment. By assuming that the downdip limit of the potential rupture zone is controlled by a temperature of 450°C and the updip limit is at the deformation front, I defined the potential megathrust rupture zone for the Explorer segment. For the Winona segment where the tectonic structure and processes are presently not very well understood, I provided a preliminary estimate of the décollement temperatures by considering only the effect of sedimentation on a cooling lithosphere (Appendix). Motivated by the 2011 M_w Tohoku-Oki earthquake which features a trench-breaching megathrust rupture, I reanalyzed the marine multichannel seismic images of the accretionary wedge deformation front at northern Cascadia to identify potential tsunamigenic faults and search for evidence for previous trench-breaching ruptures (Chapter 3). To investigate how the different faults seen on the seismic images can contribute to tsunami generation, I devised hypothetical models of a frontal thrust and a back-thrust (Chapter 3). I also extended the splay fault proposed for central Cascadia [*Priest et al.*, 2009] northward with two versions. In order to simulate whole-margin rupture scenarios for tsunami hazard assessment and early warning, I compiled a new Cascadia megathrust geometry and updated the potential rupture zone for Cascadia (Chapter 4). For tsunami hazard assessment and early warning at northernmost Cascadia, a suite of 21 tsunami source scenarios have been developed using the 3D dislocation model based on the latest understanding of fault structures, theoretical knowledge of fault mechanics, and lessons learned from recent large tsunamigenic earthquakes around the world (Chapter 4). The main findings of this dissertation research are summarized as follows:

(1) The 2D finite-element thermal models for the Explorer segment of the Cascadia megathrust show that the thermal condition allows a narrow potential rupture zone of ~60 km downdip width that is located offshore but extends to within 10 km of the coast (Chapter 2). This conclusion is insensitive to ambiguities in the interface geometry. The effect of megathrust frictional heating on the thermal limit of the potential rupture zone is very small because of the low rate of subduction and shallow depth of the affected fault segment. If most of the sediment on the incoming plate was accumulated over the most recent 1 Ma instead of the 4 Ma as assumed in the preferred model, the thermally defined potential rupture zone will extend farther landward by ~15 km. If the rupture is confined to be south of the Winona Basin, the strike length of the potential rupture zone is less than 100 km. Hazard estimates based on this strike length should be regarded as a minimum, because a similar thrust rupture along the boundary of the Winona block and

North American plate cannot be excluded. The Explorer segment is a small portion of the Cascadia megathrust, but its seismic rupture, whether independently or together with the rest of the Cascadia megathrust, can generate tsunamis that affect the local coastal area.

(2) An examination of marine multichannel seismic images with a focus on the accretionary wedge deformation front (Chapter 3) has not provided strong evidence for trench-breaching ruptures during previous megathrust earthquakes at Cascadia. Given the complex structure at Cascadia's deformation front, the possibility of a trench-breaching rupture appears to be low. Buried rupture and activation of multiple thrusts and back-thrusts may be more likely in generating tsunamis. However, for tsunami hazard assessment, we should consider all the rupture scenarios, including the slip-to-trench rupture involving frontal thrusts.

(3) Coseismic seafloor uplift is the primary cause of tsunami. Coseismic subsidence of the coastal area further enhances tsunami wave heights and run-up. The 3D dislocation rupture models developed in Chpater 4 indicate that the buried rupture, splay faulting rupture, and trench-breaching rupture scenarios can result in significant seafloor uplift and coastal subsidence, and hence will lead to great tsunamis that seriously affect the local coastal area. The back-thrust rupture near the accretionary wedge deformation front is unimportant for tsunami generation. The rupture models developed in this study did not consider along-strike fault slip variation. More realistic rupture scenarios should be developed in the future.

(4) Deformation modelling using the various rupture scenarios indicates that land-based real-time Global Navigational Satellite System (GNSS) measurements can well constrain along-strike rupture boundaries and distinguish between tsunamigenic megathrust earthquake and non-tsunamigenic strike-slip earthquake (Chapter 4). However, the same modelling also indicates that these measurements cannot determine the coseismic fault behaviour of the shallow portion of the megathrust which is farther offshore but is of first-order importance in tsunami generation (Chapter 4). A combination of near-trench real-time observations (if available in the future) and the real-time GNSS displacement data with adequate sites and proper network configuration can be applied to tsunami early warning. The combination can effectively differentiate between different rupture scenarios as tsunami sources and can also prevent false alarms due to non-tsunamigenic strike-slip earthquakes along the Nootka fault zone.

Future efforts can be made to continue this study in the following directions:

(1) Better and more observational constraints will improve the definition of the thermal state of the megathrust at northernmost Cascadia. For the Explorer segment, more detailed constraints on the sedimentation history will help better define the seaward boundary condition for the 2D finite-element thermal modelling. More active and passive seismic observations will minimize the ambiguity in defining the plate interface geometry. Offshore heat flow data are needed to better constrain the shallow thermal state of the megathrust.

(2) For the Winona segment, the tectonic structure and process need to be further studied to better resolve the seismogenesis and tsunamigenesis issues. The preliminary 1D thermal modelling in Appendix indicates that the décollement (assumed to lie at the top of the oceanic crust) is cold enough to allow megathrust earthquakes across the full width of the Winona Basin and to the coast. The largest uncertainties in the estimate of the thermal structure arise from the poorly constrained age of the oceanic lithosphere beneath the basin, although the few existing seafloor heat flow observations provide some help. The greatest uncertainties in translating the thermal structure into risks associated with seismogenesis and tsunamigenesis arise from the poor definition of current convergence rates along the Winona block/North America plate boundary. By considering only the sedimentation effect (ignoring the subduction effect), I have obtained a minimum estimate of the downdip of the potential rupture zone for the Winona fragment. Adding the subduction effect would only make the megathrust colder and thus widen the downdip extent of the thermally allowed potential rupture zone. According to the model results (Appendix), a width of the potential rupture zone should be at least ~35 km reaching the continental slope and extending to a depth of ~7 km below the seafloor. The strike length of the potential rupture zone should be around 150 km if the rupture is confined in the Winona Basin. The results indicate that the Winona fragment should be included in future seismic and tsunami hazard assessment.

(3) Better knowledge of previous great subduction zone earthquakes will lead to more realistic rupture scenarios for tsunami hazard assessment and real-time early

warning. Observations from large megathrust earthquakes world-wide, e.g., A.D. 1700 Cascadia [*Wang et al.*, 2013], 2004 Sumatra [*Chlieh et al.*, 2007], 2010 Chile [*Lorito et al.*, 2011] and 2011 Tohoku-Oki [e.g., *Ide et al.*, 2011] , suggest (along-strike) heterogeneous coseismic slip distribution. With better paleoseismic constraints, we can devise more realistic rupture models by considering along-strike slip variations which has not been included in the study. Besides, how the different faults, such as frontal thrust, back-thrust, and splay fault, have contributed to the previous megathrust earthquakes and associated tsunamis can also be better understood through more detailed and systematic paleoseismic studies.

(4) For tsunami hazard assessment at northernmost Cascadia, more efforts are needed to systematically evaluate and improve the different rupture scenarios developed in Chapter 4. An example of using a simple logic tree with only two branches defined by trench-normal slip distribution and rupture size is given in section 4.4.1. There may be other ways to design a logic tree. The purpose of evaluating different rupture scenarios is to assign reasonable weighting factors to various branches of the logic tree. The weighting factors should be assigned by an expert panel based on the current geological and geophysical observations at Cascadia and comparison with other subduction zones.

(5) For tsunami early warning at northermost Cascadia, a combination of near-trench real-time observations and the (proposed and existing) GNSS displacements can distinguish between different rupture scenarios as tsunami sources and exclude non-tsunamigenic strike-slip ruptures. It would be extremely helpful to add real-time

sensors such as pressure gauges and tiltmetres extending from the nodes of the NEPTUNE cabled ocean observatory to have a wide coverage of the near-trench area. It also would be extremely helpful to set up adequate real-time GNSS stations with proper network configuration. How to combine the different real-time data sets for tsunami early warning needs to be further studied.

Bibliography

Amante, C., and Eakins, B. W. (2009). ETOPO1 1 arc-minute global relief model: procedures, data sources and analysis. *NOAA Technical Memorandum NESDIS NGDC-24*.

Atwater, B. F., Nelson, A. R., Clague, J. J., Carver, G. A., Yamaguchi, D. K., Bobrowsky, P. T., Bourgeois, J., Darienzo, M. E., Grant, W. C., Hemphill-Haley, E., Kelsey, H. M., Jacoby, G. C., Nishenko, S. P., Palmer, S. P., Peterson, C. D., and Reinhart, M. A. (1995). Summary of coastal geologic evidence for past great earthquakes at the Cascadia subduction zone. *Earthquake spectra*, *11*(1), 1-18.

Audet, P., Bostock, M. G., Boyarko, D. C., Brudzinski, M. R., and Allen, R. M. (2010). Slab morphology in the Cascadia fore arc and its relation to episodic tremor and slip. *Journal of Geophysical Research: Solid Earth*, *115*, B00A16.

Audet, P., Bostock, M. G., Mercier, J. P., and Cassidy, J. F. (2008). Morphology of the Explorer–Juan de Fuca slab edge in northern Cascadia: Imaging plate capture at a ridge-trench-transform triple junction. *Geology*,*36*(11), 895-898.

Cassidy, J. F., Ellis, R. M., Karavas, C., and Rogers, G. C. (1998). The northern limit of the subducted Juan de Fuca plate system. *Journal of Geophysical Research: Solid Earth*, *103*(B11), 26949-26961.

Carignan, K.S., Eakins, B.W., Love, M.R., Sutherland, M.G., and McLean, S.J. (2013). Bathymetric Digital Elevation Model of British Columbia, Canada: Procedures, Data Sources, and Analysis. *Prepared for NOAA, Pacific Marine Environmental Laboratory (PMEL) by the NOAA National Geophysical Data centre (NGDC)*.

Cherniawsky, J. Y., Titov, V. V., Wang, K., and Li, J. Y. (2007). Numerical simulations of tsunami waves and currents for southern Vancouver Island from a Cascadia megathrust earthquake. *Pure and Applied Geophysics*,*164*(2-3), 465-492.

Chlieh, M., Avouac, J. P., Hjorleifsdottir, V., Song, T. R. A., Ji, C., Sieh, K., Sladen, A., Herbert, H., Prawirodirdjo, L., Bock, Y., and Galetzka, J. (2007). Coseismic slip and afterslip of the great M_w 9.15 Sumatra–Andaman earthquake of 2004. *Bulletin of the Seismological Society of America*, *97*(1A), S152-S173.

Clowes, R. M., Yorath, C. J., and Hyndman, R. D. (1987). Reflection mapping across the convergent margin of western Canada. *Geophysical Journal International*, *89*(1), 79-84.

Cummins, P. R., and Kaneda, Y. (2000). Possible splay fault slip during the 1946 Nankai earthquake. *Geophysical Research Letters*, *27*(17), 2725-2728.

Currie, C. A., Wang, K., Hyndman, R. D., and He, J. (2004). The thermal effects of steady-state slab-driven mantle flow above a subducting plate: the Cascadia subduction zone and backarc. *Earth and Planetary Science Letters*, *223*(1), 35-48.

Davis, E. E., and Hyndman, R. D. (1989). Accretion and recent deformation of sediments along the northern Cascadia subduction zone. *Geological Society of America Bulletin*, *101*(11), 1465-1480.

Davis, E. E., and Riddihough, R. P. (1982). The Winona Basin: structure and tectonics. *Canadian Journal of Earth Sciences*, *19*(4), 767-788.

Davis, E. E., and Seemann, D. A. (1981). *A compilation of seismic reflection profiles across the continental margin of western Canada*. Geological Survey of Canada, Pacific Geoscience Centre.

Davis, E. E., Currie, R. G., and Sawyer, B. S. (1987). Marine geophysical maps of western Canada: Geological Survey of Canada Maps 2-1987-17-1987.

DeMets, C., Gordon, R. G., Argus, D. F., and Stein, S. (1994). Effect of recent revisions to the geomagnetic reversal time scale on estimates of current plate motions. *Geophysical Research Letters*, *21*(20), 2191-2194.

Di Toro, G., Han, R., Hirose, T., De Paola, N., Nielsen, S., Mizoguchi, K., Ferri1, F., Cocco, M., and Shimamoto, T. (2011). Fault lubrication during earthquakes. *Nature*, *471*(7339), 494-498.

Dragert, H., Schmidt, M., Wang, K., and Bock, Y. (2005). A Canadian pilot project for a GPS-augmented tsunami warning system. In *AGU Fall Meeting Abstracts*.

Flück, P., Hyndman, R. D., and Wang, K. (1997). Three ‐ dimensional dislocation model for great earthquakes of the Cascadia subduction zone. *Journal of Geophysical Research: Solid Earth*, *102*(B9), 20539-20550.

Fujiwara, T., Kodaira, S., Kaiho, Y., Takahashi, N., and Kaneda, Y. (2011). The 2011 Tohoku-Oki earthquake: Displacement reaching the trench axis.*Science*, *334*(6060), 1240-1240.

Gao, D., Wang, K., Davis, E. E.,and He J. H. (2016). Thermal state of the Explorer segment of the Cascadia subduction zone: Implications for seismic and tsunami hazard (In preparation).

Gao, X., and Wang, K. (2014). Strength of stick-slip and creeping subduction megathrusts from heat flow observations. *Science*, *345*(6200), 1038-1041.

Goldfinger, C., Nelson, C. H., Morey, A. E., Johnson, J. E., Patton, J. R., Karabanov, E., Gutierrez-Pastor, J., Eriksson, A.T., Gracia, E., Dunhill, G., and Enkin, R. J. (2012). Turbidite event history: Methods and implications for Holocene paleoseismicity of the Cascadia subduction zon*e. U.S. Geological Survey Professional Paper, 1661-F.*

Gulick, S. P., Austin Jr, J. A., McNeill, L. C., Bangs, N. L., Martin, K. M., Henstock, T. J., Bull, J. M., Dean, S., Djajadihardja, Y. S., and Permana, H. (2011). Updip rupture of the 2004 Sumatra earthquake extended by thick indurated sediments. *Nature Geoscience*, *4*(7), 453-456.

Hanks, T. C. And Kanamori H. (1979), A moment magnitude scale. *Journal of Geophysical Research*, *84*, 2348–2350.

Henstock, T. J., McNeill, L. C., and Tappin, D. R. (2006). Seafloor morphology of the Sumatran subduction zone: Surface rupture during megathrust earthquakes?. *Geology*, *34*(6), 485-488.

Hsu, Y. J., Simons, M., Avouac, J. P., Galetzka, J., Sieh, K., Chlieh, M., Natawidjaja, D., Prawirodirdjo, L., and Bock, Y. (2006). Frictional afterslip following the 2005 Nias-Simeulue earthquake, Sumatra. *Science*, *312*(5782), 1921-1926.

Hu, Y., and Wang, K. (2008). Coseismic strengthening of the shallow portion of the subduction fault and its effects on wedge taper. *Journal of Geophysical Research: Solid Earth*, *113*, B12411.

Hyndman, R. D. (2013). Downdip landward limit of Cascadia great earthquake rupture. *Journal of Geophysical Research: Solid Earth*, *118*(10), 5530-5549.

Hyndman, R. D., and Wang, K. (1993). Thermal constraints on the zone of major thrust earthquake failure: The Cascadia subduction zone. *Journal of Geophysical Research: Solid Earth*, *98*(B2), 2039-2060.

Hyndman, R. D., and Wang, K. (1995). The rupture zone of Cascadia great earthquakes from current deformation and the thermal regime. *Journal of Geophysical Research: Solid Earth*, *100*(B11), 22133-22154.

Hyndman, R. D., Spence, G. D., Yuan, T., and Davis, E. E. (1994). 10. Regional geophysics and structural framework of the Vancouver Island accretionary prism. In *Proceedings of the Ocean Drilling Program, initial reports,*146(1).

Ide, S., Baltay, A., and Beroza, G. C. (2011). Shallow dynamic overshoot and energetic deep rupture in the 2011 M_w 9.0 Tohoku-Oki earthquake. *Science*, *332*(6036), 1426-1429.

Iinuma, T., Hino, R., Kido, M., Inazu, D., Osada, Y., Ito, Y., Ohzono, M., Tsushima, H., Suzuki, S., Fujimoto, H., and Miura, S. (2012). Coseismic slip distribution of the 2011 off the Pacific Coast of Tohoku Earthquake (M9. 0) refined by means of seafloor geodetic data. *Journal of Geophysical Research: Solid Earth*, *117*, B07409.

Ikari, M. J., Marone, C., and Saffer, D. M. (2011). On the relation between fault strength and frictional stability. *Geology*, *39*(1), 83-86.

Insua, T. L., Grilli, A., Grilli, S., Shelby, M., Wang, K., Gao, D., Cherniawsky, J., Harris, J., Douglas, K., Heesemann, M., McLean, S., and Moran, K. (2015). Preliminary tsunami hazard assessment in British Columbia, Canada. In *2015 AGU Fall Meeting*.

Kao, H., Shan, S. J., Dragert, H., and Rogers, G. (2009). Northern Cascadia episodic tremor and slip: A decade of tremor observations from 1997 to 2007. *Journal of Geophysical Research: Solid Earth*, *114*, B00A12.

Karato, S. I., and Wu, P. (1993). Rheology of the upper mantle: A synthesis. *Science*, *260*(5109), 771-778.

Kim, Y., Miller, M. S., Pearce, F., and Clayton, R. W. (2012). Seismic imaging of the Cocos plate subduction zone system in central Mexico. *Geochemistry, Geophysics, Geosystems*, *13*, Q07001.

Kodaira, S., No, T., Nakamura, Y., Fujiwara, T., Kaiho, Y., Miura, S., Takahashi, N., Kaneda, Y., and Taira, A. (2012). Coseismic fault rupture at the trench axis during the 2011 Tohoku-Oki earthquake. *Nature Geoscience*, *5*(9), 646-650.

Leonard, L. J., Rogers, G. C., and Mazzotti, S. (2012). A preliminary tsunami hazard assessment of the Canadian coastline. *Geological Survey of Canada, Open File*, *7201*, 126.

Lewis, T. J., Lowe, C., and Hamilton, T. S. (1997). Continental signature of a ridge-trench-triple junction: Northern Vancouver Island. *Journal of Geophysical Research: Solid Earth*, *102*(B4), 7767-7781.

Lorito, S., Romano, F., Atzori, S., Tong, X., Avallone, A., McCloskey, J., Cocco, M., Boschi, E., and Piatanesi, A. (2011). Limited overlap between the seismic gap and coseismic slip of the great 2010 Chile earthquake. *Nature Geoscience*, *4*(3), 173-177.

Love, M.R., Carignan, K.S., Eakins, B.W., Sutherland, M.G., Beasley, L., and McLean, S.J. (2015a). Digital Elevation Model of Barkley Sound, Canada: Procedures, Data Sources, and Analysis. *Prepared for NOAA, Pacific Marine Environmental Laboratory (PMEL) by the NOAA National Geophysical Data centre (NGDC)*.

Love, M.R., Carignan, K.S., Eakins, B.W., Sutherland, M.G., Beasley, L., and McLean, S.J. (2015b). Digital Elevation Model of Port Alberni, Canada: Procedures, Data Sources, and Analysis. *Prepared for NOAA, Pacific Marine Environmental Laboratory (PMEL) by the NOAA National Geophysical Data centre (NGDC)*.

Ludwin, R. S., Dennis, R., Carver, D., McMillan, A. D., Losey, R., Clague, J., Jonientz-Trisler, C., Bowechop, J., Wray, J., and James, K. (2005). Dating the 1700 Cascadia earthquake: Great coastal earthquakes in native stories. *Seismological Research Letters*, *76*(2), 140-148.

Mazzotti, S., Dragert, H., Henton, J., Schmidt, M., Hyndman, R., James, T., Lu, Y., and Craymer, M. (2003). Current tectonics of northern Cascadia from a decade of GPS measurements. *Journal of Geophysical Research: Solid Earth*, *108*, 2554.

McCaffrey, R., King, R. W., Payne, S. J., and Lancaster, M. (2013). Active tectonics of northwestern US inferred from GPS ‐ derived surface velocities.*Journal of Geophysical Research: Solid Earth*, *118*(2), 709-723.

McCaffrey, R., Qamar, A. I., King, R. W., Wells, R., Khazaradze, G., Williams, C. A., Stevens, C. W., Vollick, J. J., and Zwick, P. C. (2007). Fault locking, block rotation and crustal deformation in the Pacific Northwest. *Geophysical Journal International*, *169*(3), 1315-1340.

McCrory, P. A., Blair, J. L., Oppenheimer, D. H., and Walter, S. R. (2004). *Depth to the Juan de Fuca slab beneath the Cascadia subduction margin: A 3-D model for sorting earthquakes*. US Department of the Interior, US Geological Survey.

McCrory, P. A., Blair, J. L., Waldhauser, F., and Oppenheimer, D. H. (2012). Juan de Fuca slab geometry and its relation to Wadati ‐ Benioff zone seismicity. *Journal of Geophysical Research: Solid Earth*, *117*, B09306.

Noda, H., and Lapusta, N. (2013). Stable creeping fault segments can become destructive as a result of dynamic weakening. *Nature*, *493*(7433), 518-521.

Obana, K., Scherwath, M., Yamamoto, Y., Kodaira, S., Wang, K., Spence, G., Riedel, M., and Kao, H. (2015). Earthquake activity in northern Cascadia subduction zone off Vancouver Island revealed by ocean ‐ bottom seismograph observations. *Bulletin of the Seismological Society of America*,*105*(1), 489-495.

Okada, Y. (1985). Surface deformation due to shear and tensile faults in a half-space. *Bulletin of the Seismological Society of America*, *75*(4), 1135-1154.

Ozawa, S., Nishimura, T., Munekane, H., Suito, H., Kobayashi, T., Tobita, M., and Imakiire, T. (2012). Preceding, coseismic, and postseismic slips of the 2011 Tohoku earthquake, Japan. *Journal of Geophysical Research: Solid Earth*, *117*, B07404.

Peacock, S. M., and Wang, K. (1999). Seismic consequences of warm versus cool subduction metamorphism: Examples from southwest and northeast Japan. *Science*, *286*(5441), 937-939.

Plafker, G. (1972). Alaskan earthquake of 1964 and Chilean earthquake of 1960: Implications for arc tectonics. *Journal of Geophysical Research*, *77*(5), 901-925.

Priest , G. R., Witter, R. C., Zhang, Y. J., Wang, K., Goldfinger, C., Stimely, L. L., English, J. T., Pickner, S. G., Hughes, K. L.B., Wille, T. E., and Smith, R. L. (2013). Tsunami inundation scenarios for Oregon. *Oregon Department of Geology and Mineral Industries, Open-file report 0-13-19.*

Priest, G. R., Goldfinger, C., Wang, K., Witter, R. C., Zhang, Y., and Baptista, A. M. (2009). Tsunami hazard assessment of the Northern Oregon coast: a multi-deterministic approach tested at Cannon Beach, Clatsop County, Oregon. *Oregon Department of Geology and Mineral Industries, Special Paper 41*.

Priest, G. R., Goldfinger, C., Wang, K., Witter, R. C., Zhang, Y., and Baptista, A. M. (2010). Confidence levels for tsunami-inundation limits in northern Oregon inferred from a 10,000-year history of great earthquakes at the Cascadia subduction zone. *Natural Hazards*, *54*(1), 27-73.

Priest, G. R., Zhang, Y., Witter, R. C., Wang, K., Goldfinger, C., and Stimely, L. (2014). Tsunami impact to Washington and northern Oregon from segment ruptures on the southern Cascadia subduction zone. *Natural Hazards*, *72*(2), 849-870.

Riddihough, R. (1984). Recent movements of the Juan de Fuca plate system. *Journal of Geophysical Research: Solid Earth*, *89*(B8), 6980-6994.

Riddihough, R. P., Currie, R. G., and Hyndman, R. D. (1980). The Dellwood Knolls and their role in triple junction tectonics off northern Vancouver Island. *Canadian Journal of Earth Sciences*, *17*(5), 577-593.

Rohr, K. M. M., and Tryon, A. J. (2010). Pacific-North America plate boundary reorganization in response to a change in relative plate motion: Offshore Canada. *Geochemistry, Geophysics, Geosystems*, *11*, Q06007.

Royer, A. A., and Bostock, M. G. (2014). A comparative study of low frequency earthquake templates in northern Cascadia. *Earth and Planetary Science Letters*, *402*, 247-256.

Satake, K., Fujii, Y., Harada, T., and Namegaya, Y. (2013). Time and space distribution of coseismic slip of the 2011 Tohoku earthquake as inferred from tsunami waveform data. *Bulletin of the Seismological Society of America*,*103*(2B), 1473-1492.

Satake, K., Wang, K., and Atwater, B. F. (2003). Fault slip and seismic moment of the 1700 Cascadia earthquake inferred from Japanese tsunami descriptions. *Journal of Geophysical Research: Solid Earth*, *108*, 2535.

Schmalzle, G. M., McCaffrey, R., and Creager, K. C. (2014). Central Cascadia subduction zone creep. *Geochemistry, Geophysics, Geosystems*, *15*(4), 1515-1532.

Shelly, D. R., Beroza, G. C., and Ide, S. (2007). Non-volcanic tremor and low-frequency earthquake swarms. *Nature*, *446*(7133), 305-307.

Shelly, D. R., Beroza, G. C., Ide, S., and Nakamula, S. (2006). Low-frequency earthquakes in Shikoku, Japan, and their relationship to episodic tremor and slip. *Nature*, *442*(7099), 188-191.

Shi, F., Kirby, J. T., Harris, J. C., Geiman, J. D., and Grilli, S. T. (2012). A high-order adaptive time-stepping TVD solver for Boussinesq modelling of breaking waves and coastal inundation. *Ocean Modelling*, *43*, 36-51.

Singh, S. C., Carton, H., Tapponnier, P., Hananto, N. D., Chauhan, A. P., Hartoyo, D., Bayly, M., Moeljopranoto, S., Bunting, T., Christie, P., Lubis, H., and Martin, J. (2008). Seismic evidence for broken oceanic crust in the 2004 Sumatra earthquake epicentral region. *Nature Geoscience*, *1*(11), 777-781.

Spence, G. D., Hyndman, R. D., Davis, E. E., and Yorath, C. J. (1991a). Seismic structure of the northern Cascadia accretionary prism: evidence from new multichannel seismic reflection data. *Continental Lithosphere: Deep Seismic Reflections*, 257-263.

Spence, G. D., Hyndman, R. D., Langton, S., Yorath, C. J., and Davis, E. E. (1991b). Multichannel seismic reflection profiles across the Vancouver Island continental shelf and slope. *Geological Survey of Canada, Open File*, 2391.

Su, X., Baumann, K., and Thiede, J. (2000). 4. Calcareous nannofossils from leg 168: biochronology and diagenesis 1. In *Proceedings of the Ocean Drilling Program, Scientific Results*, *168*, 39-49.

Sun, T., and Wang, K. (2015). Viscoelastic relaxation following subduction earthquakes and its effects on afterslip determination. *Journal of Geophysical Research: Solid Earth*, *120*(2), 1329-1344.

Van Keken, P. E., Kiefer, B., and Peacock, S. M. (2002). High-resolution models of subduction zones: Implications for mineral dehydration reactions and the transport of water into the deep mantle. *Geochemistry, Geophysics, Geosystems*, *3*(10), 1056.

Wada, I., and Wang, K. (2009). Common depth of slab-mantle decoupling: Reconciling diversity and uniformity of subduction zones. *Geochemistry, Geophysics, Geosystems*, *10*, Q10009.

Wada, I., Wang, K., He, J., and Hyndman, R. D. (2008). Weakening of the subduction interface and its effects on surface heat flow, slab dehydration, and mantle wedge serpentinization. *Journal of Geophysical Research: Solid Earth*, *113*, B04402.

Wang, K. (2007). Elastic and viscoelastic models of crustal deformation in subduction earthquake cycles. *The Seismogenic Zone of Subduction Thrust Faults*, 540-575.

Wang, K., and Davis, E. E. (1992). Thermal effects of marine sedimentation in hydrothermally active areas. *Geophysical Journal International*, *110*(1), 70-78.

Wang, K., and He, J. (2008). Effects of frictional behaviour and geometry of subduction fault on coseismic seafloor deformation. *Bulletin of the Seismological Society of America*, *98*(2), 571-579.

Wang, K., and Hu, Y. (2006). Accretionary prisms in subduction earthquake cycles: The theory of dynamic Coulomb wedge. *Journal of Geophysical Research: Solid Earth*, *111*, B06410.

Wang, K., and Tréhu, A. M. (2016). Invited review paper: Some outstanding issues in the study of great megathrust earthquakes—The Cascadia example. *Journal of Geodynamics*, *98*, 1-18.

Wang, K., He, J., Schulzeck, F., Hyndman, R. D., and Riedel, M. (2015). Thermal condition of the 27 October 2012 M_w 7.8 Haida Gwaii subduction earthquake at the obliquely convergent Queen Charlotte margin. *Bulletin of the Seismological Society of America, 105(2B)*, 1290–1300.

Wang, K., Hu, Y., and He, J. (2012). Deformation cycles of subduction earthquakes in a viscoelastic Earth. *Nature*, *484*(7394), 327-332.

Wang, K., Wells, R., Mazzotti, S., Hyndman, R. D., and Sagiya, T. (2003). A revised dislocation model of interseismic deformation of the Cascadia subduction zone. *Journal of Geophysical Research: Solid Earth*, *108*, 2026.

Wang, P. L. (2012). Rupture models of the great 1700 Cascadia earthquake based on microfossil paleoseismic observations.

Wang, P. L., Engelhart, S. E., Wang, K., Hawkes, A. D., Horton, B. P., Nelson, A. R., and Witter, R. C. (2013). Heterogeneous rupture in the great Cascadia earthquake of 1700 inferred from coastal subsidence estimates. *Journal of Geophysical Research: Solid Earth*, *118*(5), 2460-2473.

Wei, G., Kirby, J. T., Grilli, S. T., and Subramanya, R. (1995). A fully nonlinear Boussinesq model for surface waves. Part 1. Highly nonlinear unsteady waves. *Journal of Fluid Mechanics*, *294*, 71-92.

Wilson, D. S. (1993). Confidence intervals for motion and deformation of the Juan de Fuca plate. *Journal of Geophysical Research: Solid Earth*, *98*(B9), 16053-16071.

Wilson, D. S. (2002). The Juan de Fuca plate and slab: Isochron structure and Cenozoic plate motions. *The Cascadia Subduction Zone and Related Subduction Systems*, *4350*, 9-12.

Witter, R. C., Zhang, Y. J., Wang, K., Priest, G. R., Goldfinger, C., Stimely, L., English, J. T. , and Ferro, P. A. (2013). Simulated tsunami inundation for a range of Cascadia megathrust earthquake scenarios at Bandon, Oregon, USA. *Geosphere*, *9*(6), 1783-1803.

Witter, R. C., Zhang, Y., Wang, K., Goldfinger, C., Priest, G. R., and Allan, J. C. (2012). Coseismic slip on the southern Cascadia megathrust implied by tsunami deposits in an Oregon lake and earthquake ‐ triggered marine turbidites. *Journal of Geophysical Research: Solid Earth*, *117*, B10303.

Witter, R. C., Zhang, Y., Wang, K., Priest, G. R., Goldfinger, C., Stimely, L. L., English, J. T., and Ferro, P. A. (2011). Simulating tsunami inundation at Bandon, Coos County, Oregon, using hypothetical Cascadia and Alaska earthquake scenarios. *Oregon Department of Geology and Mineral Industries Special Paper 43*.

Yorath, C. J., Clowes, R. M., MacDonald, R. D., Spencer, C., Davis, E. E., Hyndman, R. D., Rohr, K., Sweeny, J. F., Currie, R. G., Halpen, J. F., Halpenny, J. F., and Seemann, D. A. (1987). Marine Multichannel Seismic Reflection, Gravity and Magnetic Profiles: Vancouver Island Continental Margin and Juan de Fuca Ridge. *Geological Survey of Canada, Open file*, 1661.

Yuan, T., Spence, G. D., and Hyndman, R. D. (1994). Seismic velocities and inferred porosities in the accretionary wedge sediments at the Cascadia margin. *Journal of Geophysical Research: Solid Earth*, *99*(B3), 4413-4427.

Appendix: Potential of Megathrust Earthquakes and Tsunamis in the Winona Basin Area

A.1. Tectonics and Sedimentation History

The megathrust and tsunamigenic potential of the Winona part of the Explorer segment of the Cascadia subduction zone has never been investigated. To address this issue, I develop one-dimensional (1D) finite element thermal models to investigate the thermal state of the probable megathrust. Again, I adopt the argument that megathrust earthquakes are limited within a temperature range, that is, rupture can initiate at temperatures less than 350°C and can propagate at temperatures less than than 450°C (section 2.1).

The Winona crustal block beneath the Winona basin lies between the Paul Revere Ridge and its northwestern extension, the Revere-Dellwood fracture zone, and the continental margin off northernmost Vancouver Island and southern Queen Charlotte sound (Figure A.1a). The block might be separated from the Explorer plate. The history of its crustal generation can only be speculated on, since magnetic anomalies appear to have been thermally erased as a consequence of deep sediment burial in the region. On the basis of plate kinematics constrained by magnetic anomalies further offshore, *Davis and Riddihough* [1982] speculate that the oceanic crust of the Winona block ranges in age from roughly 1 Ma in the southeast to 5 Ma in the northwest. The Revere-Dellwood fracture zone currently serves as a transform fault between the Pacific plate and the

Winona block and is seismically very active. Extensional faults imaged at the seafloor at the Dellwood Knolls, and active volcanism there and at the Tuzo Wilson Knolls indicate active rifting and possibly the creation of new oceanic crust in that region [e.g., *Riddihough et al.*, 1980].

The current role of the Paul Revere Ridge is not well understood. *Davis and Riddihough* [1982] have speculated that the uplift of the Paul Revere Ridge and the landward tilting of the Winona block are the result of faulting on the seaward side of the ridge. Whatever the cause, it is clear that rotation of the block about a horizontal axis paralleling the strike of the Paul Revere Ridge began about 1.5-2 Ma BP. Since then, the Winona basin has been kept filled with turbidite sediments of glacial origin. The fanning that is characteristic of the turbidite deposits (Figure A. 1b) indicates that sedimentation was synchronous with the crustal tilting and subsidence of the Winona block, although the seismic imaging is not adequate to define stratigraphic details deep in the basin. For the purposes of thermal modelling, I assume that the basin subsidence and rapid sedimentation began at 1.5-2 Ma BP, and continued steadily since. The sedimentation history of the outer (seaward) part of the basin may be slightly shorter than that of the inner (landward) part as a result of progressive onlap, but this detail cannot be resolved.

Also important to the subject of this study is the evidence in seismic reflection data for convergence between the Winona block and North America, as seen in anticlinal structures that have developed within the Winona Basin [*Davis and Seemann, 1981*; *Davis et al.*, 1987]. Many of the structures appear to include recently deposited sediments

(Figure A.1b). The seaward-most extent of these folds is inferred to mark the deformation front of an accretionary prism. In the northwestern part of the basin (represented by the profile shown in Figure A.1b), the frontal anticlinal structures are isolated from and lie well seaward of the base of the continental slope; any thrust linking them to the deeper part of the subduction thrust must leave the intervening sediments undeformed over a distance of 10-20 km.

While many aspects of the Paul Revere Ridge and the structures within the Winona Basin are unclear, it is difficult to rule out recent subduction in this area. An alternate interpretation has been presented by *Rohr and Tryon* [2010] who propose that the relative motion between the Explorer and North America plates is currently being taken up by a distribution of strike-slip faults in the Winona Basin and in the Explorer plate itself. Despite the different viewpoints about the tectonic model, the potential for megathrust earthquakes and associated tsunamis cannot be ignored in hazard evaluation. Hence, for the purposes of the modelling discussed below, I assume that the basin is underlain by a thrust décollement that reaches as far seaward as the seaward-most anticlinal features imaged in seismic reflection profiles, acoustic backscatter and bathymetry [*Davis and Seemann*, 1981; *Davis et al.*, 1987] (Figure A.1). The rate of margin-normal convergence must lie somewhere between the lower limit suggested by *Rohr and Tryon* [2010] (none) and an upper limit of roughly 2 cm/yr similar to the Explorer plate–North American Plate rate.

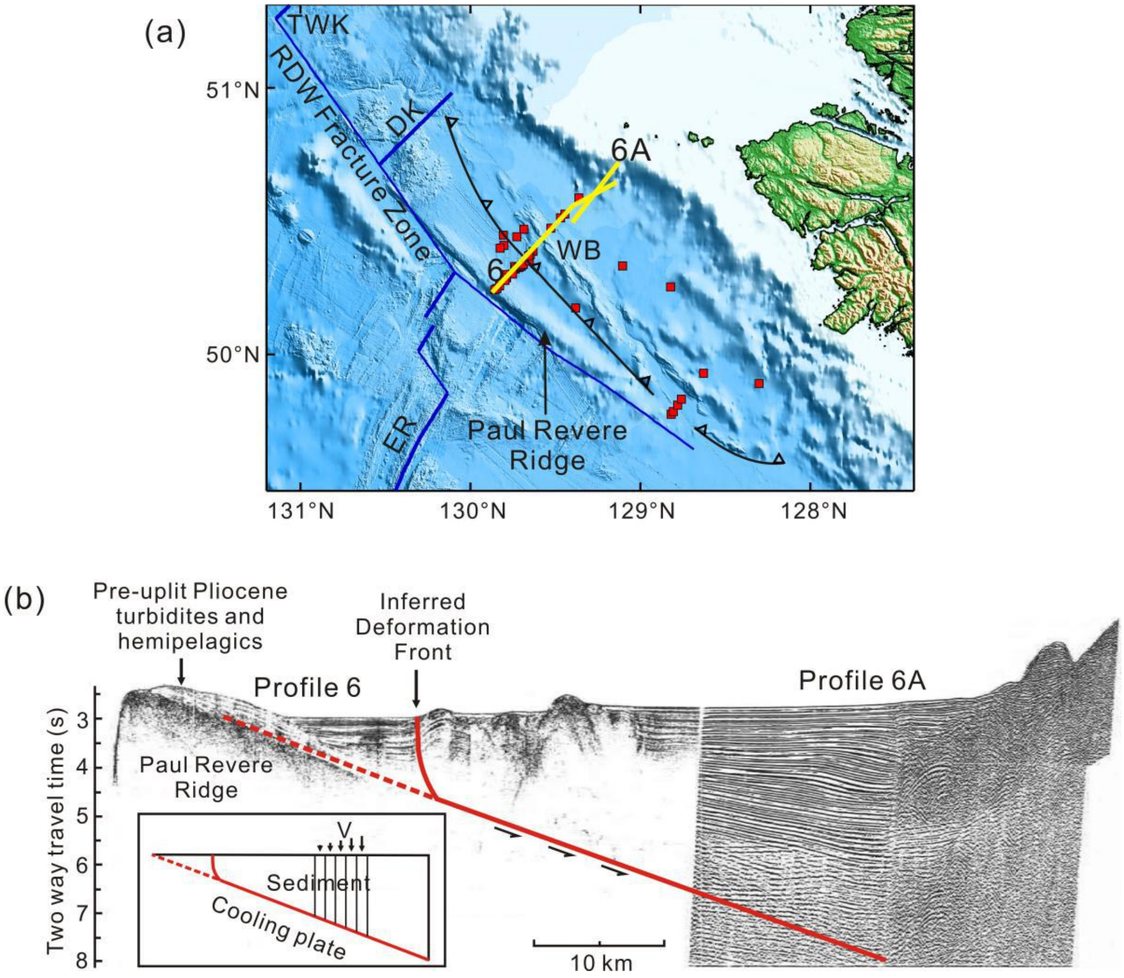

Figure A.1. Tectonic setting of the Winona region and sediment structure in the basin. (a) Regional map of Winona basin. TWK, Tuzo Wilson Knolls; DK, Dellwood Knolls; WB, Winona basin; ER, Explorer Ridge; RDW fracture zone, Revere-Dellwood-Willson fracture zone. Locations of heat flow measurements [*Davis and Riddihough*, 1982] are shown with squares. Seismic profiles 6 and 6a are shown with thick yellow lines. Black barbed line indicates the inferred deformation front. (b) Seismic reflection profile 6/6a [*Davis and Riddihough*, 1982] showing sediment structure. The vertical scale, if converted into depth, is approximately 5 times horizontal. Inset shows the simplified model.

A.2. Effects of Sedimentation

The thermal evolution of the décollement beneath the Winona Basin is affected by three factors: the total sediment accumulation, the rate of sedimentation, and the rate of subduction. Greater sediment thickness causes the décollement to be warmer and hence the potential seismogenic zone to be narrower, whereas higher rates of sedimentation and subduction have the opposite effect. Given the large uncertainties in subduction related parametres, I provide a warmest estimate of the décollement temperatures by considering the sedimentation effect only. Adding any subduction effect will make the interface cooler and the potential rupture zone wider.

In considering the sedimentation process only, if I divide the sediment section into columns (Figure A.1b), the temperature on the assumed detachment in each column is analogous to the sediment-basement interface temperature in the model of sediments deposition on a cooling plate. Therefore I can adopt the 1D heat transfer model of a cooling oceanic plate with a specified sedimentation history [*Wang and Davis*, 1992], as used to define the seaward boundary of the 2D model for the main Explorer plate (section 2.2). Here the lateral heat transfer between the columns and the gentle dip of the igneous crust (Figure 1.b) can be safely neglected.

For each sediment column, I assume a constant deposition rate during the entire Pleistocene sedimentation period compatible with the present thickness of the given column. The actual turbidite deposition history is bound to be more complex, but this is impossible to determine given presently available observations [*Davis and Riddihough*, 1982]. The material parametres I use are the same as those used by *Hyndman and Wang* [1993] (Table 2.1). Because the assumed décollement starts at the deformation front (Figure 1.b), the basement temperature further seaward is unimportant. For modelling convenience, it is appropriate to assume that sedimentation occurred during the same period everywhere, although the sedimentation period of the outer part of the basin is likely to be slightly shorter than that of the inner part for reasons discussed above. As the exact beginning time of sedimentation (1.5-2 Ma BP) and the present age of the cooling plate (4-5 Ma) are uncertain, I varied these parametres in the modelling (Figure A.2). A longer sedimentation period (2 Ma) gives basement more time to recover the effect of sediment deposition, and vice versa. A younger plate (4Ma) results in a warmer basement, and vice versa.

Surface heat flow data [see Table 1 of *Davis and Riddihough*, 1982] along the seismic reflection profile 6/6a are shown in Figure A.1a. The most remarkable feature of these data is that the values decrease landward from the outer part of the basin to the inner part. Errors of heat flow data may be up to 10-20% [*Davis and Riddihough,* 1982]. A conservative error of 20% is assigned to all the heat flow values shown in Figure A.2a.

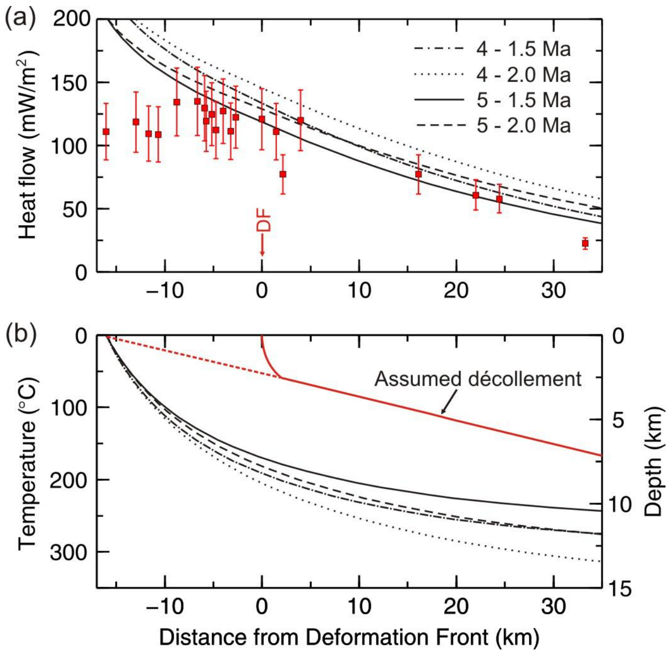

Figure A.2. Thermal model results. (a) Observed (squares with error bars) and model predicted (lines) surface heat flows. DF, deformation front. (b) Model predicted temperatures of the assumed décollement. For both (a) and (b), different models are labeled using age of incoming plate – assume of the beginning time of the sedimentation (both in Ma).

A.3. Modelling Results

I have developed 1D finite-element thermal models to investigate the thermal regime of the Winona décollement along the seismic reflection profile 6/6a (Figure A.1b). The modelling results are shown in Figure A.2, together with the seafloor heat flow data of *Davis and Riddihough* [1982]. Seaward of the deformation front, all four models predict heat flow much higher than observed. In this area, it is likely, that the seafloor heat flow is biased; outcropping basement at the nearby Paul Revere fault (Figure A.1) is very likely to facilitate ventilated hydrothermal circulation, resulting in anomalously low average heat flow [*Davis and Riddihough*, 1982]. The degree and lateral extent of this physical bias is impossible to estimate, but since our domain of interest, i.e., basement temperature landward of the deformation front, is well away from outcropping igneous basement, effects of hydrothermal heat loss are probably small. Landward of the deformation front, the observed heat flows suggest a greater trend of landward decrease than model predictions. This can be qualitatively explained by the missing subduction effect which I am unable to address quantitatively. Ignoring the misfit to the overall heat flow trend, the model with cooling plate age 5 Ma and sedimentation history 1.5 Ma (Figure A.2a) is the most compatible with a zero subduction rate. The other models all require the addition of the subduction effect in order to predict heat flow values as low as observed. The basement temperatures determined by the four models (Figure A.2b) are all in the range that would allow both initiation and propagation of megathrust earthquakes across the full width of Winona Basin even in the absence of any subduction effect. The coolest estimate yields a temperature at the position of the deformation front greater than 150°C. Even the warmest model yields a temperature cooler than 325°C beneath the landward part of the basin 35 km from the deformation front, and an ultimate 450°C temperature much landward. Addition of the cooling effect of subduction would cause the décollement to be even cooler and the potential rupture zone larger. The results suffice in pointing out the potential of tsunamigenic rupture of the décollement. For lack of more quantitative information, I refrain from devising rupture scenarios for this area.